FINDING THE MISSING PIECES OF THE STANDARD MODEL

by

David Atwood

David Atwood
Dept. of Physics
McGill University, Montreal,
June 1989.

A Thesis submitted to the Faculty of Graduate Studies and research in partial fulfillment of the requirements for the degree of Doctor of Philosophy.

ABSTRACT

The Standard Model is discussed in general and the predicted (but as yet unobserved) Higgs-boson and top-quark described. Detection of a top-quark at electron-positron colliders and hadron colliders is considered for $m_t<80GeV$. The detection of the Higgs-boson is considered at the Z peak in electron-positron annihilation for $m_H\leq 60GeV$, as well as in the continuum for $100\leq m_H\leq 200GeV$ (intermediate mass range). For this range of the Higgs-boson mass, consideration is also given to its detection at the Superconducting Supercollider through the tau-lepton decay mode. A dispersive approach is considered for Higgs-boson with large mass ($m_H>500GeV$) in order to estimate non-perturbative self-interaction effects.

RÉSUMÉ

Une discussion générale du Modèle Standard est faite ainsi qu'une description du boson de Higgs et du quark-top, particules dont l'existence est prédite mais qui sont à ce jour encore inobservées. La détection aux collisionneurs électron-positron et hadroniques est examinée pour $m_t<80$ GeV. La détection du boson de Higgs dans l'annihilation électron-positron à la résonance du Z est examinée pour $m_H<60$ GeV, de même que dans le continuum pour $100<m_H<200$ GeV (intervalle intermédiaire de masse). Pour ce même intervalle de masse nous considérons aussi sa détection au Superconducting Supercollider grâce à un mode de désintégration tau-lepton. Une approche dispersive est employée dans le cas d'une grande masse du boson de Higgs dans le but d'estimer les effets non-perturbatifs de self-interactions.

ACKNOWLEDGEMENTS

I would like to express my gratitude to my collaborators A. P. Contogouris, H. Tanaka, N. Mebarki and K. Takeuchi for their helpful discussions and encouragement. I would like to especially thank my thesis supervisor A. P. Contogouris for his guidance and assistance in preparation of this thesis. I would also like to thank J. Robinson for assistance in the preparation of this thesis and J. Malouin for helping me prepare the French abstract. I am grateful to G. Kane, R. M. Barnett and J. Gunion for discussions and suggestions and the academic staff and graduate students of the Physics Department of McGill University for helping me understand physics better.

TABLE OF CONTENTS

Title Page 1
Abstract 2
Résumé 3
Acknowledgements 4
Table of Contents 5
Preface 7

CHAPTER 1: BASIC FORMALISM AND CALCULATIONAL METHODS .. 10
1.1 Introduction 10
1.2 The Need For The Higgs-Boson and The Top-Quark 13
1.3 Monte Carlo Methods 28
1.4 Matrix Element Calculation 31
1.5 Jet Algorithm 36
Figure Captions for Chapter 1 41
Figures for Chapter 1 43

CHAPTER 2: TOP-QUARK DETECTION AT HIGH-ENERGY ELECTRON-POSITRON AND HADRON COLLIDERS 48
2.1 Introduction 48
2.2 Top-quark Detection at Electron-Positron Colliders 49
2.3 Top Quark Mass Determination in Hadron Colliders 58
Figure Captions for Chapter 2 64
Figures for Chapter 2 66

CHAPTER 3: HIGGS PRODUCTION AT OR NEAR THE Z PEAK IN ELECTRON-POSITRON ANNIHILATION 73
3.1 Introduction 73
3.2 Higgs Production at The Z Peak 76
3.3 Background from $Z \rightarrow q\bar{q}\nu\bar{\nu}$ 80
3.4 Possible Top-Quark Backgrounds 82
3.5 t-Quarkonium Effects 88
3.6 Conclusions 91
Figure Captions for Chapter 3 92
Figures for Chapter 3 94

CHAPTER 4: PRODUCTION OF THE INTERMEDIATE MASS HIGGS-BOSON IN FUTURE ELECTRON-POSITRON COLLIDERS 100
4.1 Introduction 100
4.2 Basic Formalism 102
4.3 Branching Ratios, Acceptance Cuts and Results 104
4.4 Background from $e^+e^- \longrightarrow Zt\bar{t}$ 107
4.5 Background from $e^+e^- \longrightarrow t\bar{t}$ 109

Conclusions 112
Appendix 4.A 113
Appendix 4.B 115
Figure Captions for Chapter 4 119
Figures for Chapter 4 121

CHAPTER 5: DETECTING AN INTERMEDIATE
MASS HIGGS-BOSON AT THE SSC THROUGH ITS
TAU-LEPTON DECAY MODE 125
5.1 Introduction 125
5.2 Detecting The Higgs-boson Using $pp \rightarrow H \rightarrow \tau^+ \tau^-$ 127
5.3 Conclusions 135
Figure Captions for Chapter 5 136
Figures for Chapter 5 139

CHAPTER 6: USING A DISPERSIVE APPROACH
TO A HEAVY HIGGS-BOSON 144
6.1 Introduction 144
6.2 The channel $HH \rightarrow HH$ 146
6.3 The Channel $Z_L Z_L \rightarrow Z_L Z_L$ 153
6.4 Conclusions 157
Figure Captions for Chapter 6 158
Figures for Chapter 6 159

CHAPTER 7: CONCLUSION 161

Footnotes and References 163

PREFACE

The following is an extract from the guidelines concerning thesis preparation of The McGill University Faculty of Graduate Studies and Research:

> The candidate has the option, subject to the approval of the Department, of including as part of the theses the text, or duplicated published test (see below), of an original paper, or papers. In this case the thesis must still conform to all other requirements explained in the Guidelines Concerning Thesis Preparation. Additional material (procedural and design data as well as descriptions of equipment) must be provided in sufficient detail (e.g. in appendices) to allow a clear and precise judgment to be made of the importance and originality of the research reported. The thesis should be more than a mere collection of manuscripts published or to be published. It must include a general abstract, a full introduction and literature review and a final overall conclusion. Connecting texts which provide logical bridges between different manuscripts are usually desirable in the interests of cohesion.
>
> It is acceptable for theses to include as chapters authentic copies of papers already published, provided these are duplicated clearly on regulation thesis stationary and bound as an integral part of the thesis. Photographs or other materials which do not duplicate well must be included in their original form. In such instances, connecting texts are mandatory and supplementary explanatory material is almost always necessary.
>
> The inclusion of manuscripts co-authored by the candidate and others is acceptable but the candidate is required to make an explicit statement on who contributed to such work and to what extent, and supervisors must attest to the accuracy of the claims, e.g. before the Oral Committee. Since the task of the Examiners is made more difficult in these cases, it is in the candidate's interest to make the responsibilities of authors perfectly clear. Candidates following this option must inform Department before it submits the thesis for review.

The text of the above shall be cited in full in the introductory sections of any theses to which it applies.

Several of the chapters are, with the approval of my supervisor (A. P. Contogouris) and the Physics Department at McGill University, taken partially from papers co-authored by myself and others.

Section 2.2 is taken from reference (1) which I am co-author with A. P. Contogouris and H. Tanaka. In this paper my main responsibility was to write the computer programs to generate the results as well as to check the algebraic calculations. H. Tanaka checked some of my numerical results while he and A. P. Contogouris did most of the algebraic calculations. Most of the preparation of the final text of the paper was done by A. P. Contogouris.

Section 2.3 is taken from reference (2) with the distribution of responsibilities as in section 2.2.

Chapter 3 is taken from reference (3) in which I am co-author with A. P. Contogouris, N. Mebarki and H. Tanaka. Again in this case, my main contribution was to do the computer calculations which were checked by H. Tanaka. The other authors did most of the algebraic work and A. P. Contogouris did most of the work with regard to preparation of the text of the paper.

Chapter 4 is taken from reference (4) in which I am co-author with A. P. Contogouris and K. Takeuchi. In this case I produced the numerical results which were checked by K. Takeuchi. A. P. Contogouris and K. Takeuchi produced most of the algebraic results in appendix 4.B some of which I checked

Chapter 6 is taken from reference (6) in which I am co-author with A. P. Contogouris and N. Mebarki and includes some results from reference (7). In this paper I wrote the computer program to numerically solve the Frecholm equations involved in the calculation. These results were checked by N. Mebarki. The dispersion theory calculations were mostly done by A. P. Contogouris, N. Mebarki and H. Tanaka; A. P. Contogouris did most of the work with regard to the preparation of the text of the paper.

In all of these cases deciding the direction of the work and consideration such as acceptance cuts etc. were discussed extensively among the collaborators hence the exact contribution of each can not be defined but was roughly equal. Also the wording of all of the above papers has been extensively modified and sections added to make them fit together in a cohesive text.

Chapter 5 is based completely on my own work.

CHAPTER 1

BASIC FORMALISM AND CALCULATIONAL METHODS

1.1 Introduction

The Standard Model of SU(3)xSU(2)xU(1) is basic to the present day understanding of particle physics. Within its framework all phenomena observed to date can be accounted for. This Model, however, requires the existence of the top-quark and the Higgs-boson which have yet to be observed. The observation of these particles is essential to the Standard Model and understanding whatever physics may lie beyond it.

The fundamental (in the sense that we believe them to be fundamental) fermions which have been observed so far can be arranged into three families. Within each family there is a massless neutrino, a massive charge -1 lepton, a massive charge -1/3 quark and a massive charge +2/3 quark where each of the quarks carries a $SU(3)_{color}$ charge. Thus, for example, the first generation consists of ν_e (the electron neutrino), the electron, e, the down-(d-)quark, and the up-(u-)quark. The second generation consists of ν_μ (the muon-neutrino), the muon (μ), the strange-(s-)quark and the charm-(c-)quark. Following the same pattern the third generation contains the ν_τ (tau-neutrino), the tau (τ), the b-quark but as yet no third charge +2/3 quark has yet been observed. Intuitively it seems reasonable to suppose that a third charge +2/3 quark exists and indeed the Standard Model requires it, (referred to as the top-(t-)quark) however so far experiments have been unable to observe it directly.

The other missing piece of the standard model is the Higgs-boson. This particle is required to explain the SU(2)xU(1) breaking mechanism and hence the generation of mass since an unbroken SU(2)xU(1) theory requires that all fermions and bosons are massless.

In this thesis we consider the question of how to detect these missing pieces of the standard model at accelerators presently operating or proposed for the near future such as LEP, SLC, $S\bar{p}pS$, the Tevatron, and the SSC. In this chapter, we review the standard model in section 1.2 then in section 1.3 we review the Monte Carlo method for calculating cross sections. Section 1.4 is concerned with algorithms for numerically calculating matrix elements suitable for computer calculations and section 1.5 contains an algorithm for estimating the jets observed in detectors based on parton subprocesses.

In chapter 2 we consider observing the t-quark at both electron-positron and hadron colliders. Specifically we consider the pair production of the top-quark for a mass range of $40 \leq m_t \leq 80 GeV$ (m_t is the top-quark mass)

In chapter 3 we consider production of a Higgs-boson at an electron-positron collider with center of mass energy $\sqrt{s} \sim M_Z$ where the Higgs-boson is produced in association with a neutrino pair. This could afford a method for detecting the Higgs-boson if its mass,

$m_H \leq 60 GeV$.

In chapter 4 we study Higgs-boson production at electron-positron colliders with $\sqrt{s}=300-500 GeV$. This would provide a method of detecting the Higgs-boson when $90 \leq m_H \leq 200 GeV$. If m_H is in this range it is particularly difficult to observe the Higgs-boson at other proposed colliders. To illustrate this, in chapter 5 we investigate the detection at the SSC (Superconducting Supercollider) of a Higgs-boson in this mass range through the $H \rightarrow \tau^+ \tau^-$ decay mode. Although this method is not especially successful, it illustrates the typical difficulties one has of seeing the Higgs-boson if its mass falls within this mass range.

If m_H is very large, on the order of $1 TeV$, perturbation theory is not a reliable way to describe the Higgs-boson. In chapter 6 we consider a dispersion model for such a Higgs-boson in order to try to understand some of the non-perturbative aspects of this case.

1.2 The Need For The Higgs-Boson and The Top-Quark

In this section we develop the standard model following reference (8). The notation we shall use is as follows: we will denote left handed fermion fields by u_L, d_L, e_L, and ν_L and right handed fields by u_R, d_R, and e_R. Dirac spinors are denoted for example by $u=\binom{u_R}{u_L}$ etc. and the weak eigenstates are denoted by capital letters. Thus $U=(u_R)$, $D=(d_R)$, $E=(e_R)$, and $Q=\binom{u_L}{d_L}$ and $L=\binom{\nu_L}{e_L}$. Generation indices are indicated by subscripts I, J, K, etc. and $\mathbf{D}_\mu$ is the covariant derivative to be defined in eq. 1.2.4.

When the 4-fermion structure of the weak interaction was first recognized, it was realized that there was a severe problem with the theory. For example, the effective lagrangian of radioactive β -decay (in terms of quark fields) is

$$L = \frac{1}{\sqrt{2}} G_F \; \bar{u}\gamma^\mu P_L d \;\; \bar{e}\gamma_\mu P_L \nu + h.c.$$

where

$$P_L = \frac{1}{2}(1-\gamma_5) \quad . \qquad 1.2.1$$

This is a term of mass dimension 6 and therefore cannot be a fundamental element of a renormalizable theory; so that although tree level calculations may be carried out, higher order calculations cannot be made to give sensible results. A closely related problem with such a term is that it leads to a violation of unitarity at an energy of about 300GeV (9a). The only way that these problems can be solved is to suppose that the 4-fermion term in the lagrangian is an effective term resulting from the integration of massive particles not directly observable at low energies. In 1957 Schwinger proposed the simplest such theory (9b). He hypothesized that there is a massive intermediate vector boson (the W-boson) which couples to fermions. Thus, if the lagrangian is

$$L = g_W(\bar{d}\gamma^\mu u + \bar{e}\gamma^\mu \nu)W_\mu + h.c.$$
$$+ M_W^2 W_\mu^+ W^{\mu -}$$

1.2.2

the 4-fermion coupling can be explained as a contraction of the W-boson exchange graph shown in figure 1.1. This hypothesis has since been dramatically confirmed by the discovery of the W-boson at $S\bar{p}pS$ (10).

Although all the terms in this lagrangian (eq. 1.2.2) are of dimension ≤ 4, this lagrangian is still not renormalizable. In fact, the only theories with vector particles which are known to be renormalizable are gauge theories where the vector particle is a gauge boson. Thus one might try to make a theory where the W-boson is taken to be such a gauge particle. The W, however, is massive and since gauge symmetries always force the corresponding gauge bosons to be massless some mechanism is necessary to break the symmetry thereby giving the W-boson a non-zero mass.

This problem was solved by Weinberg and Salam in 1967 (11) where the vector particles acquire their mass through the Higgs mechanism and, in addition, the weak force is unified with electromagnetism in a SU(2)XU(1) gauge theory.

The choice of this group is motivated by the fact that it is the lowest rank group which can contain as generators both the W and the U(1) of electromagnetism and introduces no exotic fermions. This group, however, has 4 generators leading to the prediction of an additional gauge particle, the Z-boson which has since been discovered at $S\bar{p}pS$ (9).

In order to develop this theory we start with the most general renormalizable lagrangian which one can write down with a scalar ϕ, left-handed lepton doublet L, right-handed electron singlet E, left-handed quark doublet Q, and right-handed quark singlet U and D. The fermion content has been chosen to be the simplest which yields the observed fermions within each generation, i.e. a massless neutrino, a massive lepton and two massive quarks with their observed charges (In reference (12) it is shown that the observed fermion quantum numbers are the ones needed to cancel the triangle anomaly). The gauge content is described by a U(1) field B_μ and a SU(2) gauge field $\mathbf{A}'_\mu$ (with corresponding field strengths $B_{\mu\nu}$ and $\mathbf{A}'_{\mu\nu}$). The relationship between physically observable particles and these gauge fields will be derived below (eq. 1.2.9).

This lagrangian is

$$
\begin{aligned}
L = &-\frac{1}{4}\mathbf{A}^{i}_{\mu\nu}\mathbf{A}^{i\mu\nu} - \frac{1}{4}B_{\mu\nu}B^{\mu\nu} \\
&+ (\mathbf{D}_{\mu}\phi)^{+}(\mathbf{D}^{\mu}\phi) + \mu^{2}\phi^{+}\phi - \lambda(\phi^{+}\phi)^{2} \\
&+ N^{(e)}{}_{IJ}\overline{L}_{I}\phi E_{J} + h.c. \\
&+ N^{(u)}{}_{IJ}\overline{Q}_{I}\tilde{\phi} U_{J} + h.c. \\
&+ N^{(d)}{}_{IJ}\overline{Q}_{I}\phi D_{J} + h.c. \\
&+ \overline{L}\, i\not{\mathbf{D}}\, L + \overline{E}\, i\not{\mathbf{D}}\, E \\
&+ \overline{Q}\, i\not{\mathbf{D}}\, Q + \overline{U}\, i\not{\mathbf{D}}\, U + \overline{D}\, i\not{\mathbf{D}}\, D
\end{aligned}
$$

1.2.3

where the indices I and J range over the number of existing fermion families and $\mathbf{D}_{\mu}$ is the gauge covariant derivative given by

$$\mathbf{D}_{\mu} = (\partial_{\mu} - i\frac{g}{2}t^{I}\mathbf{A}^{I}_{\mu} - ig'YB_{\mu}).$$

1.2.4

In this equation t^{I} are the generators of the appropriate representation of SU(2) (ie. the SU(2) Pauli matrices for left handed fermions and the Higgs doublet; 0 for right handed fermions) and the assignment of quantum numbers to the fermions and bosons is as follows:

	$SU(2)$	Y
E	1	-1
U	1	+2/3
D	1	-1/3
L	2	-1/2
Q	2	1/6
ϕ	2	1/2
A	3	0
B	1	0

1.2.5

The coupling strengths of SU(2) and U(1) are g and g′ respectively which will eventually be fixed by physically observable couplings.

Spontaneous symmetry breaking occurs if μ and λ are positive which gives rise to the Higgs potential shown in figure 1.2. This has a non-zero minimum at

$$\sqrt{2}|\phi| = \nu = \left(\frac{\mu^2}{\lambda}\right)^{\frac{1}{2}};$$

1.2.6

hence in the ground state, the Higgs field will have a non-zero vacuum expectation value $\sqrt{2}|<\phi>|=\nu$.

At this point we are still free to choose any gauge we wish. One may, in particular, choose to work in the unitary gauge where

$$\phi = \frac{1}{\sqrt{2}}\begin{pmatrix} 0 \\ \nu+h(x) \end{pmatrix} \qquad with \qquad h(x) = h^{+}(x) \ .$$

1.2.7

In this gauge we can eliminate the Higgs doublet so that the lagrangian becomes

$$L = \frac{v^2}{8}(g^2(\mathbf{A}^1_{\ \mu} \mathbf{A}^{1\mu} + \mathbf{A}^2_{\ \mu}\mathbf{A}^{2\mu}) + (g\mathbf{A}^3_{\ \mu} - g'B_\mu)(g\mathbf{A}^{3\mu} - g'B^\mu))$$

(a)

$$+\mu^2 h^2 + \lambda v h^3 + \frac{1}{4} h^4$$

(b)

$$+\frac{1}{\sqrt{2}} h (N^{(e)}_{\ IJ} \bar{e}_{L_I} e_{R_J} + N^{(u)}_{\ IJ} \bar{u}_{L_I} u_{R_J} + N^{(d)}_{\ IJ} \bar{d}_{L_I} d_{R_J}) \ + \ h.c.$$

(c)

$$+ M^{(e)}_{\ IJ} \bar{e}_{L_I} e_{R_J} + M^{(u)}_{\ IJ} \bar{u}_{L_I} u_{R_J} + M^{(d)}_{\ IJ} \bar{d}_{L_I} d_{R_J} + h.c.$$

(d)

$$-\frac{1}{4}\mathbf{A}^i_{\ \mu\nu}\mathbf{A}^{i\mu\nu} - \frac{1}{4} B_{\mu\nu} B^{\mu\nu}$$

(e)

$$+ \overline{L}\, i\not{D}\, L + \overline{E}\, i\not{D}\, E + \overline{Q}\, i\not{D}\, Q + \overline{U}\, i\not{D}\, U + \overline{Q}\, i\not{D}\, Q$$

(f)

where $\quad M_{IJ} = \frac{1}{\sqrt{2}} v N_{IJ}$.

1.2.8

Let us now rewrite the gauge fields as follows:

$$W^\pm = \frac{1}{\sqrt{2}}(\mathbf{A}^1 \mp i\mathbf{A}^2)$$

$$Z^0 = \cos\theta_W \mathbf{A}^3 - \sin\theta_W B$$

$$A = \sin\theta_W \mathbf{A}^3 + \cos\theta_W B,$$

1.2.9

where we have introduced the Weinberg angle θ_W defined by $\tan(\theta_W)=g'/g$. If we now rewrite (1.2.8a) in terms of these new fields, we get

$$M_W^2 W^+{}_\mu W^{-\mu} + \frac{1}{2} M_Z^2 Z_\mu Z^\mu \tag{1.2.10}$$

where $M_W^2 = \dfrac{1}{4} g^2 v^2$ and $M_Z^2 = \dfrac{1}{4}(g^2+g'^2)v^2$. Thus we have a massive W and Z boson satisfying the initial motivation of the intermediate vector boson hypothesis of Schwinger as well as the A field which corresponds to the electromagnetic field. With this additional transformation (eq. 1.2.9), the Yukawa terms in the fermionic sector (1.2.8d) and the kinetic terms (1.2.8f) can be transformed to

$$
\begin{aligned}
& C_L^e \bar{e}_{L_I} Z e_{L_I} + C_R^e \bar{e}_{R_I} Z e_{R_I} + C_L^\nu \bar{\nu}_{R_I} Z \nu_{R_I} + \\
& C_R^u \bar{u}_{R_I} Z u_{R_I} + C_L^u \bar{u}_{L_I} Z u_{L_I} + C_R^d \bar{d}_{R_I} Z d_{R_I} + C_L^d \bar{d}_{L_I} Z d_{L_I} \\
& - e\bar{e}_{L_I} A e_{L_I} - e\bar{e}_{R_I} A e_{R_I} \\
& + \frac{2}{3} e\bar{u}_{R_I} A u_{R_I} + \frac{2}{3} e\bar{u}_{L_I} A u_{L_I} - \frac{1}{3} e\bar{d}_{R_I} A d_{R_I} - \frac{1}{3} e\bar{d}_{L_I} A d_{L_I} + \\
& + \frac{g}{\sqrt{2}} \bar{\nu}_{L_I} W^+ e_{L_I} + h.c. \\
& + \frac{g}{\sqrt{2}} \bar{u}_{L_I} W^+ d_{L_I} + h.c. \\
& + M^{(e)}{}_{IJ} \bar{e}_{R_I} e_{L_J} + M^{(u)}{}_{IJ} \bar{u}_{R_I} u_{L_J} + M^{(d)}{}_{IJ} \bar{d}_{R_I} d_{L_J}
\end{aligned}
$$

where $\quad \mathbf{e} = g\sin\theta_W$

and

$$C^f_L = \frac{g}{\cos\theta_W}\left(\frac{T^f_3}{2} - Q_f \sin^2\theta_W\right) \qquad C^f_R = \frac{g}{\cos\theta_W}\left(- Q_f \sin^2\theta_W\right) \quad .$$

1.2.11

Here T^f_3= the third component of the weak isospin of fermion f and $Q_f = T^3_f + Y_f$.

We now have the desired interactions between the fermions and the bosons of the theory. If we interpret $\mathbf{e}$ as electric charge, then the terms proportional to A are the photon fermion interactions. Setting $g^2 = 4\sqrt{2}M^2_W G_F$ then the charged current interaction reproduces the correct 4-fermion interaction given in eq. 1.2.1.

The coupling of the Z-boson to fermions is given in terms of the constants C^f_L and C^f_R defined above. It is often convenient to write the Z-fermion coupling as $\bar{f}(A^f_Z + B^f_Z\gamma_5)\gamma_\mu f$ where $A^f_Z = (C^f_R + C^f_L)/2$ and $B^f_Z = (C^f_R - C^f_L)/2$. These constants are thus given by

$$A^f_Z = \frac{g_W}{2\cos\theta_W}(T^f_3 - 2Q_f \sin^2\theta_W), \quad B^f_Z = \frac{g_W}{2\cos\theta_W} T^f_3 \quad .$$

1.2.12

There are, *a priori*, no constraints on the Yukawa coefficients $M^{(f)}{}_{IJ}$ where f = e, u, or d. However, using the polarization theorem, we can rewrite these generation space matrices in the form

$$M^{(f)} = S^{(f)} \Delta^{(f)} T^{(f)}$$

1.2.13

where $S^{(f)}$ and $T^{(f)}$ are unitary and $\Delta^{(f)}$ is diagonal. Using these matrices the following field redefinitions are possible:

$$u_{L_I} = T^{(u)}{}_{IJ} u'_{L_J} \qquad u_{R_I} = S^{(u)}{}_{IJ} u'_{R_J}$$

$$d_{L_I} = T^{(d)}{}_{IJ} d'_{L_J} \qquad d_{R_I} = S^{(d)}{}_{IJ} d'_{R_J} \qquad \nu_{L_I} = T^{(\nu)}{}_{IJ} \nu'_{L_J}$$

$$e_{L_I} = T^{(e)}{}_{IJ} e'_{L_J} \qquad e_{R_I} = S^{(e)}{}_{IJ} e'_{R_J}$$

1.2.14

so that the Yukawa terms become

$$\sum_I \Delta^{(e)}{}_{II}\ \bar{e}'_{R_I}\ e'_{L_I} + \sum_I \Delta^{(u)}{}_{II}\ \bar{u}'_{R_I}\ u'_{L_I} + \sum_I \Delta^{(d)}{}_{II}\ \bar{d}'_{R_I}\ d'_{L_I} + h.c.\ .$$

1.2.15

The above gives rise to mass terms for the fermions by coupling the right handed fields to the left handed fields. We identify f' as the physical fermion states (mass eigenstates) and $\Delta^{(f)}{}_{II} = m_{f_I}$ as the mass of fermion f_I.

Applying this redefinition to the $W^{\pm}-$ fermion interaction we find that these terms become

$$\frac{g}{\sqrt{2}} (W^{+}\ \bar{\nu}'_{L_I} e'_{R_I} + V^{(KM)}{}_{IJ}\ W^{+}\ \bar{u}'_{L_I} d'_{R_J} + h.c.)$$

$$V^{(KM)}{}_{IJ} = T^{(u)+}\ \ T^{(d)}$$

1.2.16

where we have introduced the matrix $V^{(KM)}{}_{IJ}$, the Kobayashi-Maskawa matrix, in the charged current sector.

The matrix $V^{(KM)}$ is the product of two unitary matrices hence it is itself unitary and since we still have the freedom to define the quark fields up to a phase, $V^{(KM)}$ may be reduced to an orthogonal matrix if the number of generations is 2. If the number of generations is 3 it may be reduced to the following standard form (13) in terms of the parameters θ_1, θ_2, θ_3, and δ

$$V^{(KM)}=\begin{pmatrix} c_1 & s_1c_3 & s_1s_3 \\ -s_1c_2 & c_1c_2c_3-s_2s_3e^{i\delta} & c_1c_2c_3+s_2c_3e^{i\delta} \\ -s_1s_2 & c_1s_2c_3+c_2s_3e^{i\delta} & c_1s_2s_3-c_2c_3e^{i\delta} \end{pmatrix}$$

where $\quad s_i=\sin\theta_i$ and $c_i=\cos\theta_i$.

1.2.17

The terms in 1.2.8 proportional to h give rise to

$$\mu^2h^2+\lambda vh^3+\frac{1}{4}h^4+\sum_f m_f\frac{v}{\sqrt{2}}\bar{f}_R f_L + h.c.$$

$$+gM_W W^{+\mu}W^-_{\mu}+g\frac{M_Z}{\cos\theta_W}Z^\mu Z_\mu$$

1.2.18

which describes a self interacting scalar that couples to fermions with a strength m_f and to the W and Z gauge bosons with strength gM_W for the $W^{\pm}$, and $\frac{g}{\cos\theta_W}M_Z$ for the Z. This is the physical Higgs-boson.

This theory together with the $SU(3)_{color}$ gauge group for strong interactions is what is referred to as the Standard Model (SM).

In the bosonic sector of the model, as we have stated, the W- and Z-bosons have been discovered. In the leptonic sector we have three complete generations: e, ν_e, μ, ν_μ, τ, ν_τ. The quark sector, however, has an incomplete third generation, only 5 quark flavors have been observed namely u, d, s, c, and b. If our simple assumption about the fermion content of the theory that we started with is correct the bottom-quark should have an as yet unobserved partner, the top-quark. The physical Higgs-boson likewise has yet to be observed.

Direct searches for the top-quark at $S\bar{p}pS$ have so far proved unsuccessful yielding a lower bound on its mass of about $45GeV$ (14). Likewise, direct searches for the the Higgs-boson through the reaction $\Upsilon \to H\gamma$ at CUSB have led to a possible experimental lower bound of $\sim 3GeV$ (15) (see discussion below).

Although the direct evidence for the existence of the top-quark is still negative, there are some indirect theoretical reasons, besides the need to complete the third generation, suggesting that it should exist.

First of all, only if there are three or more generations in the Standard Model can $V^{(KM)}$ have phases that cannot be transformed away by field redefinitions such as the phase δ in the standard parameterization for 3 generations given above in equation 1.2.17.

Given that there is a complex term of the form

$$V^{(KM)}{}_{IJ}\ \bar{u}_{L_I} W^{+} d_{L_J} + h.c. \tag{1.2.19}$$

in the lagrangian one finds that if a CP transformation (charge conjugation and parity) is applied, the following is obtained:

$$V^{(KM)}{}_{IJ}^{*}\ \bar{u}_{L_I} W^{+} d_{L_J} + h.c.$$

1.2.20

hence such a term violates CP.

In nature CP violation is observed in the $K^0-\bar{K}^0$ system so it therefore seems natural to attribute this observed CP violation to complex terms in the KM matrix (16). If indeed this is the origin of CP violation, it can only happen if there are 3 or more generations.

Assuming that the standard model is correct, one can use indirect evidence to place an upper bound on m_t by a comparison of standard model radiative corrections to experimentally measured quantities. In a recent article (17), data from measurements of neutrino scattering and M_W^2/M_Z^2 are shown to put a limit (with 90% confidence) of $m_t \leq 175$, 180, $200 GeV$ according to whether m_H=10, 100. or $1000 GeV$. Clearly these radiative corrections are not very sensitive to m_H although if m_t were determined some restriction may possibly be placed on m_H.

The situation for the Higgs-boson is less clear. There is no reason for its existence other than the need to give mass to the fermions and vector bosons. Indeed theories such as technicolor do without it (18).

Since the Higgs-boson only couples to a particle with strength proportional to that particle's mass, experiments to date which involve collisions of stable particles found in nature (eg. electrons, protons, etc.) that are light on the electro-weak scale, do not probe it very well. Thus the lower bound on the Higgs-boson mass from $\Upsilon \rightarrow H\gamma$ is small compared to bounds on the masses other kinds of particles. In fact it is not completely clear how firm this bound is. In reference (19) it is demonstrated that the one-loop QCD corrections to this process can be as large as 90% suggesting that perhaps even the two loop corrections might be similarly large. This brings into question the validity of any theoretical predictions for this process. Furthermore it has been pointed out in reference (20a) that there are some mass ranges $\leq 1 GeV$ which may not be totally excluded; $m_H \leq 13 MeV$ however is firmly ruled out due to the long range component to the nuclear force the exchange of such a Higgs-boson would induce (20b,c).

If, however, one takes the standard model literally, and the top-quark is relatively light, the mass of the Higgs-boson must be $\geq 7 GeV$ or else radiative corrections cause the minimum of the effective Higgs potential to be at 0 preventing spontaneous symmetry breaking (20d).

In the other extreme, if the mass of the Higgs-boson is $\geq 700 GeV$ the Higgs-boson self coupling becomes so large that perturbation theory is no longer useful to describe it. Symptomatic of this is the fact that a perturbative calculation of the width of the Higgs-boson yields a width greater than its mass (21). A very heavy Higgs-boson, is also subject to the triviality bound. This bound comes about because the self coupling of a heavy Higgs-boson is so large that the renormalized coupling diverges at a scale below the Higgs mass. The theory is therefore inconsistient if the Higgs-boson mass is larger than some bound. Reference (22) gives a conservative triviality bound of $m_H < 900 GeV$, as well as more restrictive bounds based on less conservative estimates. There are therefore at least two orders of magnitude of the Higgs-boson mass to search.

The search for the top-quark breaks down into roughly 3 regions, light, intermediate, and heavy. If the mass of the top-quark is light, $m_t \leq M_Z/2$, then it should be visible at LEP or SLC from the decay $Z \rightarrow t\bar{t}$. As it happens this range is almost, but not quite, ruled out by existing results from $S\bar{p}pS$ (14). If $M_Z/2 \leq m_t \leq M_W$, the intermediate mass range, then the top-quark should decay either leptonically or hadronically in which case it should be visible at a hadron collider or an electron-positron collider with these signatures. In the heavy range where $m_t > M_W$, the top-quark can decay directly into a W giving a rather different signature.

The search for the Higgs-boson breaks down into 5 important regions. The ultra-light range covers Higgs-boson with mass $m_H \leq 1 GeV$ as considered in reference (20). If the Higgs-boson is in the light range, $1 GeV \leq m_H \leq M_Z$, then it should be detectable through $e^+e^- \rightarrow HZ^*$ at LEP I or LEP II as, for example we consider in chapter 3. If $M_Z \leq m_H \leq 2M_W$ (the intermediate mass range), then the detection of the Higgs-boson is problematic, particularly if $m_H \geq 2m_t$ it is too heavy to be produced at LEP II and although it would be produced at a rate of 10^6 per year at the SSC (23), the backgrounds would be formidable and it is not clear that it could be seen in all cases (24a,b). Perhaps the only certain way to see a Higgs-boson with mass in this range is at an electron-positron collider with $\sqrt{s} \sim 300 - 500 GeV$ through the process $e^+e^- \rightarrow HZ$ as we consider in chapter 4. If the Higgs-boson is heavy, $2M_W \leq m_H \leq 800 GeV$, then it would decay into two vector bosons and with this signature it could be identified at the SSC (24c,d,e). If $m_H \geq 800 GeV$, the so called obese range, its width becomes too large with respect to its mass and it is hard to detect through any process since the peak is no longer distinct.

In the calculation of signals and backgrounds, we very often want to perform integrals of the form

$$\sigma = F\int |M(\Phi)|^2 \chi(\Phi) d\Phi \tag{1.3.1}$$

where σ is the cross section of some physical process, F is the flux factor $|M(\Phi)|^2$ is the square of the matrix element, Φ is a point in the phase space of the final state of the scattering process and $\chi(\Phi)$ is a function which represents some acceptance cuts; $\chi(\Phi) = 1$ if the cuts are satisfied and 0 otherwise.

This form of integral is usually intractable analytically; hence a Monte Carlo method must be used to calculate it numerically. To do this we rewrite the above as

$$\sigma = F\overline{|M|^2\chi}\ V \tag{1.3.2}$$

where $V = \int d\Phi$ is the total volume of available phase space and $\overline{|M|^2\chi}$ is the average of $|M|^2\chi$ over the phase space. Numerically this average is calculated by the formula

$$\overline{|M|^2\chi} = \frac{1}{n}\sum_{i=1}^{n} |M(\Phi_i)|^2 \chi(\Phi_i) \tag{1.3.3}$$

where the sum is taken over n randomly selected points from the final state phase space.

When considering processes in hadron colliders, we need to generalize the above method. In such cases, the fundamental physics is given in terms of a parton subprocess whereas it is only the inclusive cross section which is seen experimentally. This inclusive cross section, in terms of the parton cross section $\hat{\sigma}$ with the initial partons 1 and 2 is given by

$$\sigma = \int \hat{\sigma}(\hat{s})\, f_1(x_1)\, f_2(x_2)\, dx_1 dx_2 \tag{1.3.4}$$

were x_i is the momentum fraction of parton i, $\hat{s} = s\, x_1 x_2$ is the center of mass energy squared of the parton subprocess and f_i is the structure function of the parton i. To evaluate this integral, we first perform the transformation

$$w = \frac{1}{x_1 x_2}$$

$$y = \frac{1}{2}\ln(\frac{x_1}{x_2})$$

$$x_1 = w^{-\frac{1}{2}} e^{y}$$

$$x_2 = w^{-\frac{1}{2}} e^{-y} \tag{1.3.5}$$

so that the above integral becomes

$$\sigma = \int w^{-2}\, \hat{\sigma}(\hat{s})\, f_1(x_1)\, f_2(x_2)\, dw\, dy \tag{1.3.6}$$

This form has the advantage that the factor $f_1(x_1)\, f_2(x_2)\, w^{-2}$ is usually a relatively smoothly varying function therefore the Monte Carlo average converges more rapidly.

To integrate the above we first select y and w from their allowed ranges

$$1 \le w \le \frac{s}{\hat{s}_{min}}$$

$$-\frac{1}{2}\ln(w) \le y \le \frac{1}{2}\ln(w)$$

1.3.7

in such a way that there is a constant probability per unit area of picking a point in the section of the w-y plane within this range. Here, $\hat{s}_{min}$ is the minimum value of $\hat{s}$ we wish to consider for the subprocess.

Next, we calculate $\hat{\sigma}(\hat{s})$ using the above method (eq. 1.3.3) and multiply the resulting average by the total area in the w-y plane of the allowed range:

$$\left(\frac{s}{\hat{s}_{min}}\right) \ln\left(\frac{s}{\hat{s}_{min}}\right) - \frac{s}{\hat{s}_{min}}$$

1.3.8

1.4 Matrix Element Calculation

Many of the processes which we consider, particularly the backgrounds to some of our signals require the calculation of complicated Feynman diagrams involving many fermion lines. Such diagrams lead to intractable expressions for $|M|^2$, the squared matrix element hence for practical calculations it is useful to develop special algorithms to handle these calculations numerically.

The standard method of doing such a calculation is to convert the spin summed $|M|^2$ into a trace of $\gamma -$ matrices and evaluate the resulting expression. For example if the only diagram contributing to a process is that of figure 1.3, we are required to evaluate the trace

$$tr(\not{p}_1\gamma^{\mu}\not{p}_2\gamma^{\nu})\ tr(\not{p}_3\gamma_{\mu}(\not{p}_4+\not{p}_5+\not{p}_6)\gamma_{\alpha}\not{p}_4\gamma_{\beta}(\not{p}_4+\not{p}_5+\not{p}_6)\gamma_{\nu})\ tr(\not{p}_5\gamma^{\alpha}\not{p}_6\gamma^{\beta}) \tag{1.4.1}$$

If there are n Feynman diagrams contributing, then in general one is required to calculate both squared terms and interference terms so that one must do n(n+1)/2 trace calculations. In cases such as the 4-fermion background to Higgs-boson production on the Z resonance (see chapter 3), the final expressions may be very complicated as can be seen for example in appendix 4.B (a symbolic manipulation package can be helpful). In such cases it is often more convenient to use a method where M is calculated directly for each diagram with a given assignment of spins of the external particles; the total for all diagrams is summed and then squared. $|M|^2$ is then appropriately averaged over particle spin and phase space. Methods based on this principle have the advantage that if there are n diagrams involved only n different calculations need be considered. Here we discuss two methods which are based on this principle. Since in our applications of these methods, the fermions may be taken to be massless, our discussion will be of that case.

The first method is to write all spinors in the Weyl basis. In this basis

$$\gamma_5 = \begin{pmatrix} 1 & 0 \\ 0 & -1 \end{pmatrix} \qquad \gamma^\mu = \begin{pmatrix} 0 & \sigma^\mu{}_L \\ \sigma^\mu{}_R & 0 \end{pmatrix} \quad ; \tag{1.4.2}$$

where σ^μ_R, *and* σ^μ_L are left and right handed Pauli matrices given by

$$\sigma^0_R = +\sigma^0_L = \begin{pmatrix} 1 & 0 \\ 0 & 1 \end{pmatrix} \qquad \sigma^1_R = -\sigma^1_L = \begin{pmatrix} 0 & 1 \\ 1 & 0 \end{pmatrix}$$

$$\sigma^2_R = -\sigma^2_L = \begin{pmatrix} 0 & -i \\ i & 0 \end{pmatrix} \qquad \sigma^3_R = -\sigma^3_L = \begin{pmatrix} 1 & 0 \\ 0 & -1 \end{pmatrix} \quad ; \tag{1.4.3}$$

these matrices satisfy the commutation relations

$$[\sigma^\mu_R, \sigma^\nu_R] = +i\epsilon_{\mu\nu\alpha\beta}\sigma^\alpha_R\sigma^\beta_R$$

$$[\sigma^\mu_L, \sigma^\nu_L] = -i\epsilon_{\mu\nu\alpha\beta}\sigma^\alpha_L\sigma^\beta_L \tag{1.4.4}$$

Spinors representing fermions with specific helicities have only two non-zero components which are the two component Weyl spinors. For a specific helicity assignment we can therefore write all the spinorial products as products of 2x2 matrices. Note that such products can be carried out much faster than products of 4x4 matrix which would in general be necessary in the Dirac basis.

For example in figure 1.3 if all the fermion lines are left handed, the expression for the amplitude is

$$M \propto u^{+}{}_{L}(p_1)\sigma^{\mu}_{L}u_L(p_2) \cdot u^{+}{}_{L}(p_3)\sigma^{\mu}{}_{L}(p_4+p_5+p_6)^{\alpha}\sigma_{R_{\alpha}}\sigma^{\nu}{}_{L}u_L(p_4) \cdot$$

$$u^{+}_{L}(p_5)\sigma^{\mu}_{L}u_L(p_6) \cdot (4 \;\; p_1 \cdot p_2 \;\; p_3 \cdot p_4)^{-1}$$

1.4.5

where $u_l(p_i)$ is the two component Weyl spinor. In practice, the currents associated with the lines (1,2) and (5,6) may be evaluated as a four vector and substituted into the intermediate matrices of line (3,4).

Since it is important to have more than one way to calculate a given diagram, we also use the method outlined in (25). In this method, explicit chiral spinors are constructed with the use of light-like reference vectors a and b which will be fixed later.

We select as a reference spinor any left-handed spinor in a given direction a, and denote it by u_0, thus $\overline{u}_0 \; u_0 = P_L \boldsymbol{d}$.

Using this reference spinor we can construct left and right handed spinors for an arbitrary momentum vector p (provided p is not parallel to a or b) where:

$$u_R(p)=\frac{\not p u_0}{\sqrt{2p\cdot a}}$$

$$u_L(p)=\frac{\not p \not b u_0}{\sqrt{4p\cdot a\ p\cdot b}}$$

1.4.6

so that

$$u_R(p)\overline{u}_R(p) = \not p\ P_R$$

$$u_L(p)\overline{u}_L(p) = \not p\ P_L$$

1.4.7

In the case where all the fermions are left handed we may write the amplitude of figure 1.3 using the above identities as

$$M = (2p_1\cdot p_2)^{-1}\ (2p_5\cdot p_6)^{-1}\ \overline{u}_L(p_1)\gamma^\mu u_L(p_2)$$

$$\overline{u}_L(p_3)\gamma_\mu\ \ (u_L(p_4)\overline{u}_L(p_4) + u_L(p_5)\overline{u}_L(p_5) + u_L(p_6)\overline{u}_L(p_6))\ \ \gamma_\nu u_L(p_4)$$

$$\overline{u}_L(p_5)\gamma^\nu u_L(p_6)$$

1.4.8

The summed γ_μ - matrices may be reduced using the identities

$$\overline{u}_L(p_1)\gamma^\alpha u_L(p_2)\ \ \overline{u}_L(p_3)\gamma_\alpha = -4(p_1\cdot p_3)\frac{\overline{u}_L(p_1)\ \ \not p_2}{\overline{u}_L(p_2)\not p_1\ u_L(p_3)}$$

$$\overline{u}_R(p_1)\gamma^\alpha u_R(p_2)\ \ \overline{u}_L(p_3)\gamma_\alpha = +4(p_2\cdot p_3)\frac{\overline{u}_R(p_1)}{\overline{u}_R(p_2)\ u_L(p_3)}$$

1.4.9

and their conjugates as well as the corresponding identities with $L\leftrightarrow R$.

If we define

$$S_{ij} = T_{ji}^* = \bar{u}_R(p_i)u_L(p_j) \ ;$$

$$S_{ii} = T_{ii} = 0 \ ;$$

1.4.10

expression 1.4.8 becomes (after some simplifications)

$$M=4\frac{T_{13}S_{64}(T_{24}S_{45}+T_{26}S_{65})}{S_{21}T_{21}S_{65}T_{65}} \ .$$

1.4.11

We now make a standard choice of reference vectors a=(1,1,0,0) and b=(1,-1,0,0) and so S and T defined above achieve the simple form

$$T_{ji}^* = S_{ij} = \frac{(p_i^0-p_i^1)\,(p_j^0+p_j^1) - (p_i^2+ip_i^3)\,(p_j^2-ip_j^3)}{\sqrt{(p_i^0-p_i^1)\,(p_j^0+p_j^1)}} \ ;$$

1.4.12

in this way all diagrams and helicity combinations may be reduced to simple products of S and T factors. For a given choice of momenta therefore, one can first calculate S_{ij} and T_{ij} and then sum the amplitudes. This method has the advantage of proceeding in some cases somewhat faster than the first; there is however a less direct correspondence between the initial amplitude and the computer code, hence a greater chance of programming error. In cases where we have used these methods we have calculated each cross section using two different methods to assure that there is no programming error.

1.5 Jet Algorithm

In some of our calculations, the matrix element which we produce refers only to a specified final state of partons. Because of QCD confinement, colored partons cannot, of course, be seen directly by the detecting apparatus. What is in fact seen are hadronic jets corresponding to the final state partons

Unlike an electron or muon, a hadronic jet is not a single particle whose momentum and energy can be easily determined but rather a collection of hadrons which go generally in the same direction as the initial parton and carry its momentum. Detecting such a jet and measuring its momentum is not an easy task and to accurately simulate it one would have to first use an algorithm such as ISAJET or PYTHIA which simulates the fragmentation of partons into hadrons and then use a detector simulator, which simulates the detection of these hadrons by a specific detector.

The intent of our work is not to enter into experimental details but rather to make statements which will be independent of specific detector design. We would also like to make our statements independent of QCD processes of small transverse momentum (soft processes), because these are not fully understood theoretically and, in addition, an enormous amount of computer time would have to be used to gain a limited amount of additional information. To this end we introduce a jet algorithm which simulates the production and detection of jets given the initial momenta of the partons.

Three general effects are taken into account by our jet algorithm. First, the fact that any detector must have a blind spot where the beams enter and leave it. Thus, a jet which is too close to this blind spot will be poorly measured and, in a cautious simulation should be discarded. Secondly, jets which are too close in direction to one another will merge and be seen by the detector as a single jet. Third, jets with too small transverse momentum may not be prominent enough against the many soft hadrons produced in all directions to be noticed as definite jets in the analysis of an event hence should be discarded. The jet algorithm which we use to accomplish these three objectives is that of reference (26) which is similar to that of reference (27).

For a given event we are presented with the 4-momenta $p_1, \ldots ,p_n$ for the n partons in the final state. The direction which each of these partons is moving can be described by an azimuthal angle ϕ and either a polar angle θ or a rapidity y given by

$$y = \ln(\cot\frac{\theta}{2}) \tag{1.5.1}$$

In the case of electron positron collisions, we use the variable θ since the event is always in the centre of mass frame while for hadron colliders we use the variable y, since it is traditional in the literature and because differences in y are invariant under the longitudinal boost necessary to transform between the frame of the parton subprocess and the lab frame. We will discuss the algorithm in the electron-positron case, while in the hadron case may be obtained by replacing θ with y.

For the parton labeled i we define the transverse momentum

$$P_{T_i} = \sqrt{(p_i^1)^2 + (p_i^2)^2}$$

1.5.2

and for each pair of partons i,j we define a distance function

$$\Delta_{ij} = cos^{-1}\frac{\vec{p}_i \cdot \vec{p}_j}{\sqrt{\vec{p}_i^2\,\vec{p}_j^2}} \qquad in\ e^+e^-\ case$$

$$\Delta_{ij} = \sqrt{(y_i - y_j)^2 + (\phi_i - \phi_j)^2} \qquad in\ p\bar{p}\ case$$

1.5.3

The first step of the jet algorithm is to eliminate all partons which have transverse momentum less than p_T^0 and which are closer to the beam axis than θ_0* i.e.

$$|\cos\theta| < |\cos\theta_0{}^*|$$

$$p_T \geq p_T^0$$

1.5.4

(in the case of a hadron collider, we eliminate partons with $|y| \geq y_0$). Then we relabel the remaining partons in in such a way that they are arranged from largest to smallest transverse momentum, p_t.

If parton 1 is far from all the other partons or jets in the sense that $\Delta_{ij} > \Delta_0$ then we consider it to form a jet in itself and place it on the final list of jets. Then we repeat this step with parton 1 eliminated from the list of partons (relabeling partons as required)

If parton 1 is not far from all other partons, let j be the label of the parton such that Δ_{1j} is smallest (hence $\Delta_{1j}<\Delta_0$). Replace p_1 by p_1+p_j eliminating p_j from the list of partons (relabeling as required) and repeat this step.

At the end of this process one has a list of possible jets. Eliminate any jet that does not satisfy the transverse momentum requirement and separation from the beam axis requirement as specified above for individual partons. This situation could come about if partons near the beam axis have been combined to form jets.

The jet algorithm is thus specified by the parameters Δ_0, p_T^0, and θ_0* (y_0).

Figure 1.4 illustrates the action of the jet algorithm on some typical events of the form $e^+ e^- \rightarrow$ 4 massless partons. Each of the figures 1.4a-1.4l depicts a single event with $\sqrt{s}$=100GeV in the center of mass frame. The directions of the initial partons are indicated by X's on a $\cos(\theta)-\phi$ plane with the size of the symbol indicating the momentum of the parton. Each of the partons is surrounded by a curve representing a cone of 15^o hence if two of these curves intersect the partons are closer than 30^o to each other. The jet algorithm is then run with the parameters Δ_0=30^o, p_T^0=10GeV, and $\cos(\theta_0*)$=0.9 with the resulting jets indicated by O's.

Figures 1.4a-1.4d show typical 4-jet events. Note that none of the curves around the partons overlap hence all the partons are separated by more than Δ_0=30^o and none of the partons are within the bands indicating $|\cos(\theta)|\geq\cos(\theta_0*)$=0.9.

Figures 1.4e-1.4h show typical 3 jet events. Figure 1.4e and 1.4f each have one parton that does not form a jet because it falls too close to the beam axis ($|\cos(\theta)|>0.9$). Figure 1.4g and 1.4h shows cases where one of the partons failed to form a jet because it had transverse momentum less than p_T^0. Figures 1.4i-1.4l show similar examples where two of the jets have been eliminated giving 2-jet events.

Figure 1.5 shows how the results of the jet algorithm behave as a function of the parameter Δ_0. Events of the form $e^+e^- \to 4$ massless partons with $\sqrt{s}=100 GeV$ where generated with a constant matrix element and then the jet algorithm was run with the parameters $p_T^0=10 GeV$, $\cos(\theta_0{}^*)=0.9$ and various value of Δ_0. As could be expected when Δ_0 is increased, the 3- and 4-jet events become events with smaller N_J (mostly 2-jet events) due to the merging of jets. Note, however that for $\Delta_0<50^o$, the region of practical interest, the proportion of events with a given number of jets is fairly stable so that one expects that predictions based on the jet algorithm should not be drastically changed by the experimental details or soft QCD effects, since one would expect that such factors would be manifested as a change in the effective value of Δ_0.

Figure Captions

Figure 1.1

A 4-fermion term in the effective lagrangian at low energies may in fact be due to a massive vector exchange.

Figure 1.2

The Higgs potential necessary for spontaneous symmetry breaking. The minimum corresponds to the vacuum expectation value of the Higgs field.

Figure 1.3

An illustrative example of a process involving massless fermions, in this case $e^+e^-\rightarrow e^+e^-e^+e^-$

Figure 1.4

Typical examples of the jet algorithm in operation are shown. Some events with 4 massless particles in the final state were generated with an even distribution in phase space with $\sqrt{s} = 100GeV$. The initial directions of the partons in the $\cos\theta-\phi$ plane are indicated by X's while the final jets are marked by O's. The size of the symbol is related to the momentum of the particle and the curve around each symbol represents a cone of radius 15^o. In the jet algorithm we have used the parameters $p_t^0 = 10GeV$, Δ_0=30^o and $|\cos(\theta_0{}^*)| = .9$. (a)-(d) show typical events where the jet algorithm found 4 jets. The upper and lower horizontal lines on these diagrams represent $|\cos(\theta_0{}^*)| = .9$. (e)-(h) show typical events where the jet algorithm found 3 jets and (i)-(l) show typical events where the jet algorithm found 2 jets.

Figure 1.5

A plot of the fraction of events (generated from phase space) versus Δ_0 satisfying N_J=0,...,4 where the other parameters are $\sqrt{s}$=100GeV, $p_T^0 = 10GeV$ and $|\cos(\theta_0{*})| = .9$. N_J=0 is shown with the solid curve; N_J=1 is shown with the dash-dot curve; N_J=2 is shown with the dash-dot-dot curve; N_J=3 is shown with the dash-dot-dot-dot curve and N_J=4 is shown with the dash-dot-dot-dot-dot curve.

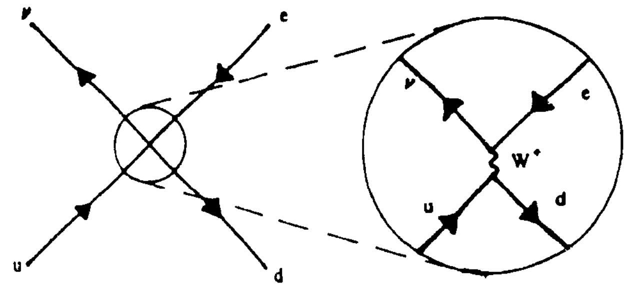

Figure 1.1

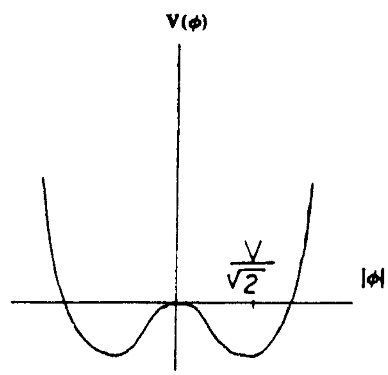

Figure 1.2

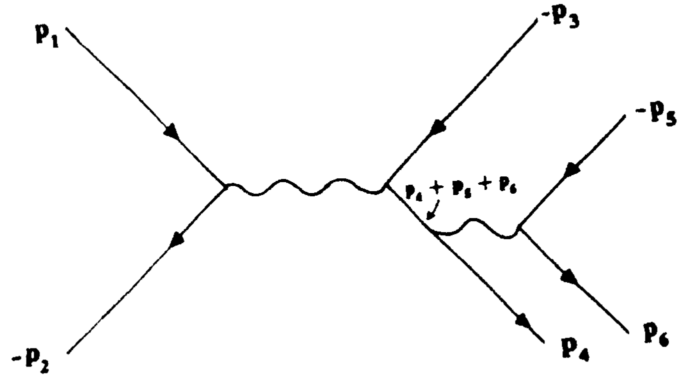

Figure 1.3

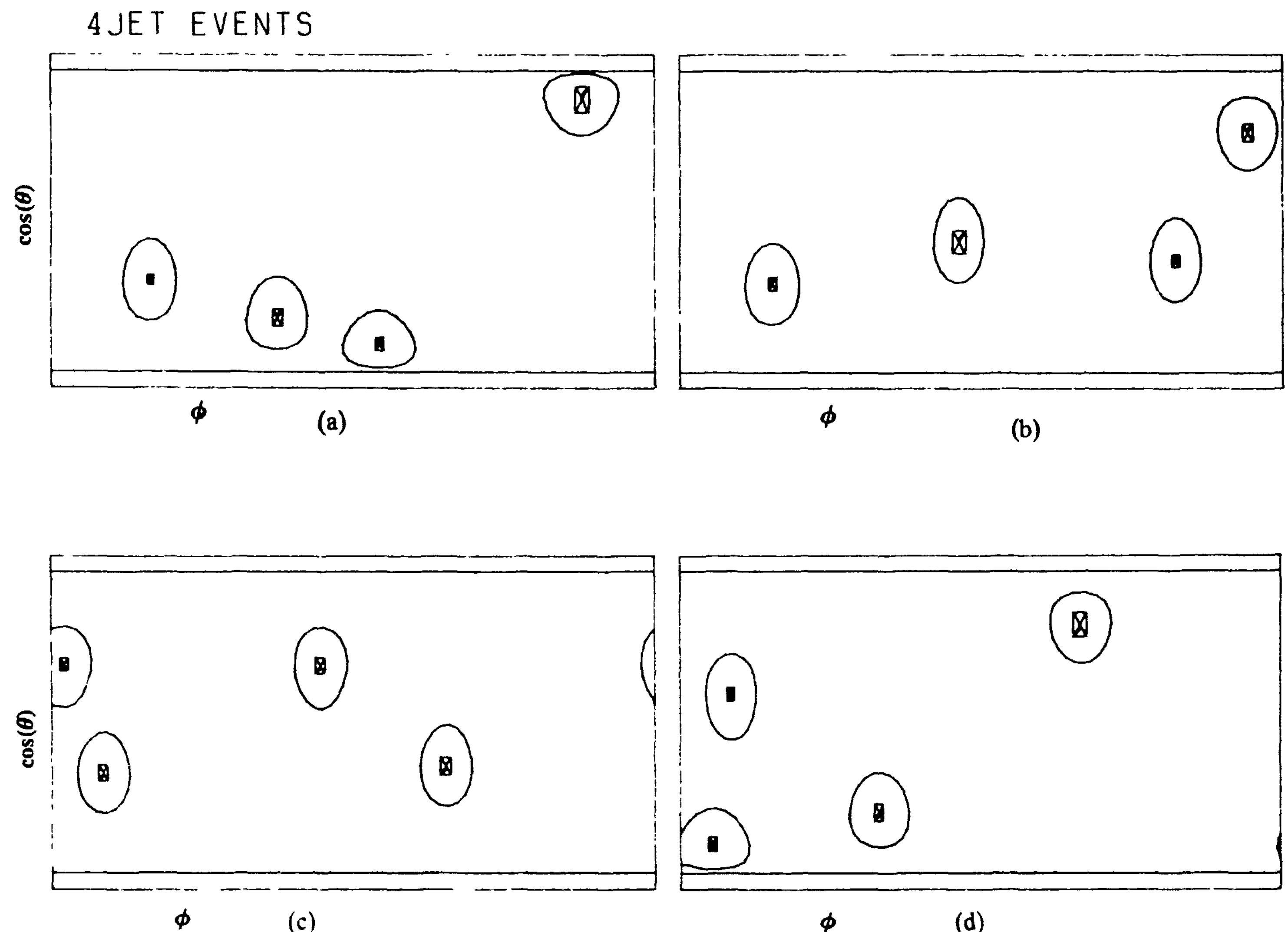

Figure 1.4

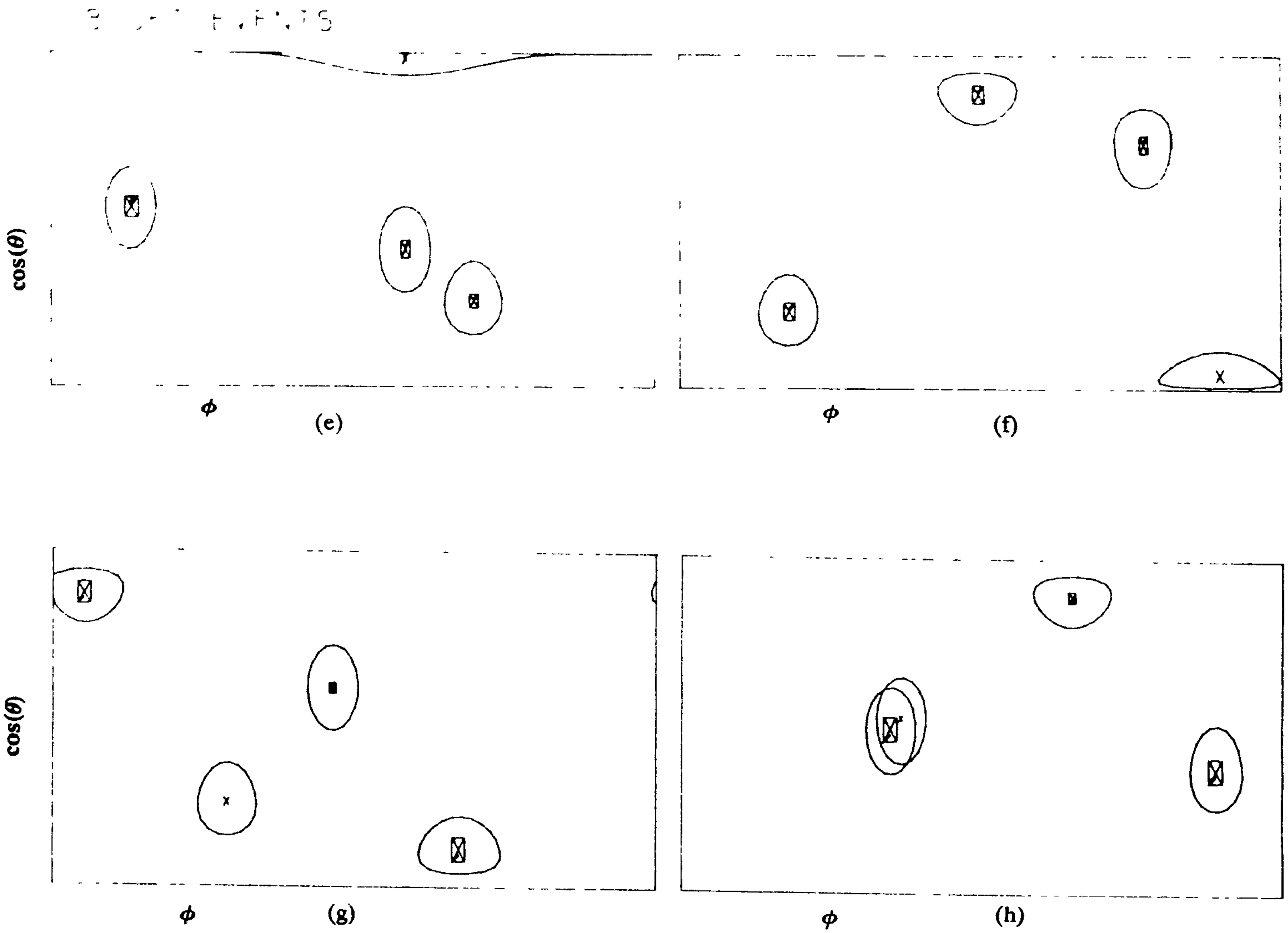

Figure 1.4

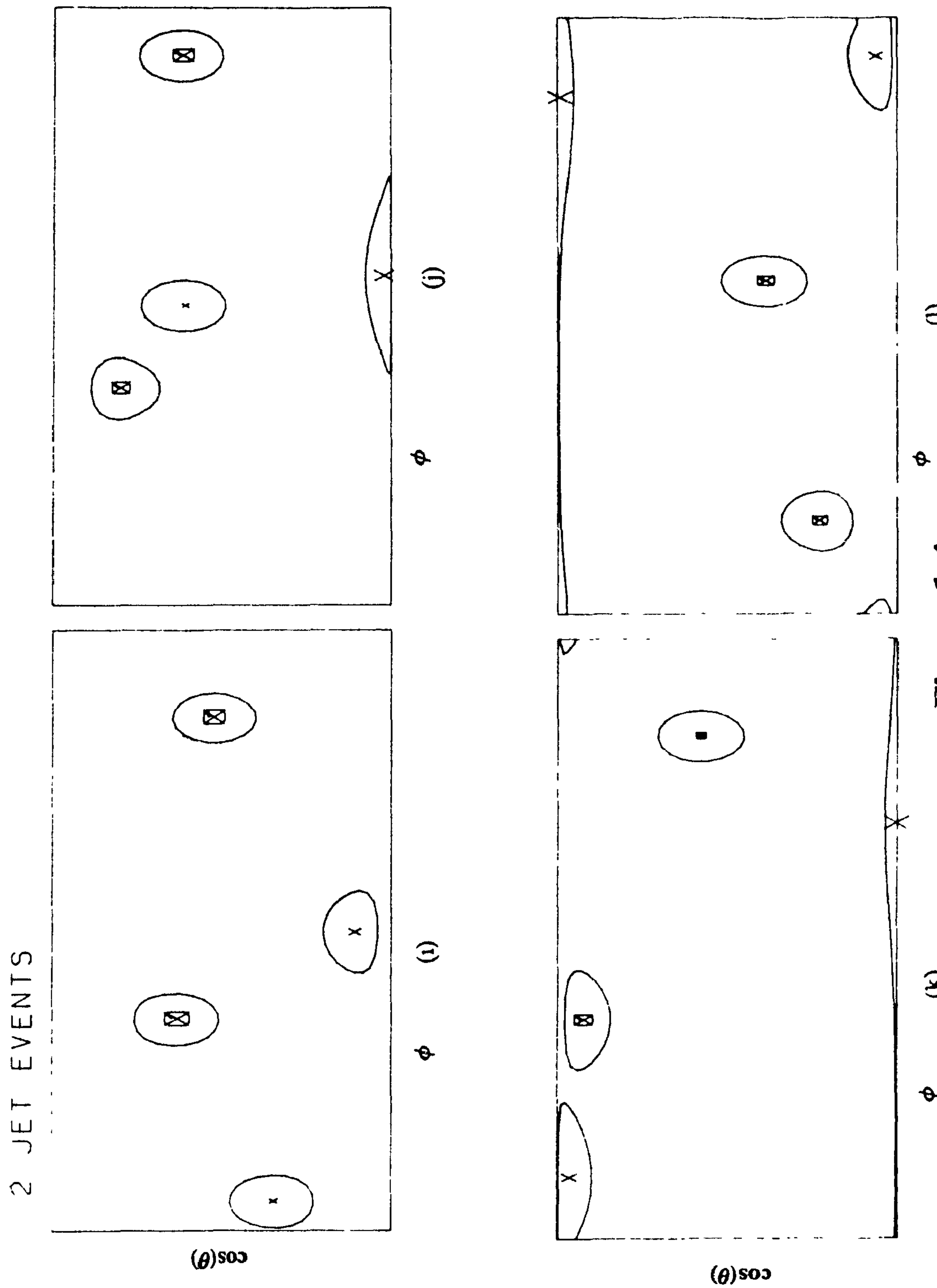

Figure 1.4

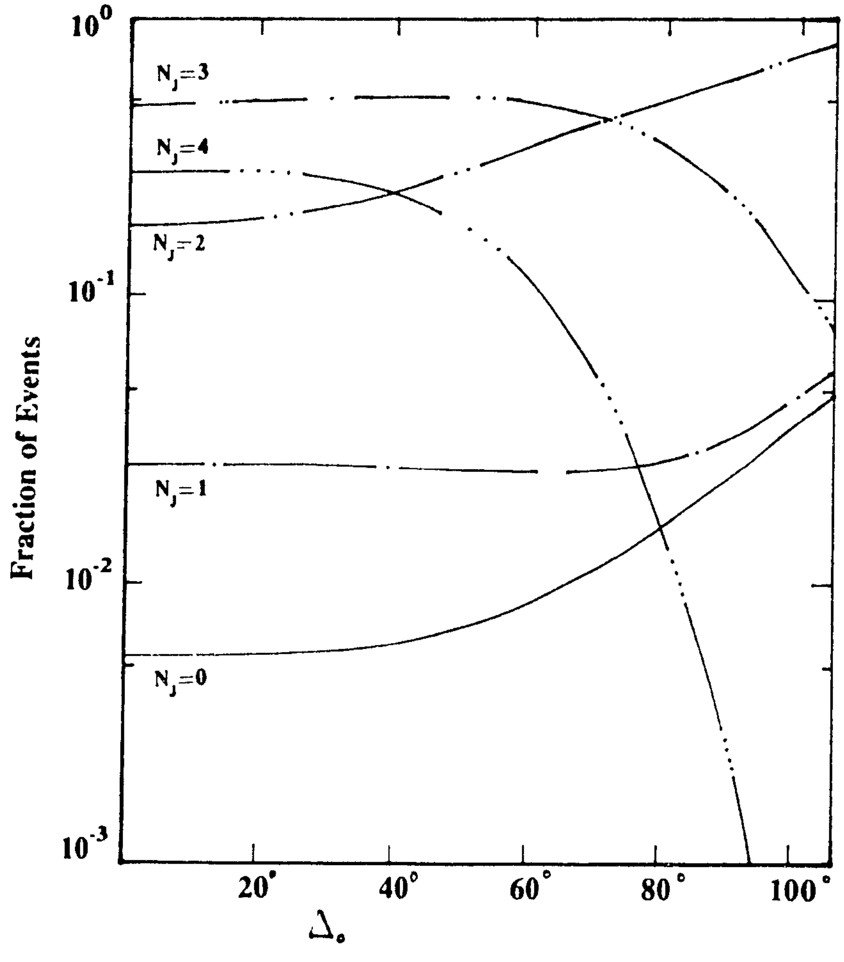

10^0
10^{-1}
10^{-2}
10^{-3}
Fraction of Events
$N_J=3$
$N_J=4$
$N_J=2$
$N_J=1$
$N_J=0$
20°
40°
60°
80°
100°
$\Delta_\circ$

Figure 1.5

CHAPTER 2

TOP-QUARK DETECTION AT HIGH-ENERGY ELECTRON-POSITRON AND HADRON COLLIDERS

2.1 Introduction

As we discussed in Chapter 1, the standard model predicts that there is a top-quark and present evidence suggests that its mass must lie in the range $45GeV \leq m_t \leq 200GeV$. In this chapter, we concern ourselves with a top-quark whose mass falls within the light or intermediate mass range defined in section 1.2, ie. with $m_t \leq 80GeV$. In this range the top-quark decay will be predominantly a 3 body weak decay ($t \rightarrow bq\bar{q}'$ or $t \rightarrow bl^+\nu_l$) as opposed to a top-quark which falls in the heavy mass range, $m_t > 80GeV$ where it will decay by $t \rightarrow bW^+$. The light and intermediate mass ranges are of interest because they are now experimentally accessible through hadron colliders such as the Tevatron or electron-positron colliders such as LEP or SLC. Section 2 of this chapter deals with detection of such a top-quark at an electron-positron collider produced though the reaction $e^+e^- \rightarrow t\bar{t}$. In section 3 we consider the detection of a top-quark produced though the analogous strong process at a hadron collider. Note that the work in this chapter was done before the present restrictions on the top-quark mass were established, hence we consider some cases which at the present time are disfavored.

Let us consider

$$e^+e^- \rightarrow t\bar{t} \rightarrow \; jets \; + l + \not{p} \qquad 2.2.1$$

($\not{p}$= missing momentum) at LEP and SLC energies. We intend to show that, with proper procedures involving a series of acceptance cuts, top-quarks with mass as large as $m_t \approx 60-70 GeV$ can be identified.

The type of event which we shall consider is $e^+e^- \rightarrow t\bar{t}$ via either Z^* or γ^* (* denotes a virtual particle) where the Z^* may be on resonance or otherwise. Let p_1, p_2, p_3, and p_4 denote the four momenta of e^-, e^+, t, and $\bar{t}$ respectively as in figure 2.1(a). We then define the invariants

$$s=(p_1+p_2)^2, \qquad t=(p_3-p_1)^2, \qquad u=(p_3-p_2)^2, \qquad 2.2.2$$

and

$$f_{\pm}(u,t) \equiv 2\,((m_t^2 - u)^2 \pm (m_t^2 - t)^2) \qquad 2.2.3$$

Denoting by T_Z the amplitude for $e^+e^- \rightarrow Z^* \rightarrow t\bar{t}$, we find after summing over final spins and averaging over initial spins (neglecting the electron mass)

$$\frac{1}{4}\Sigma T_Z T_Z^+ = N_c\,((|A_e^Z|^2 + |B_e^Z|^2)\,((|A_t^Z|^2 + |B_t^Z|^2) f_+(t,u) + 4(|A_t^Z|^2 - |B_t^Z|^2) m_t^2 s)$$

$$+ 4\,\mathrm{Re}(A_e^Z B_e^{Z*})\,\mathrm{Re}(A_t^Z B_t^{Z*}) f_-(t,u)) \times \frac{1}{((s-M_Z^2)^2 + \Gamma_Z^2 M_Z^2)} \quad .$$

2.2.4

Likewise denoting by T_γ the amplitude for $e^+e^- \to \gamma^* \to t\bar{t}$, we find

$$\frac{1}{4}\Sigma\, T_\gamma T_\gamma^+ = N_c\,|A_e^\gamma|^2\,|A_t^\gamma|^2\,(f_+(t,u) + 4m_t^2 s)\frac{1}{s^2},$$

2.2.5

and the interference term between T_Z and T_γ is

$$\frac{1}{4}\Sigma(T_Z T_\gamma^+ + T_\gamma T_Z^+) = N_c\, A_e^\gamma\, A_t^\gamma (A_e^{Z*}\, A_t^{Z*}(f_+(t,u) + 4\, m_t^2 s) + B_e^{Z*} B_t^{Z*} f^-(t,u))$$

$$\times 2\,\frac{(s-M_Z^2)}{s((s-M_Z^2) + \Gamma_Z^2\, M^{Z^2})} \quad .$$

2.2.6

In eqs. (2.2.4)-(2.2.6), Γ_Z is the width of Z and N_c is the number of colours (=3). For a fermion f (=t or e) A_f^Z, B_f^Z, and A_f^γ are the standard model couplings to the Z and γ

$$A_Z^f = \frac{g_W}{2\cos\theta_W}(T_3^f - 2Q_f \sin^2\theta_W), \quad B_Z^f = \frac{g_W}{2\cos\theta_W} T_3^f \quad .$$

$$A_\gamma^f = e_f$$

2.2.7

In the subsequent analysis we use the following cuts: Jets are identified using the jet algorithm defined in Chapter 1. Guided by jet + $\not{p}_T$ searches in e^+e^- annihilation (28), we use the values for the jet algorithm parameters: p_T^0=3GeV, $|\cos(\theta_0^*)|$=0.8, and Δ_0=30°. We require that in order for a lepton to be detected, $p_T(l)>p_T^0(l)=3GeV$ and that $|\cos(\theta_l^*)|<|\cos(\theta_l^*{}_0)|=0.8$ and in addition that each lepton be separated from any jet by an isolation angle $\theta_{jl} \geq \theta_l^0=10^o$. Finally we require all events to have a total missing momentum $\not{p}_T \geq \not{p}_T{}^0=5GeV$.

In our analysis we consider events with at least three jets in order to reduce standard model backgrounds of the form $e^+e^- \rightarrow q\bar{q}$. In particular, we look for events where one of the $t,\bar{t}$ decays semileptonically (for example $t \rightarrow bl^+\nu_l$) and the other decays into jets (for example $t \rightarrow bq\bar{q}'$). When b quarks from such a decay themselves decay hadronically, the decay products tend to be collimated hence they form a single jet.

Figure 2.1(b) shows the cross section σ for $e^+e^- \rightarrow t\bar{t}$ with one of the $t,\bar{t}$ decaying semileptonically and the other into jets for various values of m_t. We note that for high values of $\sqrt{s}$ ($\geq 100GeV$), in addition to $e^+e^- \rightarrow Z^* \rightarrow t\bar{t}$, $e^+e^- \rightarrow \gamma^* \rightarrow t\bar{t}$, is also important eqs. 2.2.5-2.2.7. We see that for each m_t there 's an optimal value of s, which we denote s_0, for which σ has a maximum $\sigma_{\max}$. For m_t in the range $30<m_t<40GeV$, one has $\sqrt{s_0}=M_Z$; as m_t increases beyond $45GeV$, $\sqrt{s_0}$ increases. Figure 2.1(b) shows that for $m_t=30GeV$, $\sigma_{\max}$ $10^3 pb$; for $m_t=40GeV$, $\sigma_{\max}=3\times10^2 pb$; while for $m_t=50GeV$, $\sigma_{\max}$ drops to $3pb$ and for $m_t=60GeV$, $\sigma_{\max}=1.8pb$.

Now consider a multi-jet event and select a particular subset of the jets. Define E_J and $\vec{P}_J$ to be the total energy and the total 3-momentum of the selected jets, and

$$m_J=\sqrt{E_J^2-\vec{P}_J^2}$$

2.2.8

To find the mass of the top-quark from experimental data, proceed as follows

(a) First select the events in which the final products of the t and $\bar{t}$ decays contain only one neutrino as in figure 2.1(a); such events can be selected because the missing energy $\not{E}$ equals the missing momentum $\not{p}$. We find that they consist of about 8% of the total number of events.

(b) Next, for such events, if the final state contains four jets, calculate the invariant mass m_J of each possible combination of three jets, and record it on a histogram. From figure 2.1(a) we see that for the combination of three jets arising from $\bar{b}$, q, and $\bar{q}'$, we have $m_J=M_t$

(c) If the final state contains three jets, calculate m_J for all two jet combinations, and record it on a histogram. Again, from figure 2.1(a) we see the following: First, suppose that the three jets arise by coalescence of two of the jets of $\bar{b}$, q, and $\bar{q}'$ into one jet, then for the combination which includes that jet and the other parton from that set, $m_J=m_t$. Second, suppose that the jet arising from the b-quark of $t\to bl^+\nu_l$ fails to qualify as a jet because, for example $p_t(j)\le p_t^0$; then if $\bar{b}$, q, $\bar{q}'$ lead to three jets, we shall have $m_J=m_t$ as well. Of course if the b jet coalesces with one (or more) of the jets of $\bar{b}$, q, $\bar{q}'$ then $m_J\neq m_t$.

Figure 1(c) shows cross sections σ_{max} for three and for jets at $s=s_0$ as a function of m_t.

Figure 2.2 shows the histograms as a function of m_J obtained by the above method. For m_t=30GeV we show the histogram for both four-jet and three-jet events (dashed line) while for m_t= 40, 50, and 60GeV, we show the histogram for four jet events only.

From this we see that four-jet events always give a strong peak at $m_j = m_t$ while for 3-jet events the peak is less prominent and may appear elsewhere.

Now figure 2.1(c) (two lower curves, the number of neutrinos, $N_\nu=1$) shows that the four-jet cross section is sizable for $m_t<45GeV$; with a luminosity $L=1.6\times 10^{31} cm^{-2}s^{-1}$ in one day's real running time (29) we expect >1 event. This suggests that the above method is more useful only if $m_t \leq 45GeV$.

Moreover, the above method assumes that events with $N_\nu=1$ can be separated from those with $N_\nu \geq 1$ by the requirement that $\not{E}=\not{p}$. If $m_t \geq M_Z/2$, energies above M_Z are necessary, and photon bremsstrahlung becomes important. The photons will tend to go along the beams, and $\not{E}$ will not be well determined.

To see this effect, we first estimate the cross section σ_γ for bremsstrahlung of a photon of momentum k with $k_{min} < k \leq k_{max} = (s-4m_t^2)/2\sqrt{s}$, radiated with respect to the beams at an angle $\theta^* < \theta_0^*$. Most of σ_γ arises when the γ is approximately collinear with $e^\pm$. Then we find

$$\sigma_\gamma(s) = 2\frac{\alpha}{\pi}\frac{1}{s}\int_{k_{min}}^{k_{max}} dk\, k\, (2 + \frac{s}{k^2} - 2\frac{\sqrt{s}}{k}) \ln\frac{(1-|\cos\theta_0^*|)\, s}{2\, m_e^2}\sigma(s-2k\sqrt{s}) \quad . \tag{2.2.9}$$

Consider for example m_t=50GeV; then from figure 2.1(b) the optimal energy is $\sqrt{s_0}$=110 GeV (maximum σ). Taking k_{min}=1GeV we find σ_γ=0.21σ. Note that because of the logarithmic dependence of 2.2.9 this result will not be strongly effected by the exact value of k_{min}. Physically this means that if a photon contributes less than 1GeV to the missing energy we suppose that the event will be effectively the same as if it were without such a photon. If it contributes more than 1GeV it will be counted as a N_ν>1 event which therefore means that the events with N_ν=1 should be reduced by 21%. However in an experiment N_ν=1 events would be indistinguishable from events with N_ν>1 and $E-|p|\leq k_{min}$ and therefore such events should be added. The result is shown in figure 2.2 (dash dotted line). Although the peak at $m_J=m_t$ (=50GeV) is still prominent, the m_J distribution is somewhat smeared out. Thus, if $m_t\geq$45GeV it is advisable to proceed with an alternative method.

Since in the above we are throwing out 82% of the events where N_ν>1, in the case of larger m_t where the event rate is low, it would be very helpful if we could find some way to include these events. Doing this we could increase the four-jet and three-jet cross sections by about one order of magnitude (figure 2.1(c), upper curves).

Applying the above method to events with $N_\nu\geq$1, we find that for four-jet events there is still a peak at $m_J=m_t$ but significantly broader hence identification of the top-quark and determination of m_t become more difficult. Thus to consider $N_\nu\geq$1 events, we follow a different procedure.

First denoting by E_Z and $\vec{P}_Z$ the energy and momentum of Z, we define

$$\tilde{m}_J \equiv \sqrt{(E_Z - E_J)^2 - (\vec{P}_Z - \vec{P}_J)^2}$$

2.2.10

Next, we consider the four-jet and three-jet events for $N_\nu \geq 1$ and their distribution in the $m_J - \tilde{m}_J$ plane; this is shown for $m_t = 50 GeV$ in figure 2.3(a). We see that there is a concentration of events in a square of about $10GeV \times 10GeV$ with $m_J \leq m_t$ and $\tilde{m}_J \geq m_t$. Most of the events plotted in this square are, in fact, from correct combinations (ie. like $\bar{b}$, q, and $\bar{q}'$, figure 2.1(a)), and it turns out that 75% of the correct combinations are to be found in this square. Incorrect combinations scatter continuously through the allowed range of the $m_J - \tilde{m}_J$ plane. Thus, we proceed by selecting events only in this square; their detailed distribution is shown in figure 2.3(b).

For events satisfying these cuts, we now consider averages between m_J and $\tilde{m}_J$ of the form

$$M(x) = (1-x)m_J + x\tilde{m}_J$$

2.2.11

for various values of the parameter x, $0 \leq x \leq 1$. With reference to figure 2.3(b), this average amounts to a projection along an axis defined by the value of x. Figure 2.3(b) also shows that for $m_t = 50 GeV$ there is a relative concentration of events along the axis corresponding to $x \sim 0.45$. For $m_t = 30 GeV$, we find a similar concentration along $x \sim 0.22$, etc.. This suggests that for each m_t there is an optimal value of x such that the histogram versus $M(x)$ shows the most prominent peak.

Figure 2.1(d) shows as a function of m_t the value of x denoted by x_0, which produce the most prominent peak in the histogram vs $M(x_0)$. Then figure 2.4, for m_t=30, 40, 50, and 60GeV shows the histogram vs $M(x_0)$ for the above values of x_0; there is evidentially a prominent peak for all these values of m_t

To summarize, for not too large $m_t(\leq 45GeV)$, we determine m_t via a histogram versus m_J for events with N_μ=1 only. For larger m_t, we first plot the events in the m_J–$\tilde{m}_J$ plane; a concentration occurs which gives an approximate value of m_t. Next, we introduce an additional cut corresponding to a square of about $10GeV\times 10GeV$, we use this approximate value to determine a value of x_0 as in figure 2.1(d); and, finally, we construct a histogram for the number of events versus $M(x_0)$. The value of m_t arises as a prominent peak in this histogram.

Within the standard model, background to $e^+e^-\to jets + l + \not{p}$ may arise first from $e^+e^-\to b\bar{b}$ with b and/or $\bar{b}$ decaying semileptonically. However, because of the smallness of m_b, the products of the b and of the b decay will be very collimated; this will give rise to two-jet back-to-back events in the e^+e^- center of mass system. Since we look for events with three or four jets, such a background will be practically absent.

More important is the background from $e^+e^-\to bb$ + $gluons$; the cross sections are of order α_s or higher as compared with $e^+e^-\to t\bar{t}$ but for relatively low $p_T(j)$ they may be substantial. On the other hand, considering, for example, $e^-e^+\to b\bar{b}g$ with $b\to c\bar{\nu}_l l^-$, we note that because of our lepton isolation cut in θ_l^0 and of the smallness of m_b, b must be rather soft and the gluon must be rather hard.

We have determined the cross section for $e^+e^- \to b\bar{b}g$ (three jets) subject to our acceptance cuts, corresponding to each value of m_t (figure 2.1(c) dotted line). Clearly it is more than 1 order of magnitude smaller than $e^+e^- \to t\bar{t}$ for $N_\nu \geq 1$. Thus it cannot significantly interfere with our results when we apply the method discussed earlier that uses $N_\nu \geq 1$ data. In this calculation we numerically determined the amplitude using the Weyl basis method described in section 1.4.

Compared with $e^-e^+ \to t\bar{t}$ for $N_\nu = 1$, this background is significant (figure 2.1(c)). However, its m_J distribution is different. This is shown as an example for $m_t = 30 GeV$ in figure 2.2 (dotted lines): whereas $e^-e^+ \to t\bar{t}$ peaks at $m_J < \sqrt{s}/2$, $e^+e^- \to b\bar{b}g$ shows some peak at $m_J > \sqrt{s}/2$. The latter is due to the lepton isolation cut which, as mentioned, forces b to be soft causing the invariant mass of $\bar{b}$, g to be large.

For $m_t > M_Z/2$, the background from $b\bar{b}g$ decreases in importance (figure 2.1(c)) since the optimal $\sqrt{s}$ increases and it is less likely that b will be soft enough to give an isolated lepton.

Finally, for $e^+e^- \to b\bar{b}gg$, which is of higher order in α_s, the cross section is estimated to be smaller by an order of magnitude (30).

Let us now consider $t\bar{t}$ production in a hadron collider through events of the type $p\bar{p}\to t\bar{t}+X$ with one of the $t, \bar{t}$ decaying semileptonically and the other into jets. Thus, for example,

$$\begin{aligned} p\bar{p} \to t &+ \bar{t} + X \\ &\quad \to \bar{b}q\bar{q}' \\ &\to bl^{-}\bar{\nu}_l \end{aligned}$$

2.3.1

As before, the neutrino manifests itself by some missing transverse momentum $\not{p}_T$ and some of the jets associated with b, b, q, q' may coalesce or be rejected by our jet algorithm. We therefore look for events of the type

$$p\bar{p} \to t\bar{t} + X \to n\ jets + l + \not{p}_t + X$$

2.3.2

with n=3 or 4. We intend to show that, with proper procedures, top-quarks with $m_t \leq 40GeV$ can be identified at $Sp\bar{p}S$ $(\sqrt{s}=630GeV)$ and $m_t \leq 80GeV$ at the tevatron $(\sqrt{s}=2TeV)$. Our procedures are similar to those of section 2.2.

To determine the jets, we use our jet algorithm except that we take rapidity instead of angle as described in section 1.5. The parameters we take are $p^0_t(j)=7GeV$; $|y|\leq y_0=2.5GeV$ and for the jet separation, $\Delta R_{ij}=\sqrt{\Delta y^2+\Delta\varphi^2} > \Delta_0=1$. Furthermore, we require the lepton be produced with transverse momentum exceeding $p^0_t(l)=12GeV$ and with center of mass rapidity $|y(l)|<y_0(l)=2.5$; and the lepton be separated

from each jet by $\Delta R(lj)>\Delta R_0(lj)=0.5$. Finally we introduce a missing momentum cut $\not{p}_t>\not{p}_t^0=4GeV$.

We now define mass variables analogous to those of section 2.2. Denote by p_l the lepton momentum and by E_i and $\vec{p}_i$ the energy and momentum of the jet $i(=1, \ldots ,n)$. Let us first consider the case n=4. For each subset of 3 of the final jets define as before the invariant mass m_J by:

$$m_J^2=(\sum_{i=1}^{n-1} E_i)^2 - (\sum_{i=1}^{n-1} \vec{p}_i)^2 \qquad 2.3.3$$

moreover, for the remaining jet define the quantity

$$\tilde{M}_J^2 = (E_n + |\vec{p}_l| + |\not{p}_t|)^2 - (\vec{p}_n + \vec{p}_l + \not{p}_t)^2; \qquad 2.3.4$$

for each such subset, m_J and $\tilde{M}_J$ are measurable quantities (31), m_J is identical with the quantity in section 2.2 while $\tilde{M}_J$ differs in that since we cannot use longitudinal momentum conservation on the parton subprocess, we must estimate the mass of the top-quark which decays semileptonically by using only the transverse part of the neutrino momentum.

Next consider n=3. First, for each subset of 2 of the final jets define m_J and $\tilde{M}_J$ as in (2.3.3) and (2.3.4), Finally, take all 3 of the final jets and define:

$$m_J^2 = (\sum_{i=1}^{3} E_i)^2 - (\sum_{i=1}^{3} \vec{p}_i)^2 \qquad 2.3.3a$$

and

$$\tilde{M}_J^2=(|\vec{p}_l|+|\vec{p}_T|)^2-(\vec{p}_n+\vec{p}_l+\vec{p}_T)^2;$$

2.3.4a

To explain our approach take first the simplest case that all the final quarks $b, \bar{b}, q, \bar{q}'$ produce only jets (none decays semileptonically). Beginning with n=4, suppose that in equation (2.3.3) the subset of 3 jets corresponds to b, q, and $\bar{q}'$; then $m_J=m_t$. Moreover in Eq. (2.3.4) if $|\vec{p}_T|=|\vec{p}|$, then $\tilde{M}_J=m_t$ as well. Thus considering the distribution of events in the $m_J-\tilde{M}_J$ plane, we expect to have a concentration at m_t m_t and $\tilde{M}_J \lesssim m_t$. On the other hand if in (2.3.3) one of the jets corresponds to b then m_J and $\tilde{M}_J$ will be quite different from m_t and in general from each other.

To further enhance the relative concentration, for each event we form all possible combinations of jets and calculate m_J and $\tilde{M}_J$. Then among all such combinations, we choose the one for which

$$|m_J-\tilde{M}_J| = \text{ minimum}$$

Calling the corresponding values m_0 and $\tilde{m}_0$. Then the distribution of events in the $m_0-\tilde{m}_0$ plane is expected to show an even stronger concentration at $m_0=m_t$ and $\tilde{m}_0 \lesssim m_t$.

Next we turn to the case n=3. First of all, assume that two of the jets coalesce. If these jets correspond to two of the jets of b, q and q', then the reasoning proceeds as before, On the other hand, if one of the coalescing jets corresponds to b, then m_J and $\tilde{M}_J$ will in general significantly differ from m_t and in general from each other so that the events where this happens will be scattered about the $m_0-\tilde{m}_0$ plane.

Finally, suppose that for one of the jets the transverse momentum

$|\vec{p}_T(j)|<p_T^0(j)$ and therefore n=3. If this jet corresponds to one of $\bar{b}$, q, or $\bar{q}'$, with the definitions (2.3.3), (2.3.4) we reason as before. If it corresponds to b, we use the definitions (2.3.3a) and (2.3.4a) to repeat the same reasoning.

Now assume that some of b, $\bar{b}$, q, $\bar{q}'$ decay semileptonically. Then $m_J<m_t$. Regarding $\tilde{M}_J$, in general we can have $\tilde{M}_J\leq m_t$ or $\tilde{M}_J>m_t$; for the 'correct' combination of jets therefore with respect to $\tilde{M}_J$ we expect a broader distribution. However, we can argue that for a large fraction of events, for the 'correct' combination of jets $|\tilde{M}_J-m_t|$ is not too large. The argument is as follows: (i) We are missing the longitudinal part of the momentum of the ν_l of the decay $t\rightarrow bl^+\nu_l$. (ii) Additional neutrinos may arise from the decays of b, q, or $\bar{q}'$; and their momenta will, in general, contribute to $\not{p}_T$. Factor (i) tends to make $\tilde{M}_J<m_t$; however, the effect should be rather small, because on the average only 1/3 of the energy of t goes to the neutrino, and 1/3 of the neutrino's momentum is longitudinal. Factor (ii) tends to make $\tilde{M}_J>m_t$; however, only a small fraction of the momentum of $\bar{b}$, q, $\bar{q}'$ is taken by the neutrinos of their decays as in the e^+e^- case. Thus, factor (ii) is expected to have a small effect, as well. In our Monte Carlo calculations, factor (i) and (ii) together were found to give on the average $|\tilde{M}_J-m_t|=10GeV$.

Thus our procedure to enhance the concentration should still work since we expect $m_0\approx\tilde{m}_0$ for the combination of events with all the selected jets arising from $\bar{t}$.

The reaction $p\bar{p}\rightarrow t\bar{t}$ proceeds via the subprocesses $q\bar{q}\rightarrow t\bar{t}$ and $gg\rightarrow t\bar{t}$; their cross sections are given in reference (32). We use the parton distributions of reference (33) (set 1) with 6 flavors and $Q^2=s$.

We introduce a K-factor of 2 into our results (34).

To illustrate our approach, figure 2.5(a) shows for $S\bar{p}pS$ and m_t=40GeV the distribution $d\sigma/\,dm\,d\tilde{M}$ of events in the m_J–$\tilde{M}_t$ plane; there is a concentration near m_J=$\tilde{M}_J$=m_t. Then figure 2.5(b) shows the corresponding distribution of $d\sigma/dm_0\,d\tilde{m}_0$ in the m_0–$\tilde{m}_0$ plane; now the concentration near m_0=$\tilde{m}_0$=m_t is significantly stronger. Figures 2.5(c) and (d) show $d\sigma/\,dm_0\,d\tilde{m}_0$ at the tevatron for m_t=40 and 60GeV. Note that in all of (b), (c), and (d) the distribution with respect to $\tilde{m}_0$ is broader.

Figure 2.6 shows the distributions $d\sigma/\,dm_0$ for various values of m_t; in each case there is a clear peak at m_0=m_t. The figure also shows the level of 1 event/GeV at $S\bar{p}pS$ corresponding to an integrated luminosity of 600 nb; and at the tevatron for $L=10^{-3}\,nb^{-1}\,s^{-1}$, six months operation at efficiency 1/3. Thus at $S\bar{p}pS$ if m_t=40GeV in the range $35\leq m_0\leq 45GeV$ we anticipate about 14 events; however, at the tevatron in a range $m_t-5\leq m_0\leq m_t+5GeV$ we anticipate at least hundreds of events for all m_t=30, 40, and 80GeV.

A possible background may arise from:

$$\bar{p}p \to W + gluons + X \tag{2.3.5}$$

with $W\to l^-\bar{\nu}_l$ and the gluons giving rise to jets. However with respect to our process, (2.3.5) is of order $\alpha_W\alpha_s$ and its cross section is therefore expected to be insignificant.

A more important background may arise from with, say, $b \rightarrow cl^- \bar{\nu}_l$ and $b \rightarrow jet$. We calculated the cross section for $p\bar{p} \rightarrow b + \bar{b} + gluons + X$ using the expressions of reference (35) for the subprocess $q\bar{q} \rightarrow q\bar{q}g$ and $gg \rightarrow q\bar{q}g$; then we calculate $b \rightarrow cl^- \nu_l$ taking $m_t = 50 GeV$. Figure 2.7 shows the distributions $d\sigma / dp_{t_l}$ vs p_{t_l} at $S\bar{p}pS$ and the tevatron. Clearly at low $p_{t_T} (\leq m_b)$ this background is substantial, but as p_{t_l} increases beyond m_b it decreases very fast. We qualitatively understand its shape in view of the smallness of m_b and of our lepton-jet separation cut $\Delta R(lj)$: Such a background event requires b to be soft so then p_{t_l} cannot much exceed m_b.

Similar remarks hold for the background $p\bar{p} \rightarrow b\bar{b}gg + X$, which, in fact should be somewhat smaller than $p\bar{p} \rightarrow b\bar{b}g + X$ since it involves one more gluon.

Our results of figure 2.7 suggest that we can somewhat reduce our acceptance cut in p_{t_l} to $p^0_{t_l} = 8 GeV$. At $S\bar{p}pS$ for $m_t = 40 GeV$, figure 2.6 shows (dashed line) the corresponding distributions; evidently the number of interesting events increases by a factor of about 2.

Figure Captions

Figure 2.1

(a) A graph for $e^+e^-\to t\bar{t}$ with t decaying semileptonically ($t\to bl^+\nu_l$) and $\bar{t}$ into jets ($\bar{t}\to\bar{b}q\bar{q}'$). (b) cross section for $e^-e^+\to t\bar{t}$ with one of the t , t bar decaying semileptonically and the other into jets. (c) Cross section for σ_{max} (ie at $s=s_0$) for three and four jets corresponding to $N_\nu=1$ and $N_\nu\geq 1$. Dotted line, cross section for the background $e^+e^-\to b\bar{b}g$. (d) The values x_0 of the parameter x (eq. 12) producing prominent peaks in the histogram versus $M(x_0)$.

Figure 2.2

Histograms vs m_J for $N_\nu=1$ with the method following Eq. (9), for m_t=30, 40, 50, 60GeV. The dotted line for m_t=30GeV shows the background $e^+e^-\to b\bar{b}g$.

Figure 2.3

(a) Distributions of three-jet and four-jet events with $N_\nu\geq 1$ in the $m_0-\tilde{m}_0$ plane for m_t=50GeV. Contours correspond to fixed number of events per GeV^2 in arbitrary normalization. (b) The same in more detail.

Figure 2.4

Histograms vs $M(x_0)$ with the procedure of including $N_\nu\geq 1$ for m_t=30, 40, 50, and 60 GeV.

Figure 2.5

a) Distribution $d\sigma/\,dm_J\,d\tilde{M}_J$ of events in the m_J–$\tilde{M}_J$ plane at $S\bar{p}pS$ for m_t=40GeV. Contours correspond to fixed number of events per GeV^2 in arbitrary normalization. b)Distribution $d\sigma/\,dm_0\,d\tilde{m}_0$ of events in the m_0–$\tilde{m}_0$ plane, as before (m_t=40GeV) ; same normalization. c)The same as for b), but at the tevatron (m_t=40GeV); arbitrary normalization. (d) As for (c) but with m_t=60GeV.

Figure 2.6

Distributions $d\sigma/dm_0$ vs m_0 at $S\bar{p}pS$ at the tevatron. Solid lines correspond to acceptance cut $p_t(l)$=12GeV; dashed line (at $S\bar{p}pS$) to $p_t^0(l)$ 8GeV. Dash-dotted lines denote levels of 1 event/GeV with integrated luminosities as in the text.

Figure 2.7

Distributions $d\sigma/\,dp_{l_t}$ vs the transverse momentum p_{l_T} of the lepton. Dash-dotted line: at $S\bar{p}pS$; solid lines: at the tevatron. Dashed lines denote the background from $p\bar{p}\rightarrow b\bar{b}g+X$ with b or $\bar{b}$ decaying semileptonically.

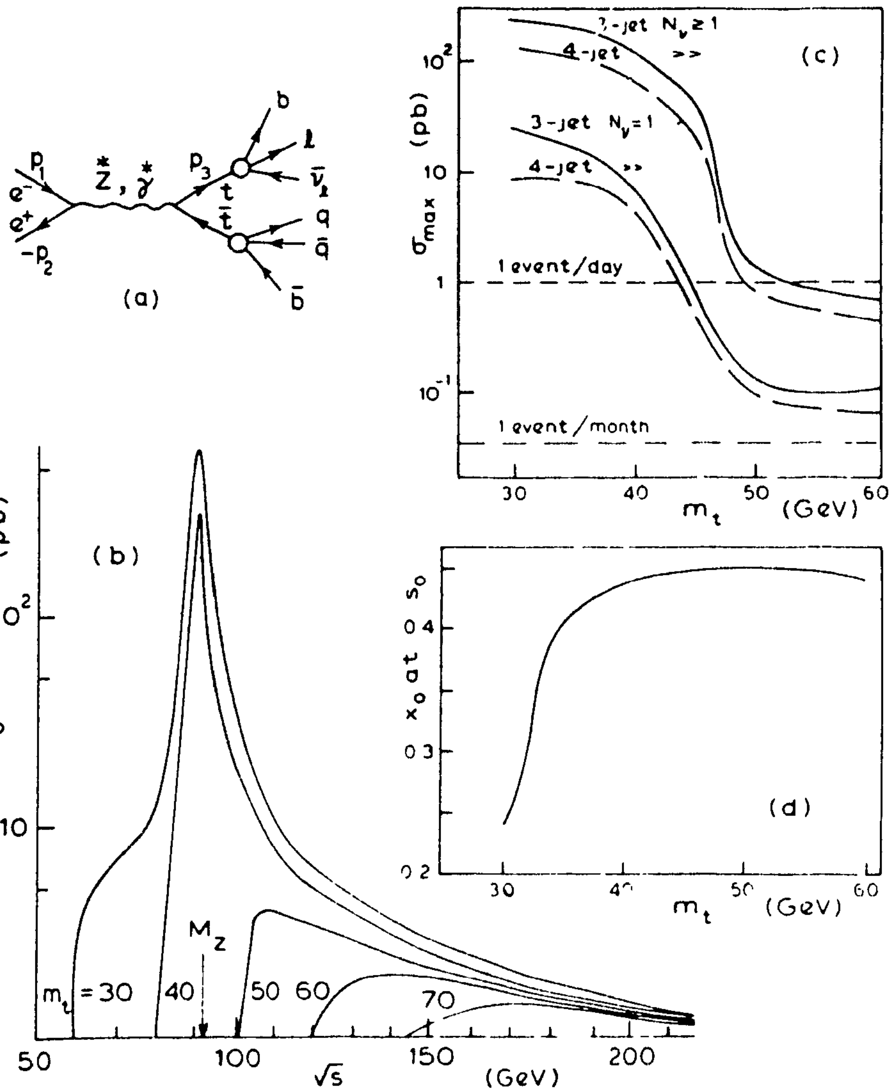
p1
e−
e+
−p2
Z*, γ*
p3
t
t̄
b
ℓ
ν̄ℓ
q
q̄
b̄
(a)
σ (pb)
(b)
10²
10
M_Z
m_t = 30
40
50
60
70
50
100
150
200
√s
(GeV)
3-jet N_ν ≥ 1
4-jet >>
(c)
3-jet N_ν = 1
4-jet >>
σ_max (pb)
10²
10
1
10⁻¹
1 event/day
1 event/month
30
40
50
60
m_t (GeV)
x₀ at s₀
0.4
0.3
0.2
(d)
30
40
50
60
m_t (GeV)

Figure 2.1

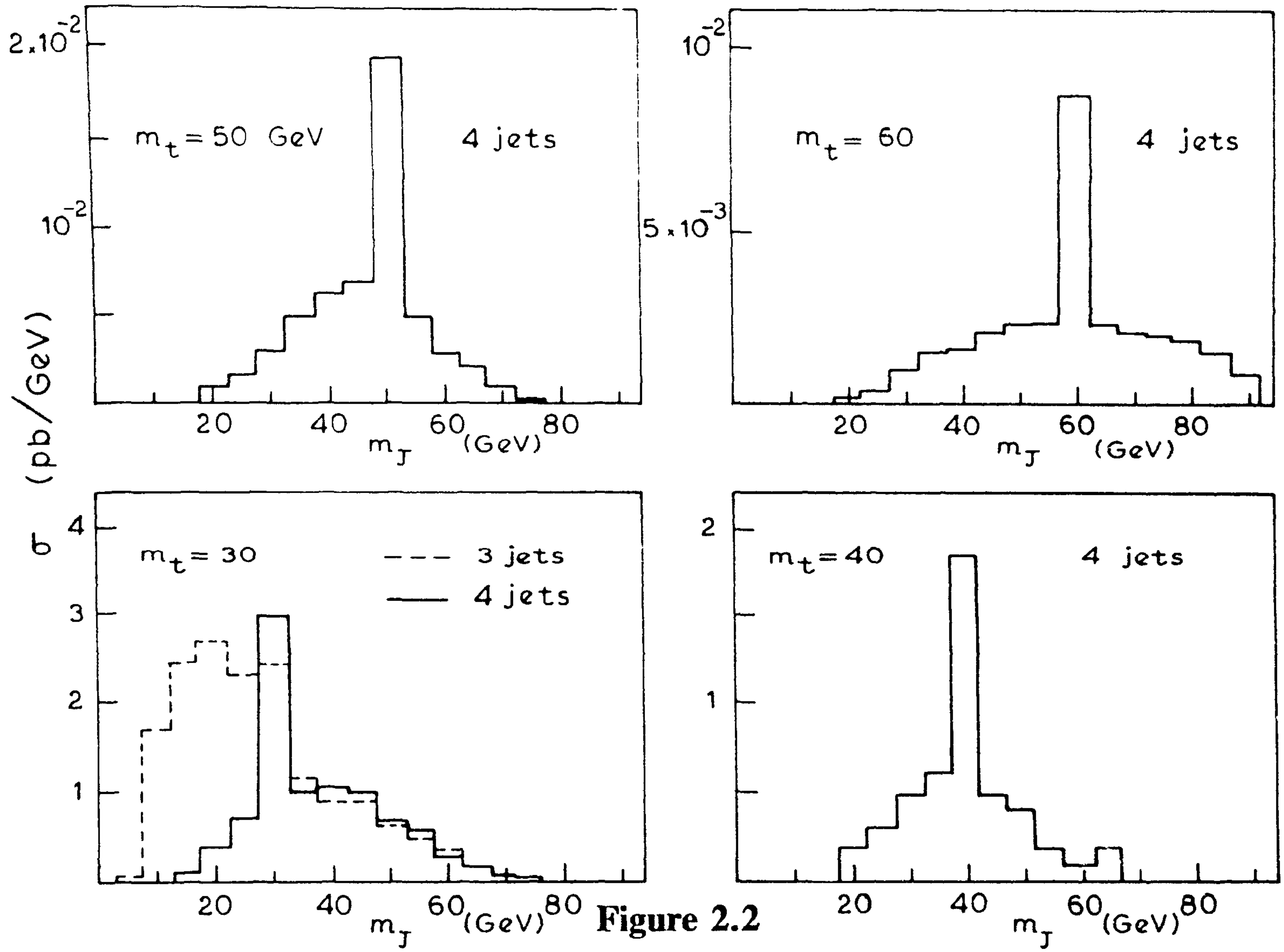
2.10^-2
10^-2
(pb/GeV)
σ
m_t = 50 GeV
4 jets
20
40
60
80
m_J
(GeV)
10^-2
5.10^-3
m_t = 60
4 jets
4
3
2
1
m_t = 30
3 jets
4 jets
2
1
m_t = 40
4 jets

Figure 2.2

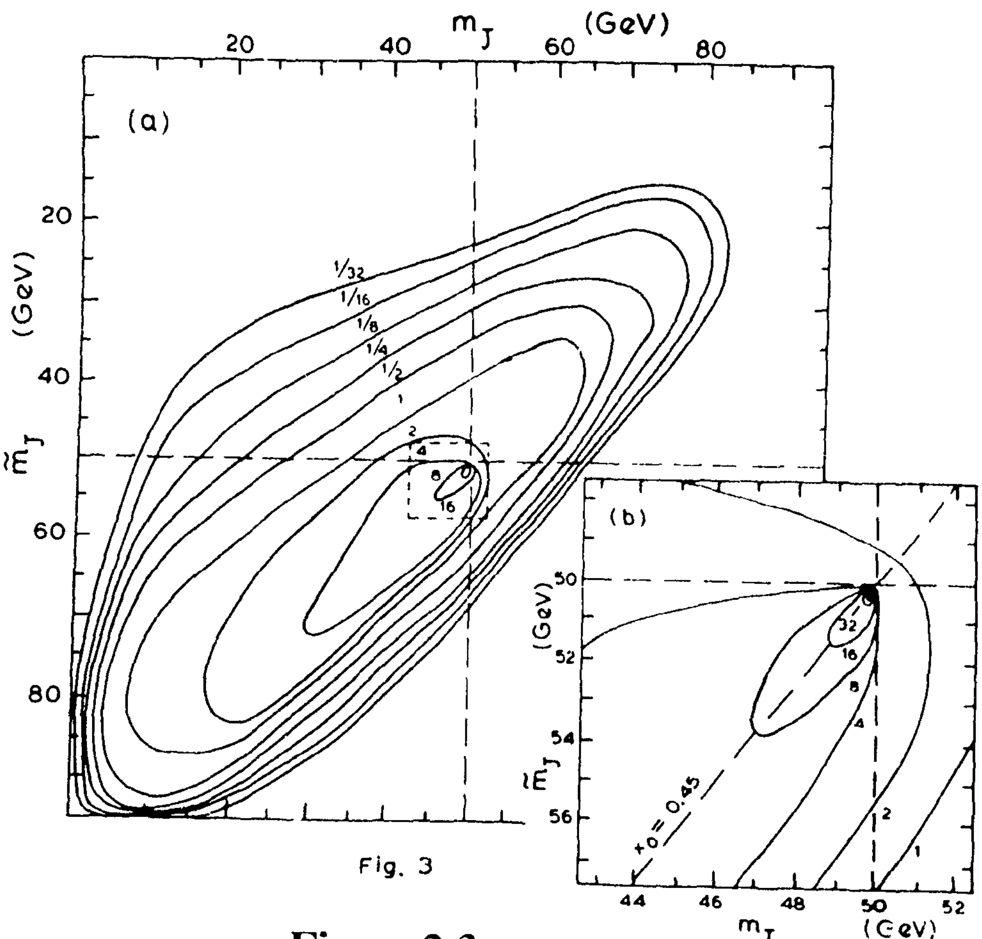

m_J (GeV)
20
40
60
80
(a)
20
40
60
80
$\tilde{m}_J$ (GeV)
1/32
1/16
1/8
1/4
1/2
1
2
4
8
16
Fig. 3
(b)
50
52
54
56
$\tilde{m}_J$ (GeV)
32
16
8
4
2
1
$x_0 = 0.45$
44
46
48
50
52
m_J (GeV)

Figure 2.3

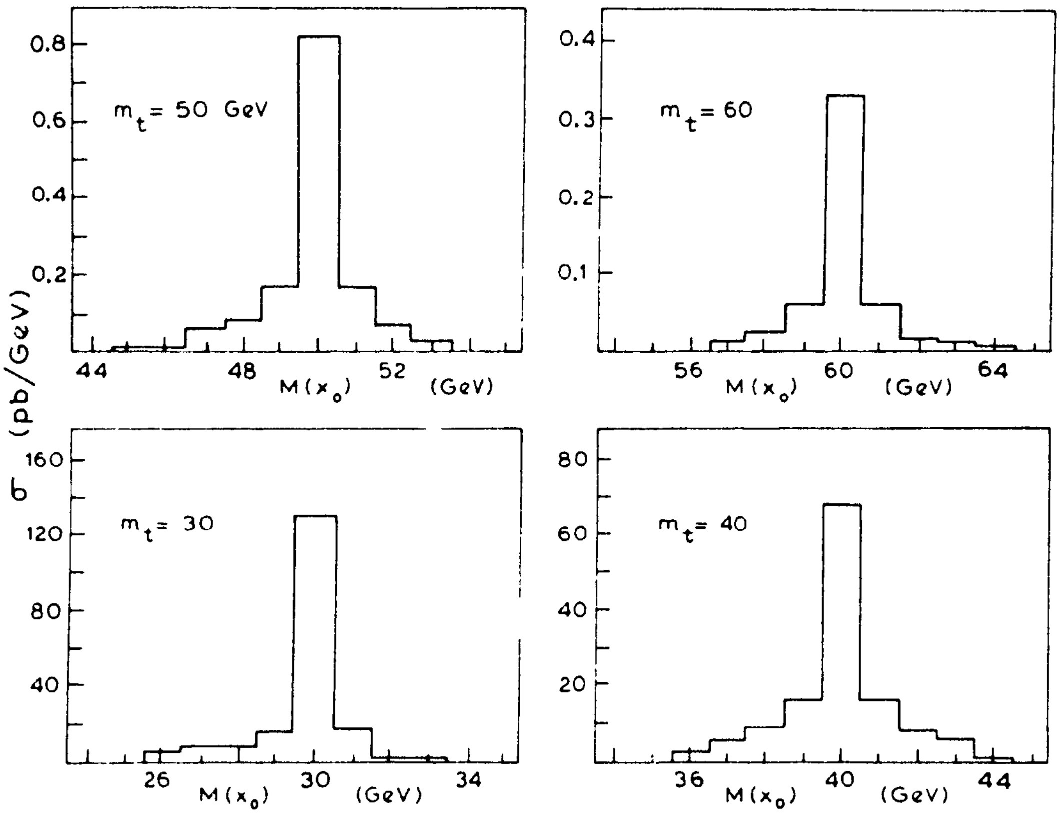

σ (pb/GeV)
m_t = 50 GeV
0.8
0.6
0.4
0.2
44
48
52
M (x_0)
(GeV)
m_t = 60
0.4
0.3
0.2
0.1
56
60
64
M (x_0)
(GeV)
m_t = 30
160
120
80
40
26
30
34
M (x_0)
(GeV)
m_t = 40
80
60
40
20
36
40
44
M (x_0)
(GeV)

Figure 2.4

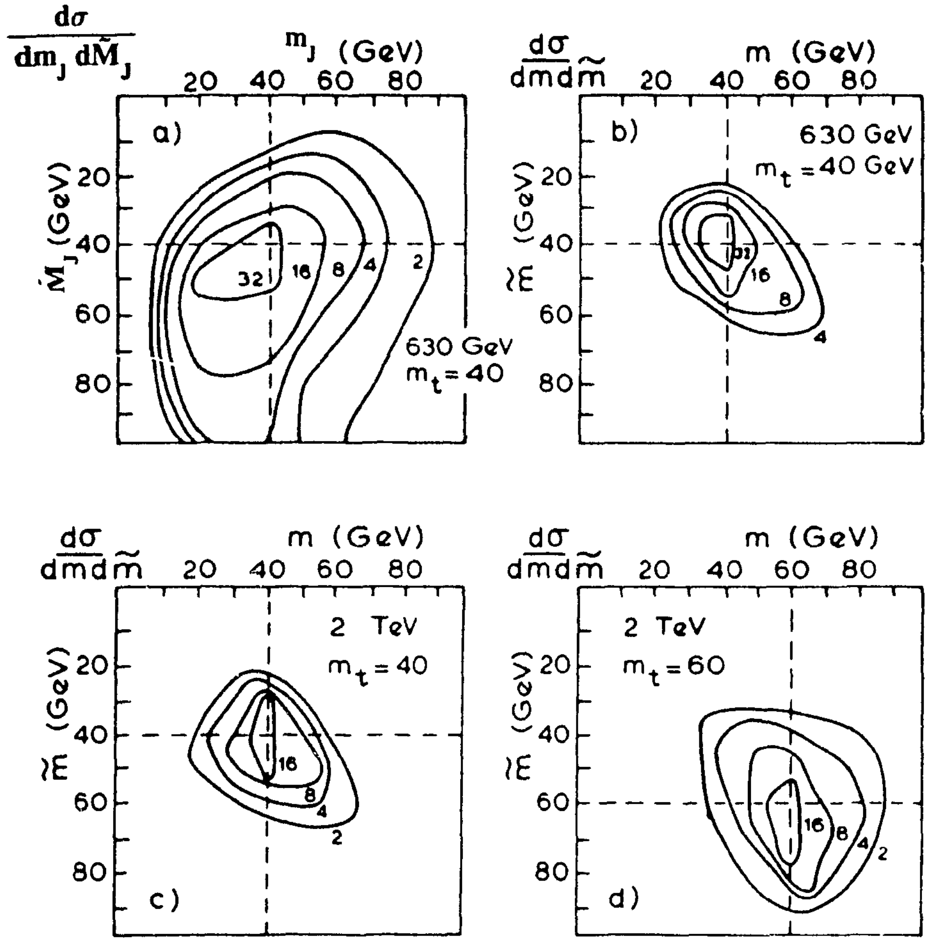

$\frac{d\sigma}{dm_J\, d\tilde{M}_J}$
m_J (GeV)
20 40 60 80
a)
$\tilde{M}_J$ (GeV)
20
40
60
80
32
16
8
4
2
630 GeV
$m_t = 40$
$\frac{d\sigma}{dm\, d\tilde{m}}$
m (GeV)
20 40 60 80
b)
630 GeV
$m_t = 40$ GeV
$\tilde{m}$ (GeV)
20
40
60
80
32
16
8
4
$\frac{d\sigma}{dm\, d\tilde{m}}$
m (GeV)
20 40 60 80
2 TeV
$m_t = 40$
$\tilde{m}$ (GeV)
20
40
60
80
16
8
4
2
c)
$\frac{d\sigma}{dm\, d\tilde{m}}$
m (GeV)
20 40 60 80
2 TeV
$m_t = 60$
$\tilde{m}$ (GeV)
20
40
60
80
16
8
4
2
d)

Figure 2.5

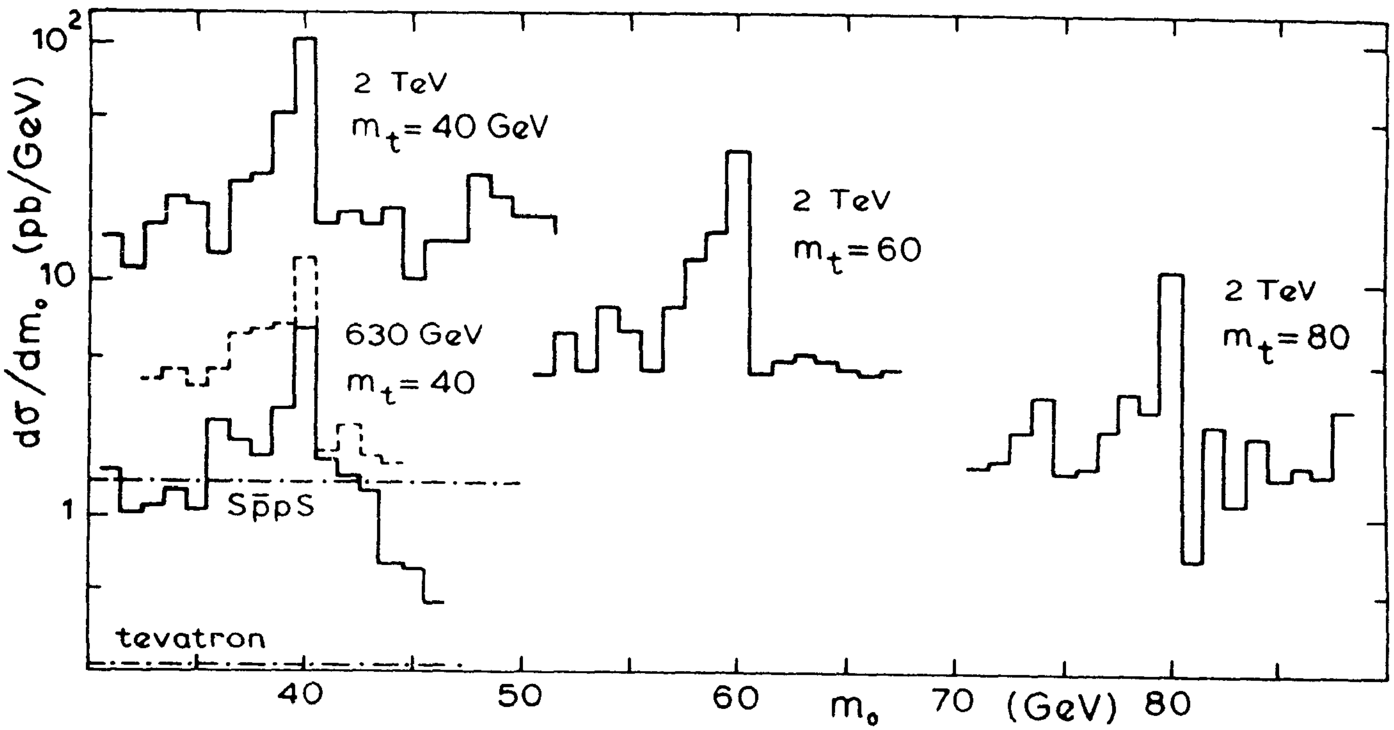

10^2
10
1
$d\sigma/dm_0$ (pb/GeV)
2 TeV
$m_t = 40$ GeV
630 GeV
$m_t = 40$
$S\bar{p}pS$
tevatron
2 TeV
$m_t = 60$
2 TeV
$m_t = 80$
40
50
60
m_0
70 (GeV) 80

Figure 2.6

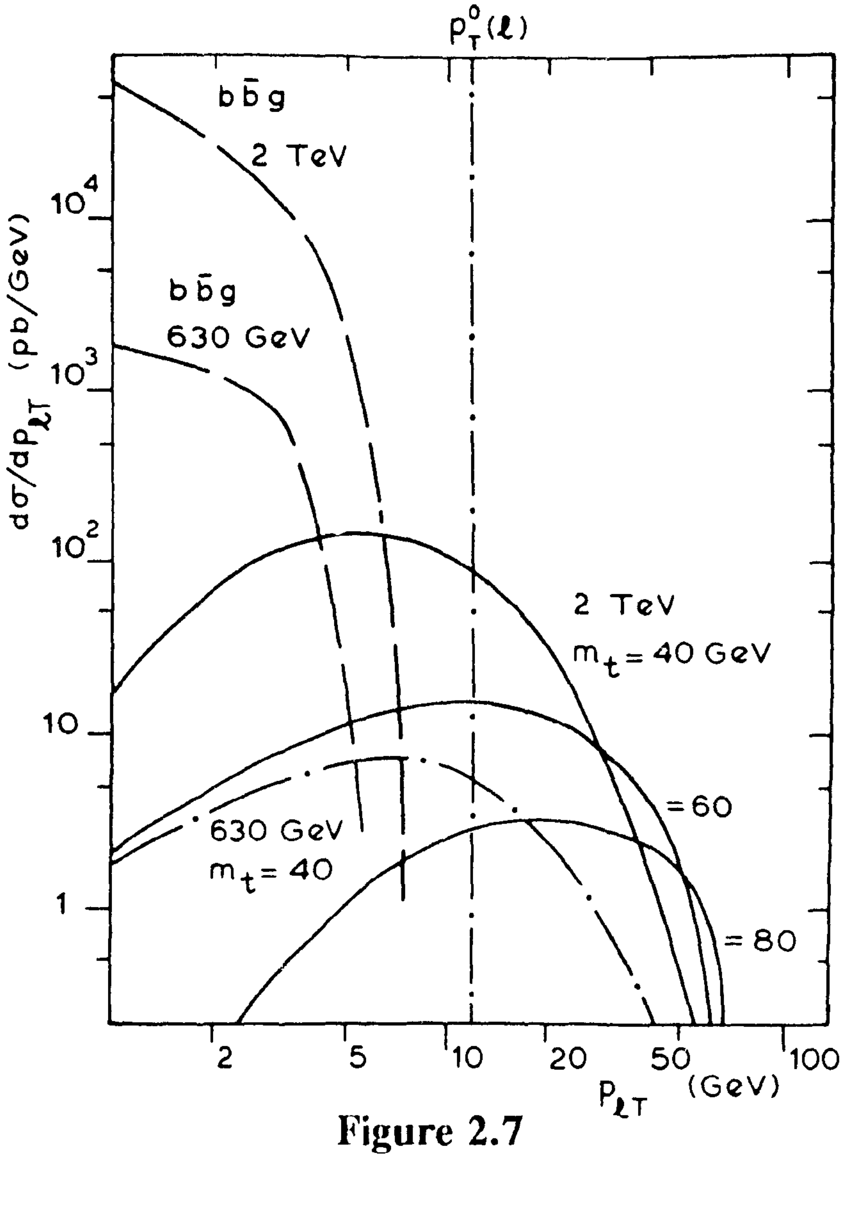

$p_T^0(\ell)$
b b̄ g
2 TeV
b b̄ g
630 GeV
2 TeV
$m_t = 40$ GeV
= 60
630 GeV
$m_t = 40$
= 80
10^4
10^3
10^2
10
1
$d\sigma/dp_{\ell T}$ (pb/GeV)
2
5
10
20
50
100
$p_{\ell T}$ (GeV)

Figure 2.7

CHAPTER 3

HIGGS PRODUCTION AT OR NEAR THE Z PEAK IN ELECTRON-POSITRON ANNIHILATION

3.1 Introduction

In this chapter we are concerned specifically with detecting a Higgs-boson that has a mass in the light range discussed in Chapter 1, in particular $10GeV \leq m_H \leq M_Z$. Perhaps the first opportunity to detect such a Higgs-boson will be in electron-positron colliders operating at the Z peak (such as SLC or LEP) through the reaction $e^+e^- \rightarrow Z \rightarrow HZ^*$, where Z^* denotes a virtual Z . Assuming that $m_H > 10GeV$, the Higgs-boson decay is dominated by $H \rightarrow b\bar{b}$ while if $3GeV < m_H < 10GeV$ $H \rightarrow c\bar{c}$ will be the dominant decay mode.

There are in general three main decay modes for the Z^*. $Z^* \rightarrow l^+l^-$ (l^- = a charged lepton), $Z^* \rightarrow \nu_l\bar{\nu}_l$ and $Z^* \rightarrow q\bar{q}$. The cross section for these processes are shown in figure 3.2.

If $Z^* \rightarrow l^+l^-$ and $l^\pm = e^\pm$ or $\mu^\pm$, then $e^+e^- \rightarrow Z^0 \rightarrow l^+l^-$ has a particularly clean signature, 2 jets and l^+l^-, although the rate is lower than $Z^* \rightarrow \nu\bar{\nu}$. This has been studied extensively in references (36)-(39)

In the case of $Z^* \rightarrow q\bar{q}$ there is a high event rate however the signal is less clean since the final state ($q\bar{q}b\bar{b}$) consists of 4 jets and is subject to standard model background from $Z \rightarrow q\bar{q}gg$.

If $Z^* \rightarrow \nu\bar{\nu}$, the event rate is higher than $Z^* \rightarrow l^+l^-$ and the signal is relatively clean, 2 jets and either missing momentum or missing energy arising from the undetected neutrinos. Thus, using this method one could in principle hope to reach slightly higher values of m_H than using $Z \to l^+l^-$. In this chapter we will focus on this final mode as a method of searching for a light Higgs-boson at a electron-positron collider at or near the Z peak.

In addition to these events (signal) of the form

$$e^+e^- \to Z \to H\nu\bar{\nu}, \quad H \to q\bar{q} \qquad 3.1.1$$

we study possible standard model backgrounds; and by introducing certain mass and energy variables, and making use of the properties of the distributions with respect to these variables, we show how to practically eliminate or at least reduce these backgrounds by the introduction of proper acceptance cuts. In suggesting some of these cuts we are guided by similar procedures of the UA1 and UA2 collaborations in their analyses of collider events.

Production of the Higgs-boson from Z decay may not be the only way to observe the Higgs-boson in electron-positron colliders. If the top-quark exists, as is required in the standard model, one would anticipate toponium (T) formation so that another important channel for Higgs-boson production is $e^+e^- \to T \to H\gamma$. We shall compare Higgs-boson production via the latter channel to that via (3.1.1) in the case where $m_t < M_Z/2$.

The outline of this chapter is as follows: In sect. 3.2 we briefly review some properties of the Higgs-boson and analyze the process $e^+e^- \to H f\bar{f}$ (f=fermion). In particular we study the distribution of the events (3.1.1) with respect to certain kinematic variables which we define. In sect 3.3 we study the background from $e^+e^- \to \nu\bar{\nu}q\bar{q}$ (q=quark) which is the main background if $m_t > M_Z/2$. We show that with a judicious choice of cuts it can be practically eliminated. In Sect. 3.4 we study a possible background from $e^+e^- \to Z \to t\bar{t}$ which is present if $m_t < M_Z/2$; we show how it can be reduced by a series of acceptance cuts. In sect. 3.5 we consider production of the Higgs-boson though the toponium resonance, a method which would also be useful if $m_t < M_Z/2$. Section 3.6 contains our conclusions.

3.2 Higgs Production at The Z Peak

In the standard model, the coupling of the Higgs-boson to a quark q is given by $g_{Hqq}=g_W m_q/2M_W$ hence, the width Γ_H for the decay $H\rightarrow q\bar{q}$ is:

$$\Gamma_H=\frac{N_c\, g_W^2\, m_H\, m_q^2}{32\pi M_W^2}\left(1-4\frac{m_q^2}{m_H^2}\right)^{\frac{3}{2}}$$

3.2.1

where $g_W=e/\sin\theta_W$ and N_c is the number of colors. The cases of interest here correspond to $m_q<<M_W$ (m_q is the mass of the b quark or lighter) so that Γ_H is very small ($\sim 0.6\times 10^{-4}\ m_H$).

To the lowest order, the generic process $e^+e^-\rightarrow Z\rightarrow Hf\bar{f}$ proceeds via the graphs of figure 3.1a. When the final state fermion f is not the t-quark only the first graph is important. Introducing the invariants (4-momenta defined in figure 3.1a)

$$t_i=(p_1-p_i)^2 \qquad u_i=(p_2-p_i)^2 \qquad i=5,\ 6,$$

3.2.2

after averaging over the initial and summing over the final spins, we obtain the squared matrix element $|M|^2$ (with $m_f=0$):

$$\frac{1}{4}\Sigma MM^+ = 2\, g_W^2\, \frac{M_Z^4}{M_W^2}[(|A_Z^e|^2+|B_Z^e|^2)(|A_Z^f|^2+|B_Z^f|^2)(u_5t_6+t_5u_6)$$

$$+\,4\ \mathrm{Re}(A_Z^eB_Z^e{}^*)\ 4\ \mathrm{Re}(A_Z^fB_Z^f{}^*)(u_5t_6-t_5u_6)]\frac{1}{(q^2-M_Z^2)^2+\Gamma_Z^2M_Z^2}\,\frac{1}{(p_4^2-M_Z^2)^2+\Gamma_Z^2M_Z^2}$$

3.2.3

The standard model values for the coupling of the Z to a fermion f (e, ν, or q) are given in section 1.2 by

$$A_Z^f=\frac{g_W}{2\cos\theta_W}(T_3^f - 2Q_f\sin^2\theta_W), \quad B_Z^f=\frac{g_W}{2\cos\theta_W}T_3^f \ .$$

3.2.4

and the H-Z coupling is $g_{HZZ}=g_W M_Z^2/M_W$ (see section 1.2).

Applying (3.2.3) at $q^2=M_Z^2$ we obtain as functions of m_H the total cross sections of figure 3.2. In $e^+e^-\rightarrow Hq\bar{q}$ we have summed over the quark contributions (q=u,d,s,c,b) and multiplied by the number of colors $N_c=3$ (we use $M_Z=91.6GeV$, $\Gamma_Z=2.81GeV$ and $\sin(\theta_W)=0.21$). Our results are in agreement with references (37),(38). We are interested in $e^+e^-\rightarrow Z^*\rightarrow H\nu\bar{\nu}$. and with a luminosity $L=1.6\times10^{31}cm^{-2}s^{-1}$ at the Z peak (the anticipated luminosity at LEP). We see that for m_H 60GeV we may anticipate several events in 3 months real running time (one year with efficiency 1/4).

We consider identification of the Higgs-boson via its decay $H\rightarrow q\bar{q}$ and we suppose that the 3-momenta $\vec{p}_q$, $\vec{p}_{\bar{q}}$ of the q, $\bar{q}$ and the energies E_q, $E_{\bar{q}}$ can be well determined. Let us introduce the invariant mass $m_{\nu\bar{\nu}}$ of the $\nu\bar{\nu}$ system. We can easily see that

$$m_{\nu\bar{\nu}}^2 = (M_Z-E_q-E_{\bar{q}})^2 - (\vec{p}_q + \vec{p}_{\bar{q}})^2$$

3.2.5

so $m_{\nu\bar{\nu}}$ is, indirectly, an experimentally measurable quantity.

In figure 3.3(a) we present the distribution $d\sigma/dm_{\nu\bar{\nu}}$ as a function of $m_{\nu\bar{\nu}}$ for various values of m_H. We note that $d\sigma/dm_{\nu\bar{\nu}}$ peaks near the upper end of phase space $m_{\nu\bar{\nu}}\approx M_Z-m_H$ (reference 37). The peaking can be qualitatively understood from an interplay between phase space and the propagator

$$\frac{1}{(p_4^2 - M_Z^2)^2 + \Gamma_Z^2 M_Z^2}$$

i.e. when $m_{\nu\bar{\nu}}^2$ $(=p_4^2)$ increases, this propagator increases since p_4^2 is closer to the resonance value of M_Z^2.

Instead of the variable $m_{\nu\nu}$ we may alternatively introduce the total energy of ν and $\bar{\nu}$:

$$E_{\nu\bar{\nu}} \equiv E_{\nu} + E_{\bar{\nu}} = M_Z - E_q - E_{\bar{q}} \qquad 3.2.6$$

$E_{\nu\bar{\nu}}$ is also experimentally measurable and, over $m_{\nu\nu}$ it has the advantage that it requires determination only of the magnitudes $|\bar{p}_q|$, $|\bar{p}_{\bar{q}}|$ of $\bar{p}_q$ and $\bar{p}_{\bar{q}}$ and not the directions.

In figure 3.3(b) we present the distribution of $d\sigma/\,dE_{\nu\nu}$ as a function of $E_{\nu\bar{\nu}}$ and of m_{H}. This distribution also peaks near the upper end of phase space $E_{\nu\nu} \approx M_Z - m_H$; in fact, the peaks are more pronounced than in $d\sigma/\,dm_{\nu\nu}$.

At this point it should be said that the channel $e^+e^- \to Hl^+l^-$ (references (36)-(39)) gives more handles on Higgs-boson searches; it has a more clear sign and better and more accurate reconstruction. On the other hand, first as figure 3.2 shows, it has a smaller cross section than (3.1.1). Second, if $l^{\pm}$ is a $\tau-$ lepton, there are problems with the $\tau-$ lepton, identification, and if $l^{\pm}$ is an electron, there is significant background from $e^+e^- \to e^+e^- q\bar{q}$ via a two photon process (see reference (38) eq. 3.11). Finally for all leptons, there is some background from

$e^+ e^- \rightarrow Z^0 \rightarrow l^+l^- q\bar{q}$

For example, for m_H=47GeV, and l=e, the total cross section for this process is comparable to that for $e^+e^- \rightarrow Z \rightarrow He^+e^-$ (reference 40).

Returning to our process $e^+e^- \rightarrow Z \rightarrow H\nu\bar{\nu}$, with $H \rightarrow q\bar{q}$, if we consider $\sim$10 events in three months real running time as a reasonable lower limit for the Higgs-boson identification, figure 3.2 implies that one can see a Higgs-boson with a mass as high as m_H=67GeV. However, this assumes that in all events $H \rightarrow q\bar{q}$, the two jets resulting from q, $\bar{q}$ are well identified, i.e., that jet-jet reconstruction into a peak corresponding to a resonance proceeds with very high efficiency. The difficulties of the UA1 and UA2 Collaborations at the CERN $p\bar{p}$ collider in attempting to establish resonances with jets do not justify such an assumption; and, although jets from e^+e^- collisions are known to be more clean, similar difficulties may still be anticipated at LEP. We therefore expect that in our case a Higgs-boson with a mass not exceeding $m_H \sim 60 GeV$ can be identified.

3.3 Background from $Z \rightarrow q\bar{q}\nu\bar{\nu}$

In this section we consider background contributions of the form

$$e^+e^- \rightarrow Z \rightarrow q\bar{q}\nu\bar{\nu}$$

3.3.1

where $m_q << M_Z$. We show that with $L = 1.6 \times 10^{31}\, cm^{-2} s^{-1}$ this background represents a few events; but that by taking advantage of the smallness of Γ_H (eq. 3.2.1) and introducing an appropriate acceptance cut we can practically eliminate it.

The Feynman graphs contributing to (3.3.1) are shown in figure 3.1(b). Reaction (3.3.1) (with q=u,d,s,c,b) involves well-established particles of the standard model, so that such contributions are definitely present.

In figure 3.2 we present the total cross section for (3.3.1) (denoted as "background") for all q=u,d,s,c,b which we have calculated using the Weyl spinor method described in section 1.4 and checked using the method of reference (25) described in section 1.4 This cross section corresponds to only a few events which is to be anticipated by the fact that the amplitudes of the graphs in figure 3.1(b) are of order g_W^4. However, if eventually the luminosity increases and one wishes to search for a Higgs-boson with a larger mass, one would have to deal with this background.

Now we compare the background (3.3.1) with $e^+e^- \rightarrow Z \rightarrow H\nu\bar{\nu}$. Figure 3.2 shows that if $m_H < 50 GeV$, this background is significantly lower; the Higgs-boson signal is well above this value. However, if

$m_H \simeq 60$-$70 GeV$ the cross section is comparable. To practically eliminate the background consider the invariant mass $M_{q\bar{q}}$ of $q\bar{q}$ in (3.3.1), which is the invariant mass of the two jet system. The distribution $d\sigma / dM_{q\bar{q}}$ with respect to $M_{q\bar{q}}$ for the background events (3.3.1) is shown in figure 3.4; as one may anticipate, it is a smooth distribution. Now we use the fact that the Higgs-boson is very narrow ($\Gamma_H \sim O(10^{-4} m_H)$): By introducing an acceptance cut in $M_{q\bar{q}}$ around m_H we can eliminate most of the events (3.3.1) without significantly affecting the cross section for $e^+e^- \rightarrow Z \rightarrow \nu\bar{\nu}$.

In actual practice the magnitude of this cut will be specified by the resolution in determining $M_{q\bar{q}}$ rather than by Γ_H itself. For example, for $m_H = 55 Gev$ even if we assumed a resolution as poor as $10 GeV$, a cut requiring that $50 \leq M_{q\bar{q}} \leq 60 GeV$ will eliminate 90% of the background events (3.3.1).

The production of $t\bar{t}$ could, in principle, cause a large background to the signature we are looking for. If the mass of the top-quark, m_t, exceeds $M_Z/2$, the corresponding background is rather small and is not a matter of concern more than the background of (3.3.1). However if $m_t<M_Z/2$, at the Z peak there will be copious $t\bar{t}$ production, and this may present a formidable problem for Higgs-boson detection.

The processes contributing to this background are

$$e^+e^- \longrightarrow Z \rightarrow \bar{t}t$$
$$\quad\hookrightarrow bq\bar{q}'$$
$$\quad\hookrightarrow \bar{b}\bar{\nu}_\tau\tau^-$$
$$\quad\hookrightarrow hadrons+\nu_\tau$$

3.4.1

$$e^+e^- \longrightarrow Z \rightarrow \bar{t}t$$
$$\quad\hookrightarrow b\nu_\tau\tau^+$$
$$\qquad\hookrightarrow hadrons+\bar{\nu}_\tau$$
$$\quad\hookrightarrow \bar{b}\bar{\nu}_\tau\tau^-$$
$$\qquad\hookrightarrow hadrons+\nu_\tau \quad ;$$

3.4.2

the corresponding graphs are shown in figure 3.1(c). In (3.4.1) the four jets in the final state (arising from b, $\bar{b}$, q, and $\bar{q}'$) may combine so that they effectively produce two jets (see below). The mode $\tau^- \to hadrons + \nu_\tau$ is a very important (~70%) fraction of τ decays. Now, if these individual hadrons are detected (or if there is good τ – lepton identification) the reactions (3.4.1) and (3.4.2) cause no problem. However, if only jets are identified, (3.4.1) and (3.4.2) produce a serious background. It is the latter case we consider here.

In combining the four final-state quarks of (3.4.1) to produce two jets we use the jet algorithm described in section 1.5. Here we use the jet algorithm parameters:

$$|\cos\theta_0^*| = 0.8 \qquad p_T^0(j) = 3GeV \qquad \Delta_0 = 30^o; \tag{3.4.3}$$

which is similar to experiments at LEP and SLC reference (42). We of course use slightly different values.

To estimate the missing momentum associated with the neutrino in $\to hadrons + \nu_\tau$ we use the following model for τ decay: All such decays are taken to be of one of the types $\tau \to (\pi, K, \rho, A_2) + \nu_\tau$; ρ is taken to represent decays into two hadrons and the A_2 meson represents decays into three hadrons. It turns out that the results are not very sensitive to the description of the hadron system. Finally, to get the total missing momentum $\not{p}$, we combine the missing momenta of the final τ – neutrinos and τ – antineutrinos.

In figure 3.5 we present the distribution of $d\sigma / d\not{p}_T$ as a function of the total missing transverse momentum $\not{p}_T$ for events of type (3.4.1) (denoted as 1–τ events), of type (3.4.2) (denoted by 2–τ), and of type

$Z \to H\nu\bar{\nu}$ with m_H=40GeV and 50GeV. These distributions are the result of a Monte Carlo calculation. The first two (1$-\tau$ and 2$-\tau$) correspond to a top-quark mass of m_t=42.5GeV (so that the corresponding t-quarkonium mass is M_t=85GeV, see sect. 3.5). Clearly events (3.4.1) and (3.4.2) form a formidable background. We notice that an acceptance cut at, for example, $p_t > p_t^0 = 15GeV$ eliminates a greater portion of events (4.1) and (4.2) than of $Z \to H\nu\bar{\nu}$. so we proceed by introducing a cut $p_T^0 = 15GeV$.

With the two jets resulting from (3.4.1) and (3.4.2) defined as above, we introduce the variable

$$E^* = M_Z - E_{J_1} - E_{J_2} \tag{3.4.4}$$

where E_{J_1}, and E_{J_2} are the energies of the two jets. Clearly, for $Z \to H\nu\nu$ with $H \to q\bar{q}$ this variable corresponds to $E_{\nu\nu}$ of Eq. (3.2.6) (E^* $E_{\nu\nu}$). Figure 3.6 shows the distributions for $d\sigma/dE^*$ vs E^* for 1$-\tau$ and 2$-\tau$ events (with m_t=42.5GeV) and for $Z \to H\nu\bar{\nu}$ events (with m_H= 30, 40 and 50GeV) all calculated using the Monte Carlo technique with an acceptance cut $p_t^0 = 15GeV$. For all such values of m_H the events $Z \to H\nu\nu$ should show as an excess over the 1$-\tau$ and 2$-\tau$ background.

Instead of E^* we may introduce the variable m* :

$$(m^*)^2 \equiv (E^*)^2 - (p_{J_1} + p_{J_2})^2 \tag{3.4.5}$$

where p_{J_1} and p_{J_2} are the momenta of the two jets, this variable corresponds to $m_{\nu\bar{\nu}}$ of Eq. (3.2.5). We have also calculated $d\sigma/dm^*$ vs.

m* for $1-\tau$, $2-\tau$, and $Z \rightarrow H\nu\bar{\nu}$ events, with similar results.

We have also obtained good results with the following variable:

$$\not{E} \equiv M_Z - E_{j_1} - E_{j_2} - E_{hadrons} \tag{3.4.6}$$

where $E_{hadrons}$ is the total energy carried by the individual hadrons from the $\tau^{\pm}$ decay of (3.4.1) and (3.4.2) (not the ones forming the jets j_1 and j_2). In $Z \rightarrow H\nu\bar{\nu}$ there are no such individual hadrons, so that $E_{hadrons}=0$ and $\not{E}$ coincides with the variable $E_{\nu 1}$ of eq. (3.2.6). In figure 7 we present the distributions $d\sigma/ d\not{E}$ versus $\not{E}$ for $1-\tau$ and $2-\tau$ events (m_t=42.5GeV) and for $Z \rightarrow H\nu\bar{\nu}$ events (m_H=30,40, and 50GeV) calculated with p_T^0=15GeV. Now the peaks of the $1-\tau$ and $2-\tau$ distributions are somewhat shifted towards smaller $\not{E}$.

Furthermore, to exploit the fact that the Higgs-boson is very narrow (section 3.3.2), in figures 3.8(a) and 3.8(b) we present the distributions $d\sigma/ dM_{j_1j_2}$ versus $M_{j_1j_2}$ ($M_{j_1j_2}$= the invariant mass of the two jets) for the sum of $1-\tau$ and $2-\tau$ events (m_t=42.5GeV) and for $Z \rightarrow H\nu\bar{\nu}$ events with (a) m_H=40GeV (figure 8(a), additional cut $40<E^*<50GeV$), and (b) m_H=50GeV (figure 8(b), additional cut $30<E^*<40GeV$); in all cases p_T^0=15GeV. It is clear that the events $Z \rightarrow H\nu\bar{\nu}$ well exceed the combined $1\tau+2\tau$ background.

We note that, in general the $1-\tau$ and $2-\tau$ background distributions show a peak (figures 3.6-3.8). This is due to purely kinematic reasons: As the energy variable (E^*, $\not{E}$, or $M_{j_1j_2}$) increases, the corresponding distribution decreases because of phase space effects; and as the variable decreases, the distribution again decreases because of the acceptance cuts.

Backgrounds similar to the ones discussed in this section will arise when one or both of the top-quarks decay semileptonically producing $l^{\pm}=\mu^{\pm}$ or $e^{\pm}$, and, for some reason $l^{\pm}$ is not detected. For example,

$$
\begin{array}{l}
e^{+}e^{-} \rightarrow Z \rightarrow t\bar{t} \\
\qquad\qquad\quad \bar{t} \rightarrow \bar{b}\mu^{-}\bar{\nu}_{\mu} \\
\qquad\qquad\quad t \rightarrow bq\bar{q}' \ or \ b\mu^{+}\nu_{\mu}
\end{array}
$$

3.4.7

with μ^{-} undetected. Likewise if τ^{+}, or τ^{-} in (3.4.1) and (3.4.2) decay semileptonically and the resulting lepton(s) are missed, additional background will be similar to the $1-\tau$ and $2-\tau$ events discussed above.

A rough estimate of such additional background can be made as follows: Let a_l be the probability of not detecting a lepton l ($=\mu$ or e). Also let b_e, b_μ, and b_h be the branching ratios for the decay of τ into $e^{-}\bar{\nu}_e\nu_\tau$, $\mu^{-}\bar{\nu}_\mu\nu_\tau$ and hadrons respectively ($b_e+b_\mu+b_h=1$) let $\sigma_{1\tau}$ be the cross section of the $1-\tau$ events of (3.4.1) (with b_h included), and σ_{1l} of the additional background with one $e^{\pm},\mu^{\pm}$ undetected. Then,

$$\sigma_{1l} = (a_e + a_\mu + b_e\, a_e + b_\mu\, a_\mu)\frac{\sigma_{1\tau}}{b_h}$$

3.4.8

Using the values b_e=0.165, b_μ=0.185, and b_h=0.65 (reference 10(b)) and taking as an example a_e=a_μ=0.1 we obtain

$$\sigma_{1l} = 0.35\sigma_{1\tau}$$

3.4.9

Likewise, let $\sigma_{2\tau}$ be the cross section of the $2-\tau$ events of (3.4.2) (with b_h^2 included), and σ_{2l} of the additional background with two leptons undetected. Then

$$\sigma_{2l} = (a_e + a_\mu + b_e a_e + b_\mu a_\mu)^2 \frac{\sigma_{2\tau}}{b_h^2} \tag{3.4.10}$$

and as in the previous example

$$\sigma_{2l} = 0.19\, \sigma_{2\tau} \tag{3.4.11}$$

We see that events with undetected leptons will enhance our background by only about 35%, therefore none of our conclusions will be affected.

3.5 t-Quarkonium Effects

If the t-quarkonium T ($=t\bar{t}$ bound state, $M_t = 2m_t$) is established at LEP or SLC, in general, the best way to detect the Higgs-boson is via $T \rightarrow H\gamma$. Reference (41), using a perturbative calculation obtains at tree level

$$r_{H\gamma} \equiv \frac{\Gamma(T \rightarrow H\gamma)}{\Gamma(T \rightarrow l^+ l^-)} = \frac{G_f}{\sqrt{2}\pi\alpha} m_t^2 (1 - \frac{m_H^2}{M_t^2})$$

3.5.1

According to (42), however, a higher order calculation may significantly reduce this rate. For example equation 2 of this reference gives the 1 loop correction to this process to be a 75% reduction given $m_H = 50GeV$ and $M_t = 80GeV$ (the result is not sensitive to the exact choice of these values). For the time being we will ignore these higher order effects, the total cross section for $e^+e^- \rightarrow T \rightarrow H\gamma$ is therefore

$$\sigma(T \rightarrow H\gamma) = \sigma(T \rightarrow hdrs.) \frac{\Gamma(T \rightarrow e^- e^+)}{\Gamma(T \rightarrow hdrs.)} r_{H\gamma}$$

3.5.2

To estimate this, for the partial width $\Gamma(T \rightarrow e^+ e^-)$ we accept the value of $5KeV$ (reference (39)). The total width $\Gamma(T \rightarrow hadrons)$ is model dependent due to uncertainty in the quark wave function. For the Richardson potential (43), which is supposed to incorporate asymptotic freedom effects, one finds $\Gamma(T \rightarrow hadrons) = 100KeV$. To get an idea of the uncertainty we mention that another potentials give $127KeV$ (reference (44)).

In figure 3.2 we present $\sigma(e^+e^-\to T\to H\gamma)$ as a function of m_H for $M_T=60$, 80, and $85GeV$ (dashed curves). Comparing with the cross section of $Z\to H\nu\bar{\nu}$ we conclude the following: (i) If $M_T=80-85GeV$, $\sigma(T\to H\gamma)\gg\sigma(Z\to H\nu\bar{\nu})$ except for $m_H\leq 20GeV$; (ii) If $M_T=60GeV$, for $m_H<30GeV$, $\sigma(T\to H\gamma)>\sigma(Z\to H\nu\bar{\nu})$. Of course, for $M_T<60GeV$ $T\to H\gamma$ is impossible. Thus for $M_T\sim 60$-70 or $\leq 30GeV$, $Z\to H\nu\bar{\nu}$ is quite useful.

It is, perhaps, of interest to consider also

$$e^+e^-\to T\to H\nu\bar{\nu} \tag{3.5.3}$$

This proceeds via the graphs of figures 3.1(d); in the third graph the Z is off shell. To determine the cross section we follow the perturbative approach of reference (41). Straightforward but lengthy calculation gives the following ratio of widths

$$\frac{\Gamma(T\to H\nu\bar{\nu})}{\Gamma(T\to H\gamma)}=\frac{3A'^2_Z A^{\nu 2}_Z N_\nu}{(2\pi)^3\alpha(1-m_H^2/m_T^2)}\int dE_H\,|p_H|\,\frac{p^2}{(p^2-M_Z^2)^2+\Gamma_Z^2M_Z^2}$$

$$\left[\frac{(p\cdot q)+2m_tp^2}{(k^2-m_t^2)^2}+\frac{6M_Z^4}{(q^2-M_Z^2)^2+\Gamma_Z^2M_Z^2}\times\left(1+\frac{(p\cdot q)(q^2-M_Z^2)}{M_Z^2(k^2-m_t^2)}-\frac{1}{3}\left(1+\frac{B'^2_Z}{A'^2_Z}\right)\left(1-\frac{(p\cdot q)^2}{4m_t^2p^2}\right)\right)\right]\ . \tag{3.5.4}$$

The momenta p_H, p, k, and q are defined in figures 3.1(d). A_f and B_f are given by 3.2.3. $N_\nu=3$ is the number of massless neutrinos. Finally the range of integration of E_H is

$$m_H\leq E_H\leq\frac{M_T^2+m_H^2}{2M_T} \tag{3.5.5}$$

Then on the basis of (3.5.1) and (3.5.2) we can determine the cross section $\sigma(T\to H\nu\bar{\nu})$.

Using for $\Gamma(T\to e^+e^-)$ and $\Gamma(T\to hadrons)$ the same values as before we present in figures 3.2 the cross section of $T\to H\nu\bar{\nu}$ as a function of m_H for M_T=85 and 92GeV (dash-doted curves). We see that for M_T=85, $\sigma(T\to H\nu\bar{\nu})$ is very small but that for M_T=92 and $m_H\geq 50GeV$ it is comparable to $\sigma(Z\to He^+e^-)$. The smallness of $\sigma(T\to H\nu\bar{\nu})$ for $M_T\leq 85GeV$ can be understood by the fact that with respect to $T\to H\gamma$ the amplitudes of graphs of figures 3.1(d) are of $O(g_W)$.

However, for a $t\bar{t}$ bound state of spin 1, when its mass is close to the mass of Z, namely,

$$|M_Z - M_T| \leq O(\Gamma_Z)$$

3.5.6 there are important T-Z mass mixing and interference effects (references (44)-(46)). Since our results in figure 3.2 neglect T-Z mixing they, may only serve as a rough estimate of the contribution (3.5.4) if (3.5.6) is true.

3.6 Conclusions

We have considered Higgs-boson production via $e^+e^- \to Z \to H\nu\bar{\nu}$ with subsequent decay $H \to q\bar{q}$. We may conclude the following.

(i) If the top-quark has a mass $m_t > M_Z/2$, or if $m_t \leq M_Z/2$ but there is good τ - lepton identification, the above reaction allows detection of a Higgs-boson with mass up to $m_t = 60GeV$. The background $e^+e^- \to Z \to q\bar{q}\nu\bar{\nu}$ can be practically eliminated via an acceptance cut in the invariant mass $M_{\nu\nu}$.

(ii) If $m_t < M_Z/2$, in particular if $m_t = 40-45GeV$, and if there is no τ lepton identification, the reactions (3.4.1) and (3.4.2) produce a formidable background. Still, by introducing various acceptance cuts, it is possible to detect a Higgs-boson with $m_H < 50GeV$.

If the t-quarkonium T is established, in general detection of the Higgs-boson via $e^+e^- \to T \to H\gamma$ is a better way. If $M_T \approx 80-85GeV$ and $m_H < 20GeV$, both $T \to H\gamma$ and $Z \to H\nu\bar{\nu}$ can be used (the latter has a cross section comparable or even greater than the former). The same is true if $M_T \approx 60GeV$ and $m_H \leq 30GeV$.

In the case $M_T = 60GeV$ and $m_H \geq 60GeV$, $T \to H\gamma$ cannot be used; then $Z \to H\nu\nu$ allows detection of a Higgs-boson with $m_H \approx 60GeV$ if there is good τ - lepton identification.

Figure Captions

Figure 3.1.

(a) Lowest order graphs for $e^+e^- \to H f \bar{f}$. (b) Graphs contributing to the background $e^+e^- \to Z \to q\bar{q}\nu\bar{\nu}$. (c) Graphs for the background $e^+e^- \to t\bar{t} \to 2\ jets + p_T$. (d) Graphs for the perturbative calculation of $T \to H\gamma$.

Figure 3.2.

Total cross sections as functions of the Higgs-boson mass m_H. Solid line: $e^+e^- \to Z \to H\nu\bar{\nu}$. Dash-double-dotted lines: $Z \to Hqq, Hl^+l$, and He^+e^-. Dashed lines: $T \to H\gamma$ for M_t=60, 80, and 85GeV. Dash-dotted lines: $T \to H\nu\bar{\nu}$ for M_T=85GeV and $M_l = M_t$. The solid line denoted background is the total cross section for $e^+e^- \to Z \to qq\nu\bar{\nu}$. The dashed line corresponds to 1 event in four months (1 year with efficiency of 1/4) real running time with $L = 1.6 \times 10^{31} cm^{-2} s^{-1}$.

Figure 3.3.

Distributions for $e^+e^- \to Z \to H\nu\bar{\nu}$: (a) vs the invariant mass $m_{\nu\nu}$ (eq. 3.2.5); (b) vs the energy $E_{\nu\nu}$ (eq. 3.2.6).

Figure 3.4.

Distribution $d\sigma / dM_{J1J2}$ of the background $e^+e^- \to Z \to q\bar{q}\nu\bar{\nu}$ vs the invariant mass $M_{J1J2} = M_{q\bar{q}}$.

Figure 3.5.

Distributions $d\sigma / dp_t$ vs missing transverse momentum p_t

calculated via the Monte Carlo method. Solid lines: for $Z \to H\nu\bar{\nu}$ corresponding to m_H=40 and 50GeV. Dashed lines:for the background Eq. (3.4.2) (denoted 2$-\tau$), with m_t=42.5GeV.

Figure 3.6.

Distributions $d\sigma/dE^*$ vs the variable E^* of eq. 3.4.4: Solid lines: for $Z \to H\nu\bar{\nu}$ with m_H=30,40, and 50GeV. Dashed lines: for eq. (3.4.1) (1$-\tau$) and for eq. 3.4.2 (2$-\tau$) with m_t=42.5GeV. In all cases an acceptance cut p_t^0=15GeV is used.

Figure 3.7.

Distributions $d\sigma/dE$ vs the variable E of eq. (3.4.6). Solid and dashed lines as in figure 3.6.

Figure 3.8.

Distributions $d\sigma/dM_{J/J2}$ vs $M_{J/J2}$ with p_T^0=15GeV. Dashed lines: total contribution of eqs. (3.4.1) and (3.4.2) ($1\tau+2\tau$) with m_t=42.5GeV. (a) With additional acceptance cut 40<E^*<50GeV. Solid distributions for m_H=40GeV. (b) With 30<E^*<40GeV. Solid distribution for m_H=50GeV.

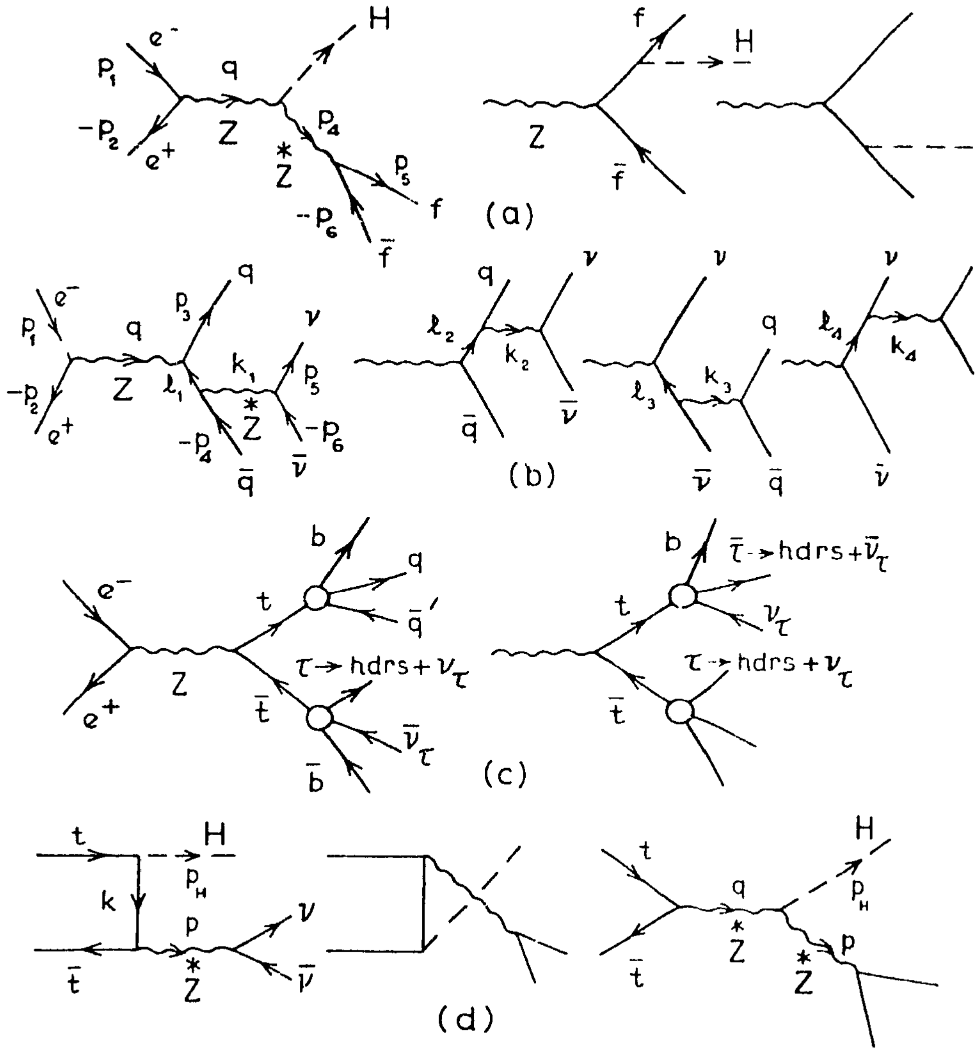

Figure 3.1

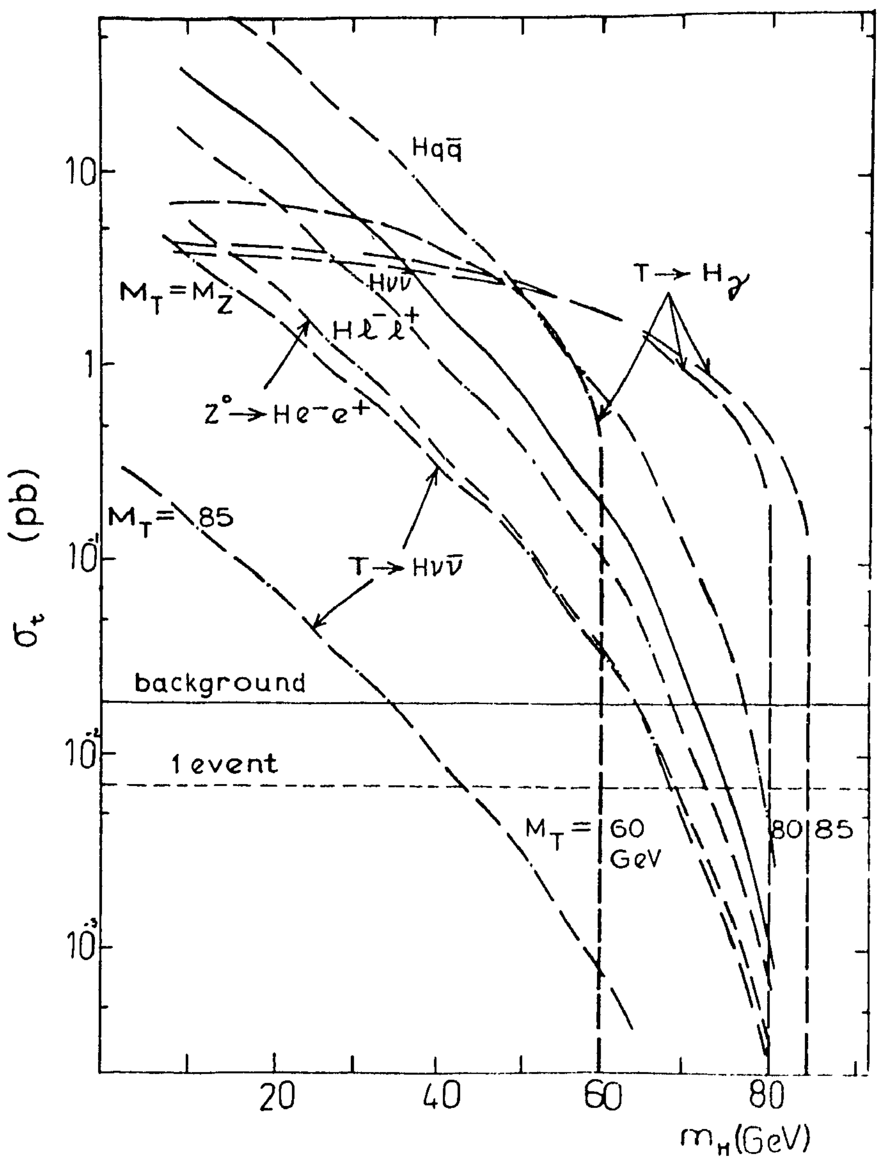
Hqq̄
Hνν̄
Hℓ⁻ℓ⁺
T→ Hγ
M_T = M_Z
Z° → He⁻e⁺
M_T = 85
T → Hνν̄
background
1 event
M_T = 60 GeV
80
85
10
1
10⁻¹
10⁻²
10⁻³
σ_t (pb)
20
40
60
80
m_H (GeV)

Figure 3.2

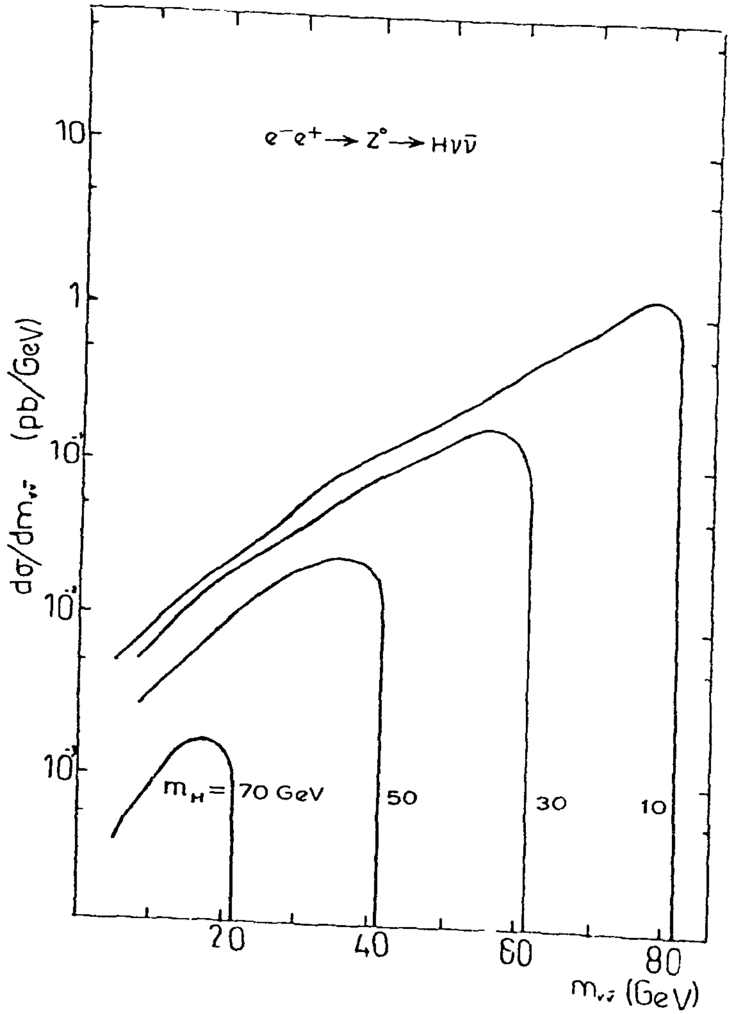

Figure 3.3a

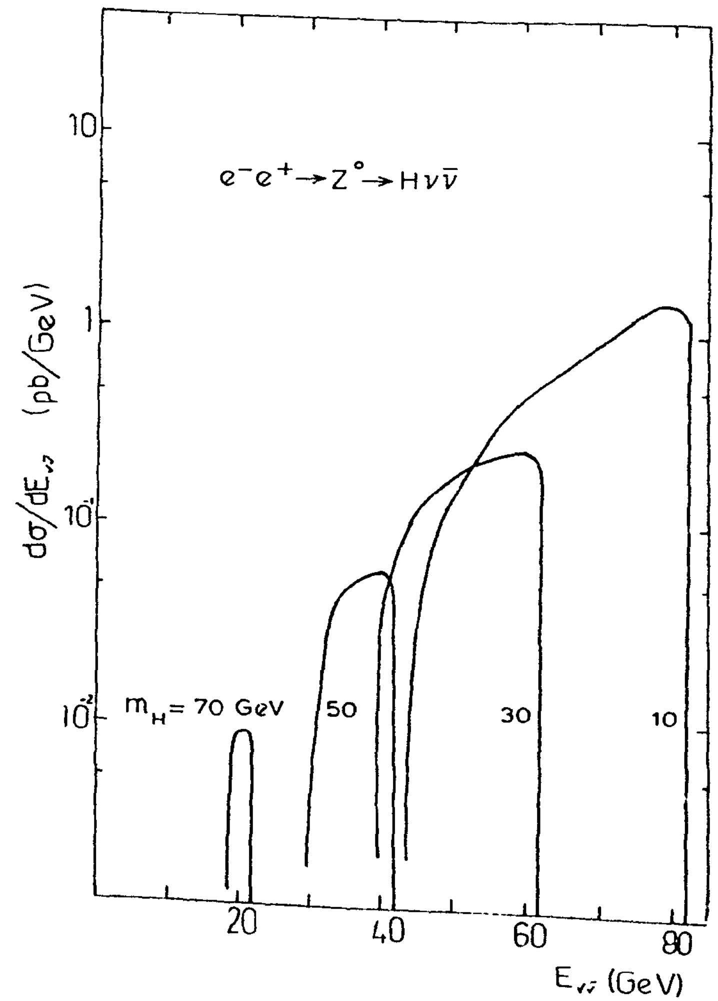

Figure 3.3b

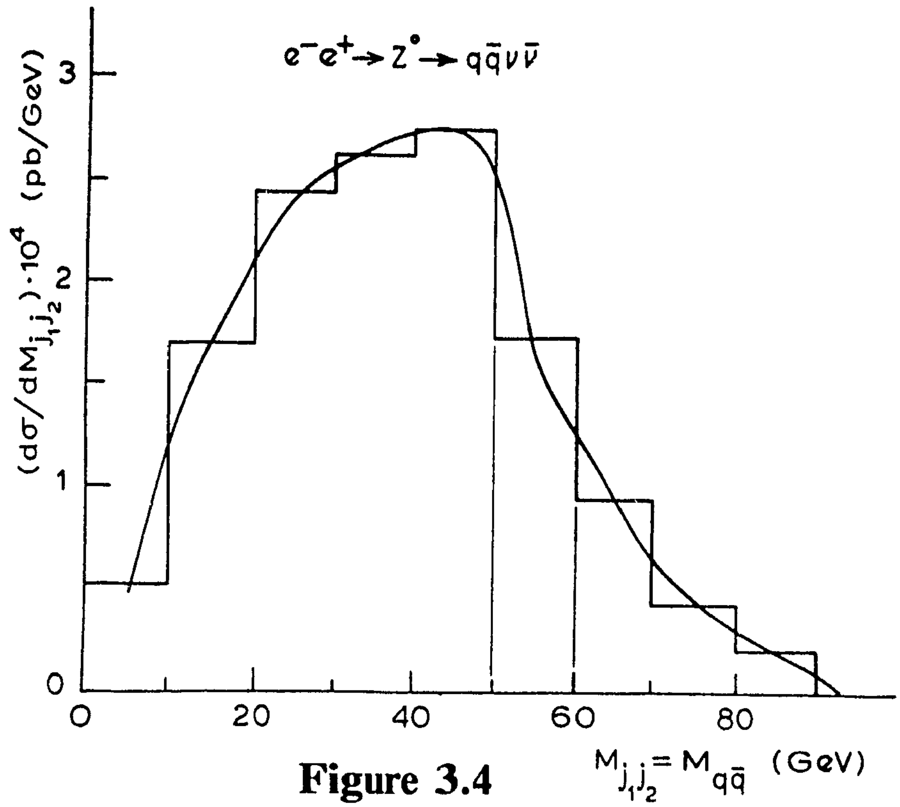

Figure 3.4

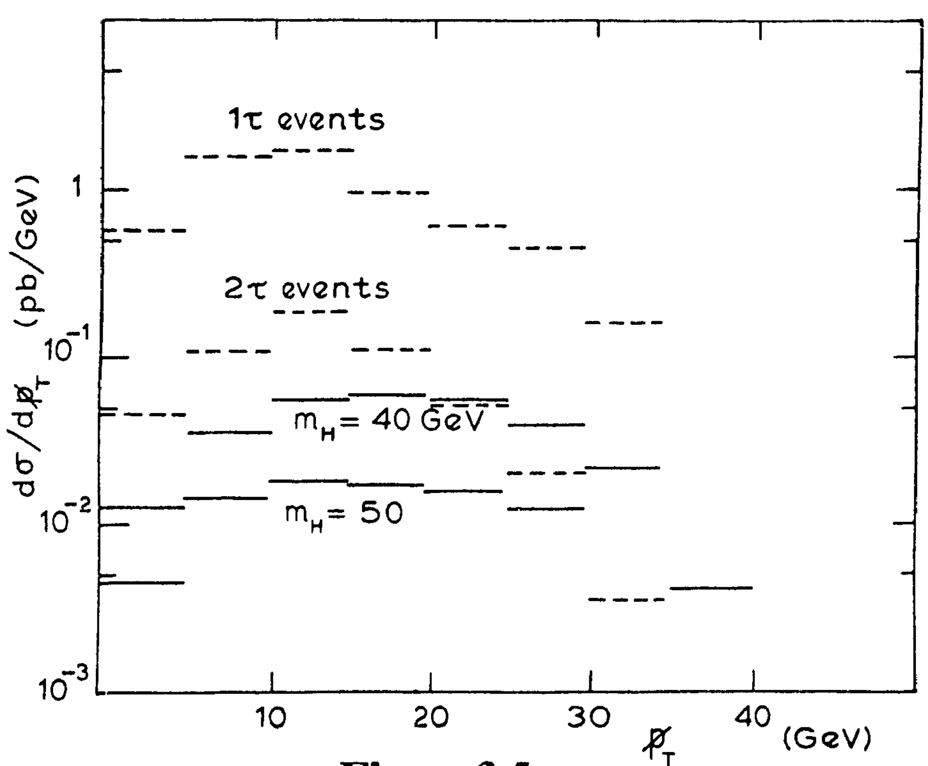

Figure 3.5

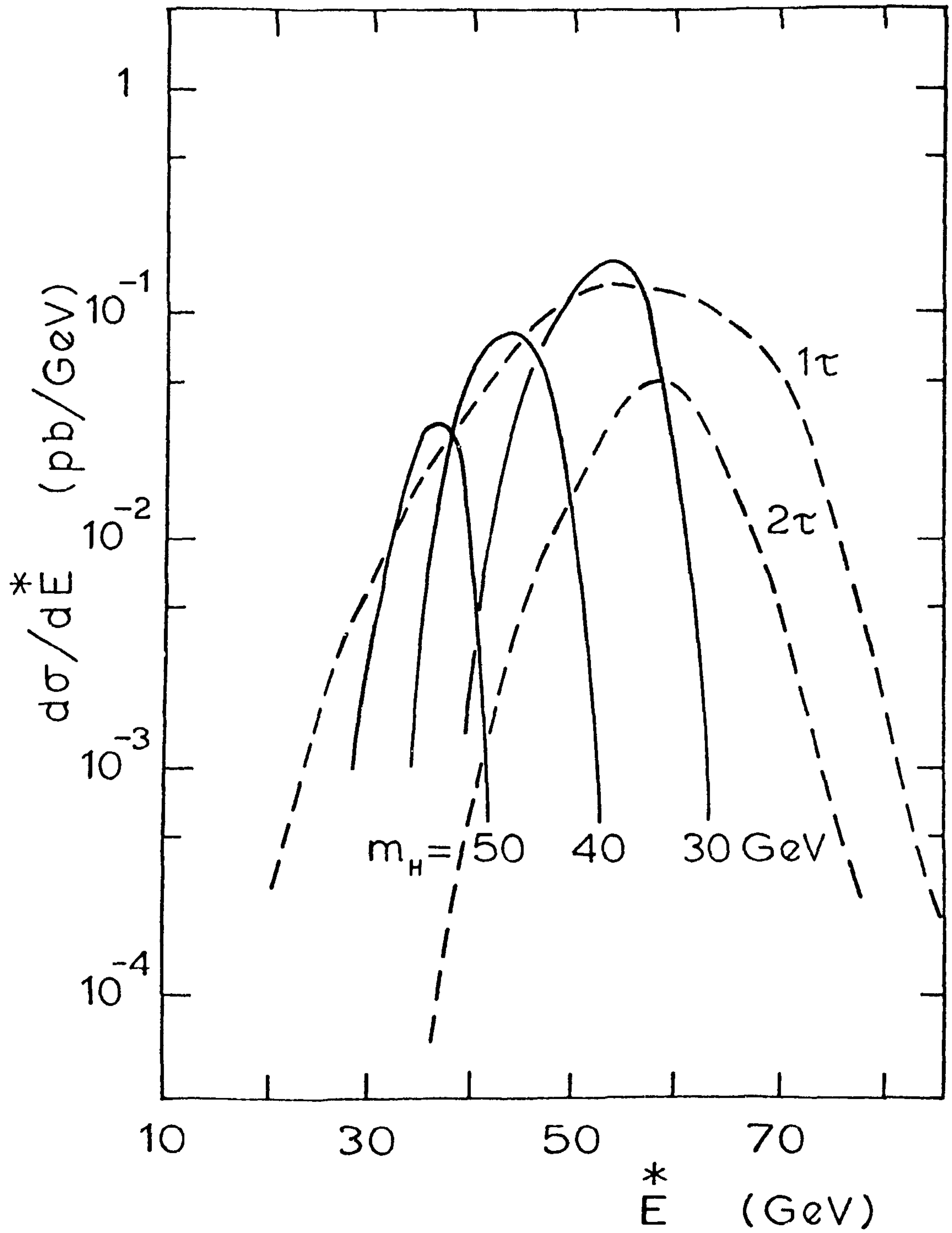

1
10^{-1}
10^{-2}
10^{-3}
10^{-4}
$d\sigma/dE^*$ (pb/GeV)
1τ
2τ
$m_H = 50$ 40 30 GeV
10
30
50
70
E^* (GeV)

Figure 3.6

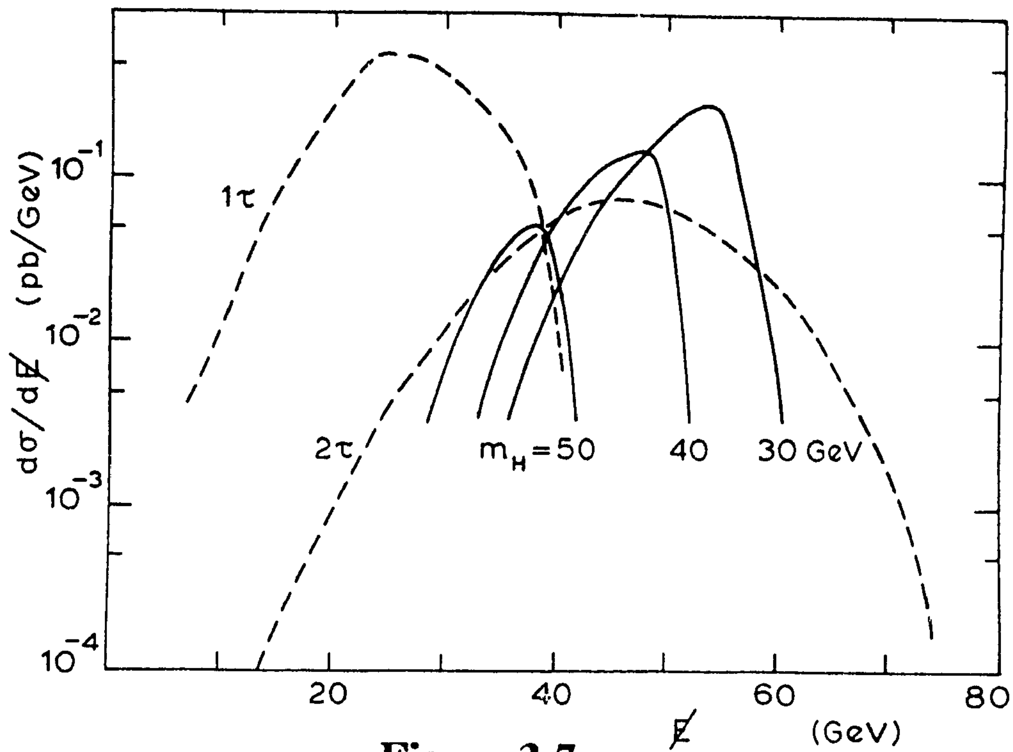

Figure 3.7

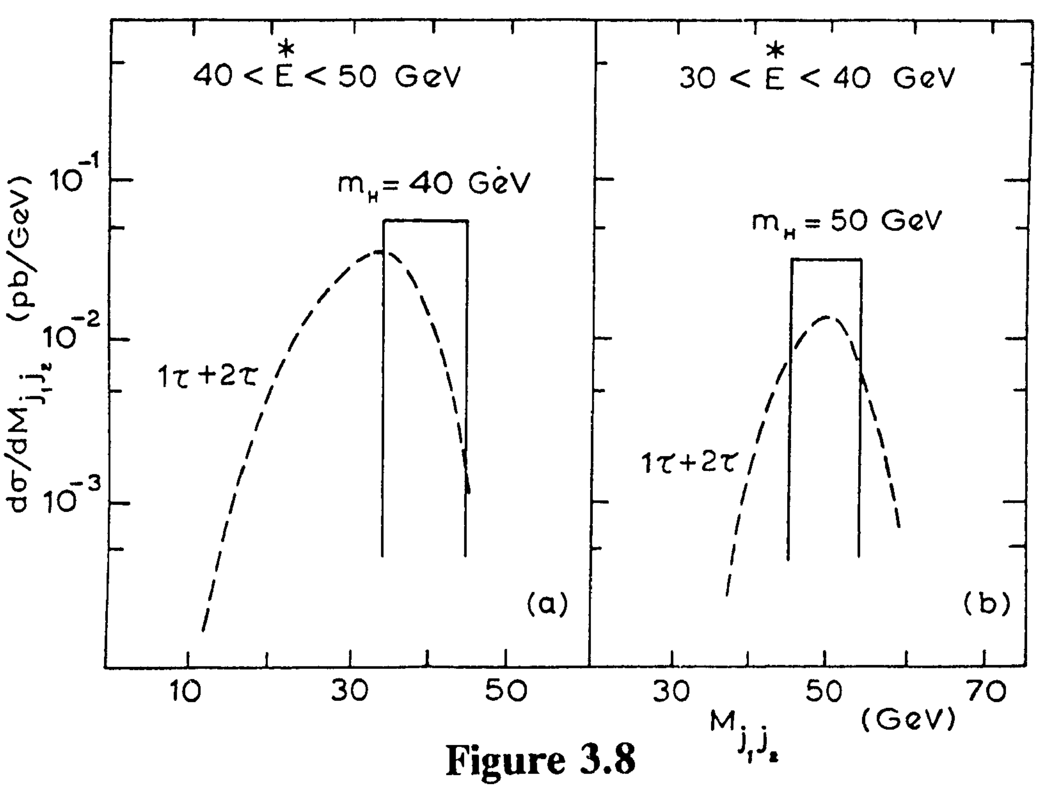

Figure 3.8

CHAPTER 4

PRODUCTION OF THE INTERMEDIATE MASS HIGGS-BOSON IN FUTURE ELECTRON-POSITRON COLLIDERS

4.1 Introduction

A range for which it is particularly hard to discover the Higgs-boson is the intermediate mass (IM) range discussed in chapter 1, $100GeV<m_H<2M_W$, where M_W is the W-boson mass. In this range, a very important role is played by the value of the mass m_t of the top-quark (which is as yet unknown). If $m_H<2m_t$ so that the decay $H\rightarrow t\bar{t}$ is impossible, an intermediate mass Higgs-boson (IMH) can still be detected for example at the SSC via $H\rightarrow b\bar{b}$ (47) as well as via its rare decays $H\rightarrow\gamma\gamma$, $\tau^+\tau^-$, or ZZ^* (see for example reference (48) and Chapter 5). However, if $m_H>2m_t$ such decays are strongly suppressed, and the possibilities of detection at SSC or LHC greatly diminish (e.g. the possibility of detection via $H\rightarrow\tau^+\tau^-$ practically disappears see chapter 5). It is precisely the case $m_H>2m_t$ which will be discussed in this chapter. In fact, throughout this chapter we suppose that the top quark with $m_t<m_H/2$ has been discovered, and its mass is fairly well determined.

In the IMH case, the best tool for detecting the Higgs-boson is possibly a electron-positron collider of cm energy $\sqrt{s}\geq300GeV$. Thus we study IMH production via the process

$$e^+ e^- \to H + Z \tag{4.1.1}$$

IMH production in electron-positron colliders at $\sqrt{s}$=1-2TeV has already been studied to some extent (49). At such energies the dominant channel for Higgs-boson production is through W^+W^- and ZZ fusion (49); the corresponding cross sections are larger than those via (4.1.1). However, the construction of electron-positron colliders in the TeV range presents yet unresolved technical problems; in fact, the difficulty increases with the energy. On the other hand, in the range $300 \leq \sqrt{s} \leq 500 GeV$ the process (4.1.1) dominates.

In this chapter we investigate in detail the latter range of energies. However, we also present results at higher $\sqrt{s}$; for even if Higgs-boson production via W^+W^- and ZZ fusion is advantageous the mechanism (4.1.1) offers an additional way.

In sect. 4.2 we present the basic formalism; we note that we carefully take into account the effect of photon bremsstrahlung from the initial state of e^+ or e^-. Section 4.3 discusses branching ratios and acceptance cuts and presents our basic results. In section 4.4 we discuss the possible background from $e^+e^- \to Zt\bar{t}$. Section 4.5 discusses a more important background from $e^+e^- \to t\bar{t}$ and presents results in detail. Finally Section 4.6 contains our conclusions.

With reference to figure 4.1(a) the cross section for $e^+e^-\to H+Z$ is (reference (50))

$$\sigma(s) = \pi\alpha_W^2 \frac{1+(1-4\sin^2\theta_W)^2}{8\cos^4\theta_W} \cdot \frac{M_Z^2}{(s-M_Z^2)^2} \frac{|\vec{q}|}{\sqrt{s}} (1+\frac{|\vec{q}|^2}{3M_Z^2})$$

4.2.1

where $\alpha_w=\alpha/\sin^2\theta_w$ and M_Z and $|\vec{q}|$ the mass and c.m. momentum of the Z; the c.m. differential cross section is:

$$\frac{d\sigma}{d\cos\theta} = \frac{3}{4}\sigma(s)\frac{2M_Z^2 + |\vec{q}|^2 (1 - \cos^2\theta)}{3M_Z^2 + |\vec{q}|^2} \quad .$$

4.2.2

Figure 4.2(a) shows the cross section (4.2.1) as a function of $\sqrt{s}$ for a Higgs-boson mass m_H=150GeV, and figure 4.2(b) shows (4.2.1) as a function of m_H at $\sqrt{s}$=500GeV (solid line). The results are in agreement with references (50) and (51) in kinematic regions of overlap.

It is important to consider also the effect of photon bremsstrahlung of the initial state e^+ or e^- (figure 4.1(b)). Events of interest for our purpose arise not only from figure 4.1(a), but also, in general, from figure 4.1(b). Then denoting by $\sigma_t(s)$ the total cross section for our process without and with photon emission, an appropriate expression from reference (52) is:

$$\sigma_t(s) = \lambda \int_0^{k_{max}} \frac{dk}{k}\, \sigma(s-2k\sqrt{s})\cdot[2\frac{k}{\sqrt{s}}(\frac{k}{\sqrt{s}} - 1) + (1 + \frac{3}{4}\lambda)(\frac{2k}{\sqrt{s}})^{\lambda}]$$

4.2.3

where $\sigma(s)$ is given by (4.2.1), $k_{max}=(s-(M_Z+m_H)^2)/2\sqrt{s}$ and

$$\lambda = 2\frac{\alpha}{\pi}(\ln\frac{s}{m_e^2} - 1)$$

4.2.4

with m_e= electron mass; the integration is over photon momentum k. The expression (4.2.3) includes also hard photon bremsstrahlung, in which case most of the contribution arises when the photons are emitted collinearly with the $e^{\pm}$ beam. It can be easily seen that, up to order α, the expression (4.2.3) reduced to expression 2.2.9 which we used in section 2.2. For our purposes we find that these two expressions give very similar results.

Denoting by $M_{H\gamma}$ the invariant mass of the system that recoils against the final Z and E_Z the c.m. energy of Z we have:

$$E_Z = \frac{s + M_Z^2 - M_{H\gamma}^2}{2\sqrt{s}}$$

4.2.5

Figure 4.3 (solid line) presents the distribution $d\sigma_t/dE_Z$ vs E_Z for $\sqrt{s}$=500GeV and M_H=150GeV ; this is equivalent to the distribution $d\sigma/dM_{H\gamma}$ vs $M_{H\gamma}$. Clearly there is a peak at $E_Z \approx 230 GeV$, corresponding to $M_{H\gamma}=m_H$. Thus a clear signature for the Higgs-boson will be a distribution in E_Z as in figure 4.3 with a prominent peak.

4.3 Branching Ratios, Acceptance Cuts and Results

We consider values of the top-quark mass $m_t \geq M_Z/2$; such values are favoured by recent analyses of the UA1 collaboration (53) and from Argus data regarding $B^0-\overline{B}^0$ mixing (54). We present results taking into account the following decay modes: For the Z decay we consider $Z \to l^+l^-$ as well as $Z \to q\overline{q}$; and regarding $H \to t\bar{t}$ we consider both t, $\bar{t}$ decaying hadronically as well as one of t, $\bar{t}$ decaying semileptonically and the other hadronically. We take the Z and t branching ratios (BR) given by the standard model. In the semileptonic decays $t \to bl^+\nu_l$ we also include $l = \tau$ – lepton.

In introducing acceptance cuts, when we consider hadronic decays of Z we must establish some condition facilitating the observation of jets from the Z. We denote by i, j the produced quarks (jets), and by θ_{ij} the angle between the quarks i, j; we denote by θ_i the angle the quark i makes with the beam axis. We label by i=1,2 the quarks from the Z. Consider first the case that in $H \to t\bar{t}$ one of t, $\bar{t}$ decays semileptonically. Then we label by j=3,4,5, and 6 the quarks arising from the t, $\bar{t}$ system. Now we introduce the following acceptance cuts

$$\cos\theta_{ij} < \cos\theta_{ij}^0 = 0.9 \quad i=1,2 \quad j=1-6$$

$$|\cos\theta_i| < \cos\theta_i^0 = \quad i=1,2$$

$$p_{T_i} \geq p_{T_i}^{\ 0} = 3GeV \quad i=1,2$$

4.3.1

In the case both $t,\bar{t}$ decay hadronically, our procedure is the same except that the quarks arising from the $t\bar{t}$ system are labelled by j=3,...,8. If the Z decays leptonically, the cuts (4.3.1) are not required.

Furthermore, we should ensure that the $t\bar{t}$ pair is indeed a $t\bar{t}$ pair and not some other $q\bar{q}$ pair. Considering first the decay $t \to bl^{+}\nu_l$, we denote by θ_{il} the angle between the lepton and the quark i. Thus for the quarks 3-6 we require: Either that (a) they form 3 or 4 jets according to our jet algorithm, or (b) they form 2 jets and the lepton is separated from them by an angle $\theta_{il} > \theta_l^0 = 10^o$.

In the case both t, $\bar{t}$ decay hadronically, we require that the quarks j=3-8 form at least 3 jets. In the above we use the jet algorithm of chapter 1 with parameters $|\cos\theta_0^*| = 0.9$, $|\cos\Delta_0| = 0.9$ and $p_T^0(j) = 3GeV$.

With the above cuts figure 4.2(a) shows the resulting cross section as a function of $\sqrt{s}$ for $m_{tt} = 150GeV$ and $m_t = 65GeV$ (short dashed line). For $\sqrt{s} < 1.2TeV$ this is not much lower than $\sigma(s)$ without cuts; however at the highest $\sqrt{s}$ it becomes smaller by more than an order of magnitude. This is primarily due to the above cut (a) or (b): As $\sqrt{s}$ increases the quarks originating from the Higgs-boson tend more and more to be collimated into a single jet, and this makes more difficult the formation of 2,3, or more jets required by the cut (a) or (b).

Figure 4.2(b) shows the same cross section as a function of m_{tt} at $\sqrt{s} = 500GeV$ and for $m_t = 65$ and $50GeV$ (short dashed lines); the cuts decrease the signal by a factor of about 3.

Figures 4.4(a) and (b) show the same cross section as a function of m_H for $\sqrt{s}$=300GeV and 1TeV.

It is important to show also the distribution $d\sigma_t / dE_Z$ (or $d\sigma_t / dM_{llv}$) including the acceptance cuts. Here in enforcing the cuts care is needed, and some details of our procedure are given in Appendix 4.A. Figure 4.3 shows this distribution for $\sqrt{s}$=500, m_H=150 and m_t=65GeV (short dashed line).

4.4 Background from

$e^+e^- \to Zt\bar{t}$

One source of background arises from the processes

$$e^+e^- \to Z\,\gamma^*$$
$$\qquad \to t\bar{t}$$

and

$$e^+e^- \to Z\,Z^*$$
$$\qquad \to t\bar{t} \qquad 4.4.1$$

depicted in figures 4.1(c),(c′). With respect to the main process (4.1.1) (the signal) the above processes are of order α and, off hand, one might tend to neglect them. However the main process (figure 4 1(a)) involves an s-channel exchange, so its cross section decreases rather fast with s; in contrast the backgrounds (4.4.1) involve a t-channel exchange and, *a priori*, their integrated cross sections might be relatively sizable especially in view of the initial state photon bremsstrahlung and the acceptance cuts we consider. Since these backgrounds may also be of interest in searches for other objects, we have carried an analytic calculation; details and results are given in Appendix 4.B.

Assuming for the $t\bar{t}$ system a resolution $\Delta M_{tt}=20GeV$ (a value rather generous (55)), figure 4.2(a) shows the resulting background (long dashed line). Notice that this background cross section involves no acceptance cuts or branching ratios. Thus it should be compared with the main process cross section shown with solid line. We conclude that this background is small.

We have also considered the effect of photon bremsstrahlung on the background (4.4.1); the corresponding distribution $d\sigma/dE_Z$ is again small compared to the main process. Introduction of acceptance cuts and branching ratios further reduced the background.

Figure 4.2(a) also shows the level of one event/year assuming a luminosity $L=10^{33}cm^{-2}s^{-1}$ and efficiency 1/3.

In the special case $m_H \sim M_Z$ and if $m_t < M_Z/2$ so that $Z \to t\bar{t}$ is possible, a troublesome background may arise from $e^+e^- \to ZZ$. We have not investigated this case.

4.5 Background from $e^+e^- \to t\bar{t}$

A potentially more important background arises from events of the type:

$$e^+e^- \to \gamma^* \to t\bar{t}$$

$$e^+e^- \to Z^* \to t\bar{t}$$

4.5.1

depicted in figure 4.1(d). The point is that various decay products of $t, \bar{t}$ may appear to "fake" the final Z of the main process (4.1.1) (the signal). Suppose for example that both $t, \bar{t}$ decay hadronically; then one of the quarks from each of the $t, \bar{t}$ may combine to produce a system of invariant mass about M_Z (figure 4.1(d)). The same situation may arise if one of $t, \bar{t}$ decays semileptonically and the other hadronically.

Denote by m_{ij} the invariant mass of the two quarks i and j. We accept an event from this background as producing a fake Z if there are two quarks i,j such that

$$|m_{ij} - M_Z| \le \delta m_Z^{(0)}$$

4.5.2

and we take $\delta m_Z^{(0)}=10GeV$. Furthermore, denote by $\tilde{m}_H$ the invariant mass of the system that recoils against the two quarks i and j (i.e. of the decay products of $t, \bar{t}$ other than i and j). Then for each value of the Higgs-boson mass m_H we take the event to be a background to Higgs-boson detection if, in addition to (4.5.2),

$$|\tilde{m}_H - m_H| \leq \delta m_H^{(0)} \qquad 4.5.3$$

we also take $\delta m_H^{(0)}=10GeV$.

The resulting background cross section for m_t=65GeV is shown first for $\sqrt{s}$=0.5TeV in figure 4.2(b) (short dash dotted line). Notice that no acceptance cuts (other than (4.5.2) and (4.5.3)) are imposed on this cross section; thus it should be compared with the main process without cuts (solid line in figure 4.2(b)). The same background cross section is also shown for $\sqrt{s}$=0.3 and 1TeV (Figures 4.4(a) and (b)).

The important point is that in all cases, although this background has a large cross section, its phase space properties are very different from those of the signal. Referring for example to figure 4.2(b) we see that it is quite strong (it peaks) at $\tilde{m}_H \sim 0.4TeV$; however, in the range $0.1 \leq \tilde{m}_H \leq 0.17TeV$, where the signal is important, this background is far below.

We can understand qualitatively the shape of this background as follows. To be specific, consider figure 2(b), i.e., $\sqrt{s}$=0.5TeV. Referring to figure 1(d), assume for simplicity that the quark i (j) is produced collinearly from t ($\bar{t}$) ; in view of m_t=65GeV and of the fact that each of t, $\bar{t}$ is produced with energy $\sqrt{s}$=250GeV, this assumption is reasonable. Now, since the quarks i and j fake the Z we have that their invariant mass m_{ij}:

$$m_{ij} \approx M_Z \ , \qquad 4.5.4$$

where the top-quark mass has been neglected. Then, the remaining jets will have an invariant mass of roughly

$$\sqrt{s}-M_Z \approx 0.4TeV \quad . \tag{4.5.5}$$

Then, the peak at $m_H \sim 0.4TeV$ is understood. Sometimes the invariant mass will be less than $\sqrt{s}-M_Z$, which gives rise to the long tail at $m_H < 0.4TeV$.

We also consider the effect of a photon bremsstrahlung on the background (4.5.1). Figure 4.3 shows the corresponding distribution $d\sigma / dE_Z$ (short dash-dotted line) for $\sqrt{s}$=500, m_H=150 and m_t=65GeV. Clearly this E_Z distribution peaks at low E_Z, so that the peak due to the signal (4.1.1) remains very prominent.

Finally, we have calculated the cross section of this background when the BR and acceptance cuts of section 4.3 are imposed (together with (4.5.2) and (4.5.3)). For m_t=65GeV the results at $\sqrt{s}$=0.3, 0.5 and 1TeV are shown with a short dash-dotted line in Figures 4.4(a), 4.2(b) and 4.4(b). Of course, in all cases BR and acceptance cuts significantly reduce the background cross section. Of particular interest is their effect at $\sqrt{s}$=0.3TeV (figure 4.4(a)), where it is clear that with the same BR and acceptance cuts the signal (short dashed line) well exceeds the background.

4.6 Conclusions

In conclusion, an intermediate mass Higgs-boson, with its mass exceeding $2m_t$ so that it mainly decays to $t\bar{t}$, could well be observed in an electron-positron collider of $\sqrt{s}$=300–500GeV and luminosity L=$10^{33}cm^{-2}s^{-1}$. Figure 4.2(a) shows that for m_H=150 and m_t=65GeV one could anticipate about 100 events/year (at an efficiency of 1/3). Construction of such a collider may become feasible in the future; certainly it presents less formidable problems than that of an electron-positron collider at $\sqrt{s}$=1TeV.

Appendix 4.A

As we stated near the end of Sect. 4.4, in calculating distributions like $d\sigma / dE_Z$, care is needed in enforcing the acceptance cuts. To explain our procedure, let $\tilde{\sigma}(s)$ be such a distribution involving no acceptance cuts. First we write $\tilde{\sigma}(s)$ in terms of the matrix element squared $|M|^2$:

$$\tilde{\sigma}(s) = \int |M|^2 \, d\Phi(s) \tag{4.A.1}$$

where $d\Phi(s)$ is the element of phase space. To introduce cuts, let $\chi(s)$ be a function of phase space such that $\chi(s)=1$ if the cuts are satisfied and $\chi(s)=0$ otherwise. then the distribution with cuts is

$$\sigma(s,cuts) = \int \chi(\Phi) \, |M|^2 \, d\Phi(s) \tag{4.A.2}$$

In calculating the effect of photon bremsstrahlung we have used the expression (4.2.3) containing the function

$$B(k) \equiv \lambda \left[2\frac{k}{\sqrt{s}} \left(\frac{k}{\sqrt{s}} - 1\right) + \left(1 + \frac{3}{4}\lambda\right) \left(\frac{2k}{\sqrt{s}}\right)^{\lambda} \right] \tag{4.A.3}$$

In terms of this one obtains for the total distribution $\tilde{\sigma}_t(s)$ without and with photon bremsstrahlung:

$$\tilde{\sigma}_t(s) = \int_0^{k_{max}} \tilde{\sigma}(s - 2k\sqrt{s}) \, B(k) \, dk \tag{4.A.4}$$

Then the correct way to introduce cuts into this expression is

$$\tilde{\sigma}_t(s,cuts) = \int_0^{k_{max}} dk\ B(k) \int \chi(\Phi,k)\ |M|^2\ d\Phi(s)$$

4.A.5

We remark that in most cases we consider χ to be a function of k, so that $\sigma_t(s,cuts)$ cannot, in general be expressed in terms of $\sigma(s,cuts)$.

Appendix 4.B

Here we present analytic results regarding the background from $e^+e^- \to Zt\bar{t}$, i.e. arising from the processes (4.4.1).

We denote by M_1 and M_2 the amplitudes of graphs 4.1(c) and 4.1(c′) respectively when the $t\bar{t}$ pair is produced via γ^* exchange; we denote by M_3 and M_4 the amplitudes of the same graphs when $t\bar{t}$ is produced via Z^* exchange. Summing over final spins and polarization and averaging over initial spins, we shall decompose the final answer as follows:

$$\begin{aligned}\Sigma\,|M_1+M_2+M_3+M_4|^2 &= \Sigma\,|M_1+M_2|^2 + \Sigma\,|M_3+M_4|^2 + \\ &+ 2\mathrm{Re}\,\Sigma\, M_1\, M_3^+ + 2\mathrm{Re}\,\Sigma\, M_1\, M_4^+ \\ &+ 2\mathrm{Re}\,\Sigma\, M_2\, M_3^+ + 2\mathrm{Re}\,\Sigma\, M_2\, M_4^+ \quad ,\end{aligned}$$

4.B.1

We write the $Zf\bar{f}$ coupling as $-i\gamma^\mu(a_f-b_f)$; here f=electron or top quark and a_f, b_f are the standard model couplings. We denote by e_t the charge of the t (=2e/3). Then referring to the 4-momenta as in Figures 4.1(c), (c′) we obtain:

$$\begin{aligned}\Sigma\,|M_1+M_2|^2 &= 4(A_Z^{e^2}+B^{Z^{e^2}})\frac{e^2 e_t^2}{(q^2)^2}\Big[\frac{1}{((q-p_1)^2)^2}\Big(F(p^1,p_2)+\frac{2p_2\cdot k}{M_Z^2}F(p_1,k)\Big) \\ &+ (p_1 \leftrightarrow p_2) + \frac{2}{(q-p_1)^2(q-p_2)^2}\Big(G-\frac{H}{M_Z^2}\Big)\Big] \quad ,\end{aligned}$$

4.B.2

where:

$$F(p_1,p_2) = m_t^2(4p_1{\cdot}q\,p_2{\cdot}q-sq^2) + (s-2p_2{\cdot}q)(4p_1{\cdot}p_3\,p_1{\cdot}p_4 - p_1q^2)$$

$$+\ 2(2p_1{\cdot}q-q^2)(p_1{\cdot}p_3\,p_2p_4 + p_1{\cdot}p_4\,p_2p_3) \quad ,$$

4.B.3

$$G = sq^2(2m_t^2+q^2) + (p_1{\cdot}q+p_2{\cdot}q-s)(4p_1{\cdot}p_3\,p_2{\cdot}p_4+4p_1{\cdot}p_4\,p_2p_3-sq^2)$$

$$-\ (p_1{\cdot}p_3\,p_1{\cdot}p_4\,p_2{\cdot}q+p_2{\cdot}p_3\,p_2{\cdot}p_4\,p_1{\cdot}q) \quad ,$$

4.B.4

$$H = (2p_1{\cdot}q-q^2)(2p_2{\cdot}q-q^2)(sm_t^2+2p_1{\cdot}p_3\,p_2{\cdot}p_4+2p_1{\cdot}p_4\,p_2{\cdot}p_3) \,.$$

4.B.5

Furthermore:

$$\Sigma\,|M_3 + M_4|^2 = 4\frac{(A_Z^{e\,2}+B^{Ze^{2}})^2}{(q^2\text{-}M_Z^2)^2}\Big[\frac{1}{((q-p_1)^2)^2}\Big(J(p_1,p_2)+\frac{2p_2{\cdot}k}{M_Z^2}J(p_1,k)\Big)$$

$$+\ (p_1\leftrightarrow p_2) + \frac{2}{(q-p_1)^2(q-p_2)^2}\Big(K-\frac{L}{M_Z^2}\Big)\Big] \quad ,$$

4.B.6

where:

$$J(p_1,p_2) = 2B_Z'^{\,2}m_t^2(sq^2-4p_1{\cdot}q\,p_2{\cdot}q) + (A_Z'^{\,2}+B_Z'^{\,2})F(p_1,p_2) + B_Z'^{\,2}\,\frac{m_t^2}{M_Z^4}\,(q^2-2M_Z^2)(2p_1{\cdot}q-q^2)^2s \quad ,$$

4.B.7

$$K = 4B_Z'^{\,2}m_t^2s(2p_1{\cdot}q+2p_2{\cdot}q-s-2q^2) + (A_Z'^{\,2}+B_Z'^{\,2})G$$

$$-\ 2B_Z'^{\,2}\,\frac{m_t^2}{M_Z^4}\,(q^2-2M_Z^2)(2p_1{\cdot}q-q^2)\,(2p_2{\cdot}q-q^2)\,s \quad ,$$

4.B.8

$$L = -2B_Z^{t\,2} m_t^2 s(2p_1\cdot q-q^2)(2p_2\cdot q-q^2) + (A_Z^{t\,2}+B_Z^{t\,2})H$$

$$- B_Z^{t\,2} \frac{m_t^2}{M_Z^4} (q^2-2M_Z^2)\,(sq^2-4p_1\cdot qp_2\cdot q)\,(2p_1\cdot q-q^2)\,(2p_2\cdot q-q^2) \ .$$

4.B.9

Finally:

$$\mathrm{Re}\ \Sigma M_1 M_3^+ = \frac{4A_Z^t A_Z^e (A_Z^{e\,2}+3B_Z^{t\,2}) e e_t}{(q^2-M_Z^2)(q-p_1)^2(q-p_2)^2 q^2} (F(p^1,p_2)+\frac{2p_2\cdot k}{M_Z^2} F(p_1,k)) \ ,$$

$$\mathrm{Re}\ \Sigma M_1 M_4^+ = \frac{4A_Z^t A_Z^e (A_Z^{e\,2}+3B_Z^{t\,2}) e e_t}{(q^2-M_Z^2)(q-p_1)^2(q-p_2)^2 q^2} (G-\frac{H}{M_Z^2}) \ .$$

4.B.10

$\Sigma M_2\, M_4^+$ is given by $\Sigma M_1\, M_3^+$ with $p_1 \longleftrightarrow p_2$. and $\Sigma M_2 M_3^+ = \Sigma M_1 M_4^+$ The above expressions should be multiplied by a factor of N_c arising by summing over the colors of the top quark.

The quantity $\Sigma\, |M_3+M_4|^2$ has also been calculated in reference (56); our result is in agreement. The expression of reference (56) contains an additional term (last term of their eq. (4.2.8)), which vanishes by symmetry when (p_3+p_4) is kept fixed in the phase-space integral (56).

Apart from the graphs (c),(c′) there is additional background of the type $e^-e^+ \rightarrow Zt\bar{t}$ arising from graphs with a Z^* or γ^* in the s-channel. However, such graphs are of $O(\alpha)$ with respect to the main process; and since they also involve an s-channel exchange, their contribution is expected to be unimportant. We have verified this by explicit calculation at $\sqrt{s} \geq 300 GeV$ and this is also in accord with reference (56).

Note that each of the amplitude sums M_1+M_2 and M_3+M_4 separately satisfies gauge invariance in the sense that the sum vanishes when the polarization vector of the final Z is replaced by its momentum and $M_Z \rightarrow 0$

Figure Captions

Figure 4.1.

Graphs for the processes considered. (a) The main process. (b) The main process with photon bremsstrahlung from the initial electron. (c) and (c′) The graphs determining the background $e^-e^+\to Zt\bar{t}$ Graphs for the background $e^+e^-\to t\bar{t}$

Figure 4.2.

(a) Total cross sections as functions of $\sqrt{s}$ for m_H=150GeV. Solid line: the main process without branching ratios (BR) and acceptance cuts. Short dashed line: the main process with BR and acceptance cuts as in sect 3, for m_t=65GeV. Long dashed: the background $e^-e^+\to Zt\bar{t}$ without BR and acceptance cuts, for m_t=65GeV The level of 1 event/year corresponds to luminosity $L=10^{33}cm^{-2}s^{-1}$ at efficiency 1/3. (b) Total cross sections as a function m_H for $\sqrt{s}$=500GeV. Solid and dashed lines as in figure 2(a) (upper (lower) dashed line corresponds to m_t=65 (50) GeV). Long dash-dotted line: The Background $e^+e^-\to t\bar{t}$ without BR and acceptance cuts for m_t=65GeV. Short dash-dotted: The same with BR and acceptance cuts.

Figure 4.3.

Distributions $d\sigma/dE_Z$ vs E_Z (or vs $M_{H\gamma}$) at $\sqrt{s}$=500GeV for m_H=150GeV. Solid line: Main process (signal) without BR and acceptance cuts. Short dashed: same with BR and acceptance cuts (m_t=65GeV). Dash-dotted: Background $e^-e^+\to t\bar{t}$ without BR and acceptance cuts (m_t=65GeV).

Figure 4.4.

(a) Total cross sections as functions of m_H for $\sqrt{s}$=300GeV. Solid, short dashed and long dash-dotted lines as in figure 3. Short dash-dotted: background $e^-e^+ \to t\bar{t}$ with BR and acceptance cuts (m_t=65GeV). (b) same as in (a) for $\sqrt{s}$=1TeV.

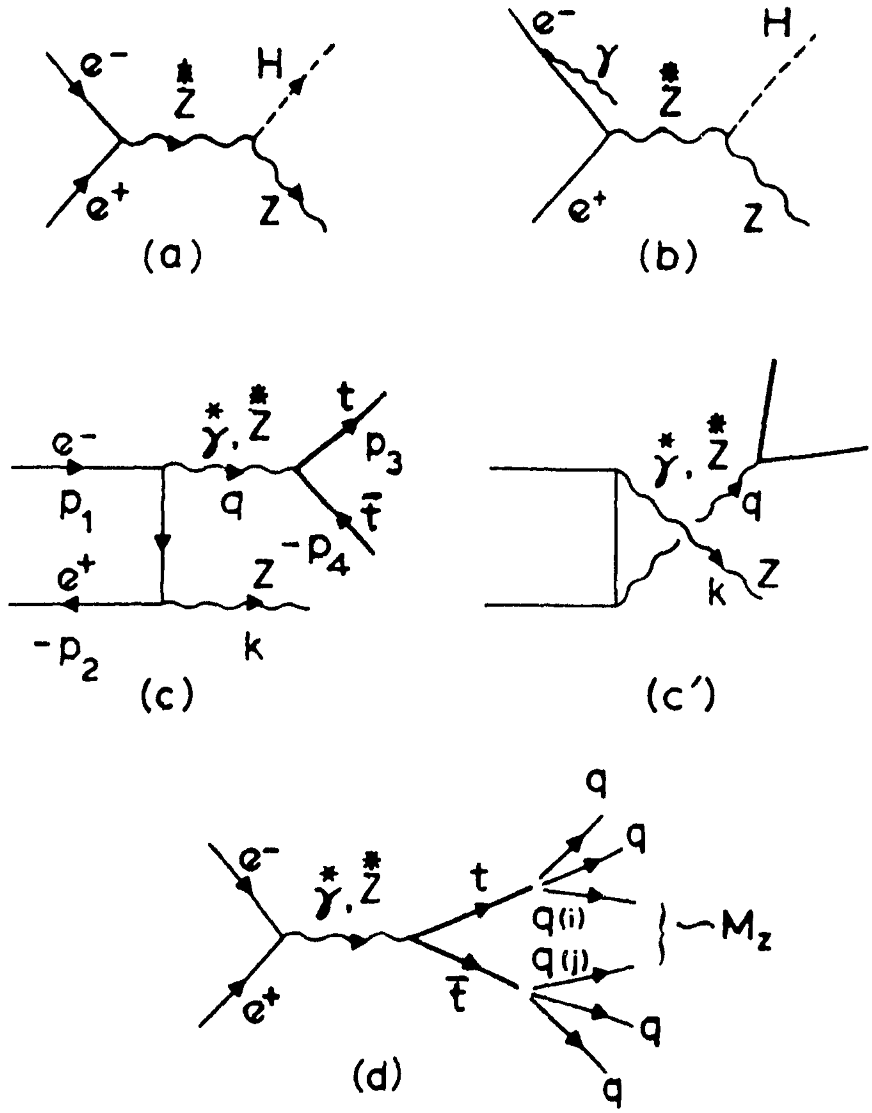

e⁻
Z*
H
e⁺
Z
(a)
e⁻
γ
Z*
H
e⁺
Z
(b)
e⁻
γ*, Z*
t
p₃
p₁
q
t̄
e⁺
Z
-p₄
-p₂
k
(c)
γ*, Z*
q
k
Z
(c′)
e⁻
γ*, Z*
t
q
q
q(i)
q(j)
M_z
t̄
e⁺
q
q
(d)

Figure 4.1

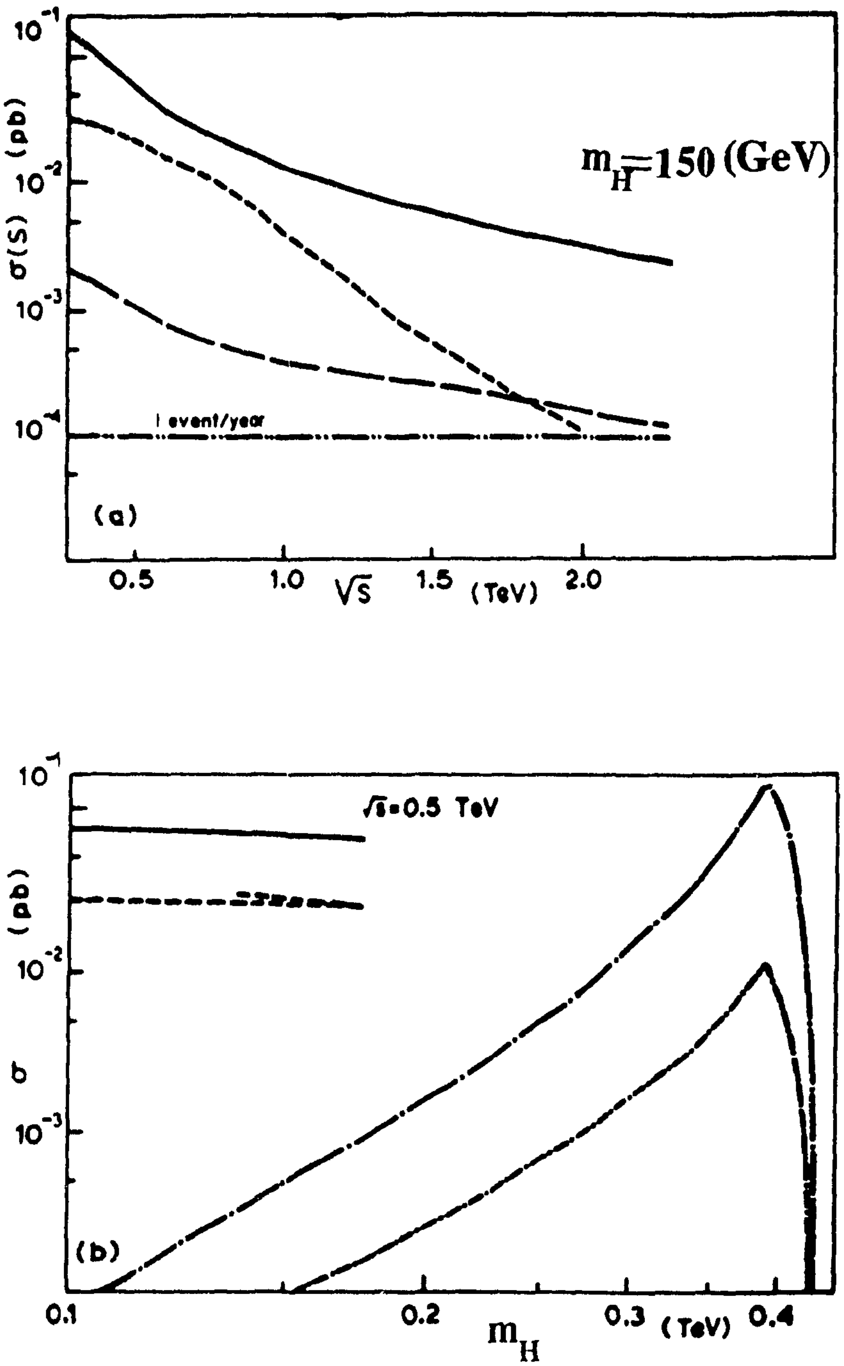

10^{-1}
10^{-2}
10^{-3}
10^{-4}
$\sigma(S)$ (pb)
m_H=150 (GeV)
1 event/year
(a)
0.5
1.0
$\sqrt{s}$
1.5
(TeV)
2.0
10^{-1}
$\sqrt{s}$=0.5 TeV
(pb)
10^{-2}
σ
10^{-3}
(b)
0.1
0.2
m_H
0.3
(TeV)
0.4

Figure 4.2

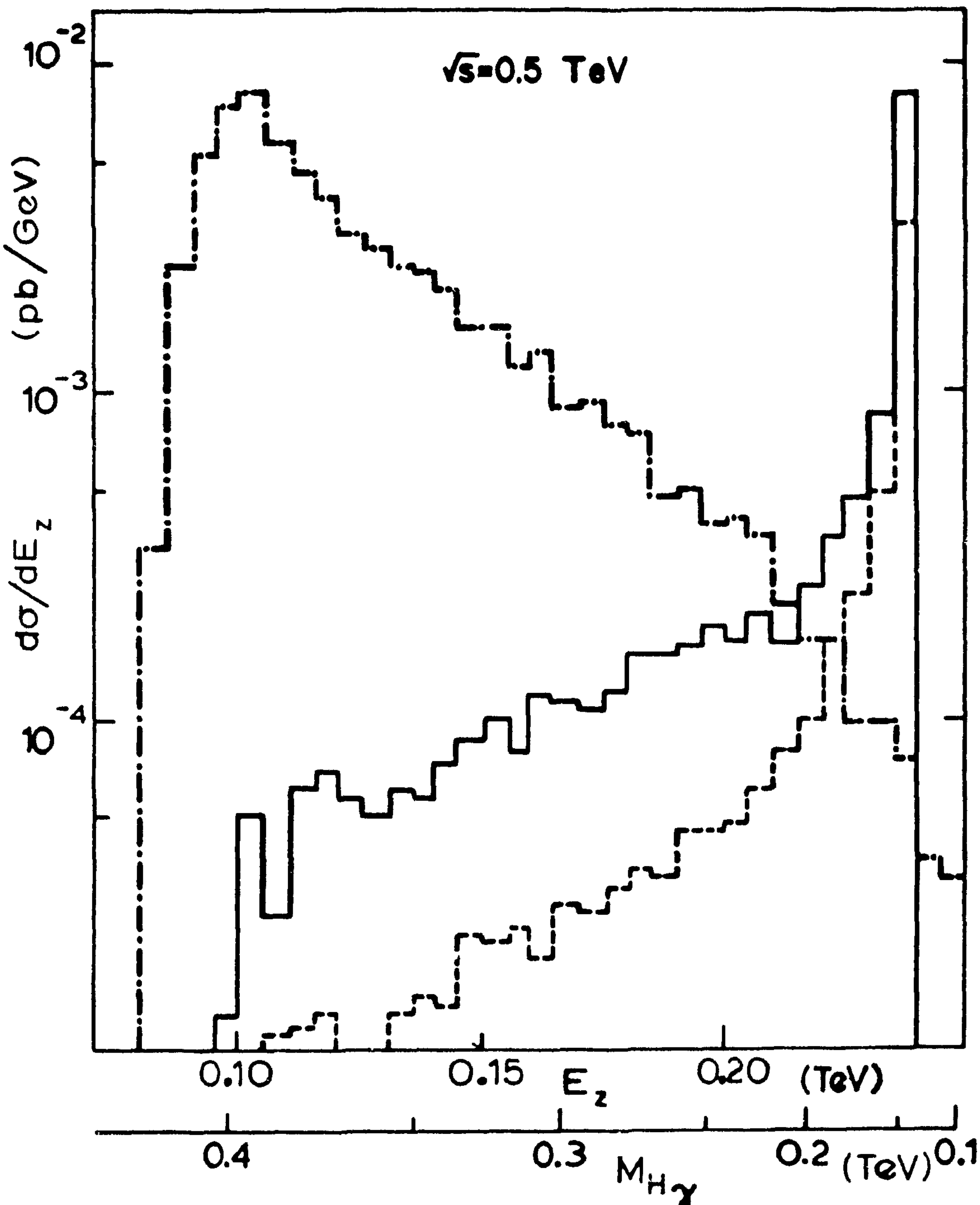

√s=0.5 TeV
dσ/dE_z (pb/GeV)
10^-2
10^-3
10^-4
0.10
0.15
E_z
0.20
(TeV)
0.4
0.3
M_Hγ
0.2
(TeV)
0.1

Figure 4.3

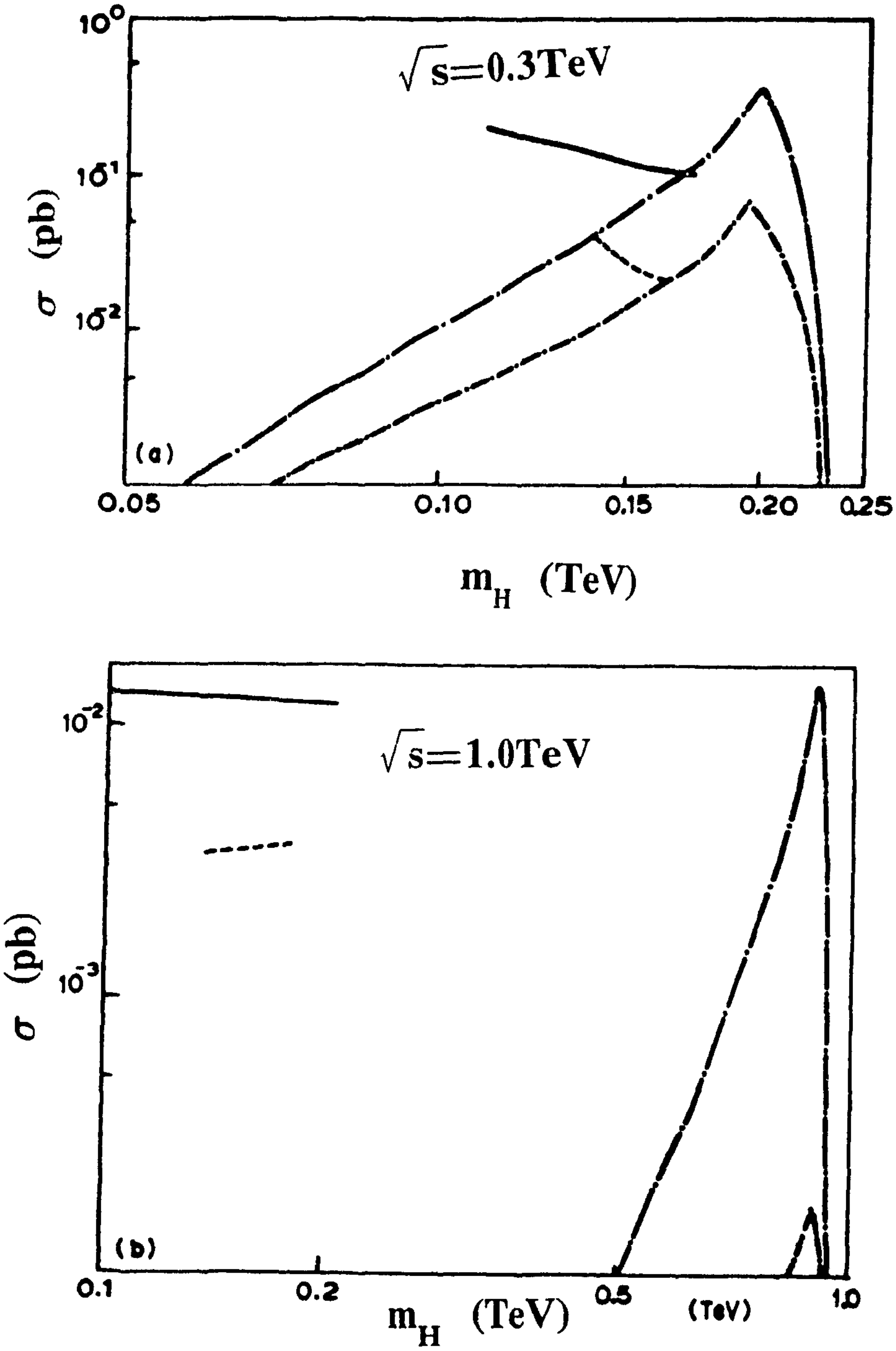

10⁰
10^{-1}
10^{-2}
σ (pb)
$\sqrt{s}$=0.3TeV
(a)
0.05
0.10
0.15
0.20
0.25
m_H (TeV)
10^{-2}
10^{-3}
σ (pb)
$\sqrt{s}$=1.0TeV
(b)
0.1
0.2
0.5
1.0
(TeV)
m_H (TeV)

Figure 4.4

CHAPTER 5

DETECTING AN INTERMEDIATE MASS HIGGS-BOSON AT THE SSC THROUGH ITS TAU-LEPTON DECAY MODE

5.1 Introduction

In chapter 4 we considered the detection of an intermediate mass Higgs-boson at a hypothetical electron-positron collider with $\sqrt{s}$=300−500GeV. Long before such a collider is built, however, the Superconducting Supercollider (SSC) will be in operation; hence it would be of great importance if an intermediate mass Higgs-boson could be shown to be detectable there.

In fact, at the SSC an intermediate mass Higgs-boson would be produced at a very high rate, 10^6 events per year, predominantly through the gluon-gluon fusion graph with a quark loop shown in figure 5.1a (reference (57)). The main obstacle to detection of such Higgs-bosons is the high backgrounds present at the SSC. For example if $m_H > 2m_t$ the main decay of the Higgs-boson is $H \rightarrow tt$ where the top-quarks appear as multiple jets. QCD jet backgrounds, however, render this kind of signal undetectable (58). Even if $m_H < 2m_t$ so that the dominant decay mode of the Higgs-boson is $H \rightarrow b\bar{b}$ it may be difficult to see though not impossible (59).

Given these difficulties in detecting the main hadronic decay of the Higgs-boson, one is led to consider other "rare" decay modes. Some of these decays present in the intermediate mass case considered in reference (60) are $H \rightarrow \gamma\gamma$, $H \rightarrow ZZ^*$, $H \rightarrow b\bar{b}$, and $H \rightarrow \tau^+\tau^-$.

Figure 5.2 (taken from (61)) shows some typical branching ratios for Higgs decay where the value of the top-quark mass m_t=55GeV has been chosen (reference (61)). In reference (60) these decay modes are considered and it is suggested that that they may be applicable for the values of m_t and m_H shown in figure 5.3 (taken from (60a)). As can be seen, the use of the $H \rightarrow \tau^+\tau^-$ decay mode could possibly be a useful alternative to some of the other decay modes and perhaps it may be of some limited use when $m_H \geq 2m_t$.

In this chapter we shall consider the detection of the intermediate mass Higgs-boson at the SSC though the $H \rightarrow \tau^+\tau^-$ decay mode. In section 5.2 we consider the $\tau^+\tau^-$ signal for the Higgs-boson produced by the gluon-gluon fusion mechanism of figure 5.1a, and the background to this from the Drell-Yan process of figure 5.1b. We then introduce acceptance cuts and consider under what conditions this signal may be seen and in section 5.3 we present our conclusions.

5.2 Detecting The Higgs-boson Using

$pp \rightarrow H \rightarrow \tau^+ \tau^-$

at The Superconducting Supercollider

The cross sections of the various Standard Model processes contributing to Higgs-boson production at the SSC ($\sqrt{s}$=40TeV) are calculated in reference (57) where the channels considered include gluon-gluon fusion, $t\bar{t}$ fusion and vector boson (WW and ZZ) fusion. These cross sections are show in figure 5.4 (taken from ref. (60)). Clearly, in the intermediate mass range gluon-gluon fusion is the dominant production mode. Moreover, the cross section for the production of a Higgs-boson through this mechanism is to a large extent independent of the mass of the top-quark in the loop. Taking an integrated luminosity of $\int L\, dt = 10^{40} cm^{-2} = 10^4 pb^{-1}$ (the estimated integrated luminosity for one year at the SSC), this cross section corresponds roughly to 10^6 events per year. Using the branching rations shown in Figure 5.2, if $m_H \leq 2m_t$ there will be $10^4 - 10^5$ events where $H \rightarrow \tau^+ \tau^-$, while if $m_H > 2m_t$ this drops rapidly to $\sim 10^3$ events.

In spite of the large number of events the identification of such a signal is difficult. In principle, if the total momentum of each of the τ^+, τ^- could be determined, such events could be identified by the invariant mass, m_0 of the τ – pair since all τ– pairs originating from $H \rightarrow \tau^+ \tau^-$ would have $m_0 = m_H$. A $\tau^\pm$ however travels only about 1 cm before it disintegrates, hence its momentum cannot be directly observed and since the decay of the $\tau^\pm$ always results in an undetectable ν_τ, the decay products will only carry part of the initial momentum of the $\tau^\pm$. Let us denote the initial momentum of the τ^+ by p_1 and the momentum of the τ^- by p_2. When the τ^+ decays the products will consist of a number of unobserved neutrinos and a number of other particles (hadrons and charged leptons) which can be observed. Let us denote the momentum of the neutrinos by $p_{1\,\nu}$ and the momentum of the other observable decay products by $p_{1\,obs}$ hence $p_{1\,\nu}+p_{1\,obs}=p_1$. Likewise the momentum of the neutrinos and observed particles from the τ^- are denoted by $p_{2\,\nu}$ and $p_{2\,obs}$ respectively.

In some instances of $\tau^\pm$ decay only a small part of the momentum will be carried by the neutrinos; hence, if we define the quantity

$$m_{obs} = |p_{1\,obs}+p_{2\,obs}| \tag{5.2.1}$$

we expect in those cases that m_{obs} will give a good approximation to m_H, while in general $m_{obs} \leq m_H$.

Figure 5.5 shows the distribution $d\sigma/\,dm_{obs}$ for m_H= 80, 120, and $135GeV$ where we have taken m_t=$65GeV$ (solid lines). Note that $0 < m_{obs} < m_H$ and in fact the distribution is smooth within the allowed range, those events towards the upper edge being the ones with most of the momentum of the $\tau^\pm$ carried by observable particles.

The main background to $pp \to H \to \tau^+\tau^-$ is the Drell-Yan process $pp \to q\bar{q} \to Z$ or $\gamma \to \tau^+\tau^-$ depicted in figure 5.1b; the distribution $d\sigma/\,dm_{obs}$ from this background is also shown in figure 5.5 (dashed line).

Clearly, τ pairs from the Z peak give enormous backgrounds for $m_{obs} \leq M_Z$ so that unless these events are cut away the signal from the Higgs-boson will be undetectable. We therefore introduce a cut

$$m_{obs} > m^0_{obs} = 95GeV \tag{5.2.2}$$

With this cut, a Higgs boson with mass $m_H \leq m^0_{obs} \approx M_Z$ cannot be seen and even in the range $M_Z \leq m_{obs}$ there is considerable background from the Drell-Yan process. For instance taking $m_t = 65GeV$, the number of background events at the SSC in a year in the range $m^0_{obs} \leq m_{obs} \leq 130GeV$ is 1.5×10^5 while the signal for m_H $120GeV$ is 5.3×10^3. If we take $m_H = 135GeV$, just above the tt threshold, the signal goes down to 1.5×10^3.

In principle the signal in the $m_H = 120GeV$ case has a statistical significance of $\sim 15\sigma$ at SSC luminosities; however its observation would require knowing the background to a level of $<3\%$. Detector uncertainties would make this difficult to achieve, hence it is useful to consider further possible cuts.

The main difficulty in reconstructing the Higgs-boson mass is that some of the center of mass energy of the initial Higgs-boson is lost to the neutrinos. It makes sense therefore to select events where this loss is *a priori* likely to be minimal. The best way to do this is to select decay modes of the $\tau^{\pm}$ which have many observable final products to carry the momentum. From reference (62) we find that the following decay modes satisfy this condition:

$\tau^- \rightarrow \pi^-\pi^0\pi^0\nu_\tau$	7.5%
$\tau^- \rightarrow \pi^-\pi^0\pi^0\pi^0\nu_\tau$	3.0%
$\tau^- \rightarrow \pi^-\pi^-\pi^+\nu_\tau$	6.8%
$\tau^- \rightarrow \pi^-\pi^-\pi^+\nu_\tau \geq 1\ \pi^0$	6.4%
total=	23.7%

5.2.3

We will call these decay modes 'multi-pi' decay modes. Figure 5.6 shows a histogram of the fraction, x, of the initial energy of a $\tau^\pm$ carried by the observable particles in multi-pi decays assuming that the initial energy of the $\tau^\pm$ is m_τ. We denote this probability by $f_\pi(x)$. As can be seen, there is a well defined peak at $x \approx 0.8$ demonstrating that most of the momentum of the $\tau^\pm$ will be carried by observable particles.

Although the neutrinos themselves are unobservable, the transverse component of momentum carried by them may be detected as missing transverse momentum from the whole event. For example if the Higgs-boson is initially produced with no transverse momentum, $(p^T_{1obs}+p^T_{2obs})$ $(p^T_{1\nu}+p^T_{2\nu})$ (T indicates the transverse component). Using this extra information with the more favourable multi-pi events, we will try to construct a more accurate estimate of the mass of the $\tau^+\tau^-$ system.

An effect which must be taken into account if we are to use the missing transverse momentum of the $\tau^+\tau^-$ system is the initial transverse momentum of the Higgs-boson due to initial state gluon radiation. To estimate this effect, we ran the ISAJET 5.31 (63) simulation which takes into account the initial state gluons. Figure 5.7 shows the resulting average transverse momentum of Drell-Yan events at various values of $\sqrt{\hat{s}}$ where we find that δ_I, the average initial transverse momentum satisfies

$$\delta_I = 6.3 + .318\sqrt{s} \tag{5.2.5}$$

Based on this we will make the possibly crude assumption that for both the signal and background the value of δ_I is $\sim 50 GeV$.

In our reconstruction algorithm we will also use the assumption that the m_τ is small compared to the energy of the $\tau^\pm$. This is justified since the mass of the $\tau^\pm$ is $1.7 GeV$ while the transverse momentum is $\sim 100 GeV$. If x_1 is the fraction of energy of the τ^+ which appears as observable particles and x_2 is the fraction of energy of the τ^- which appears as observable particles, the assumption that the $\tau^\pm$ is massless implies

$$\begin{aligned} p_{1\,obs} &= x_1\, p_1 & \qquad p_{1\,\nu} &= (1-x_1)\, p_1 \\ p_{2\,obs} &= x_2\, p_2 & \qquad p_{2\,\nu} &= (1-x_2)\, p_2 \end{aligned} \tag{5.2.6}$$

Thus in terms of the momentum fractions x_i and the observed momenta $p_{i\,obs}$ the initial transverse momentum of the $\tau^+\tau^-$ system is

$$p_{II} = \frac{1}{x_1} p^I_{1\,obs} + \frac{1}{x_2} p^I_{2\,obs} \; . \tag{5.2.7}$$

In order to determine the missing transverse momentum one must add up the total transverse momentum of the event including the observed particles from the τ^+, τ^- as well as other hadrons produced in the event. Inevitably some error is introduced when such a quantity is measured experimentally. Let us denote the root mean square average value of $|\not{p}_{Tmm}|$ by δ_{mm}. We take $\delta_{mm} \sim 30 GeV$ and further make the possibly crude assumption that it is Gaussian (64). We will denote by $\not{p}_T^{obs}$ the total observed missing transverse momentum due to neutrinos which includes the true missing transverse momentum and missing transverse momentum due to mismeasurement. Denoting the (false) missing transverse momentum due to mismeasurement by $\not{p}_T^{mm}$ we have the equality

$$\not{p}_T^{obs} = p_{1\nu} + p_{2\nu} + \not{p}_T^{mm}.$$

5.2.8

Thus, in terms of the observed momenta and the momenta fractions, $\not{p}_T^{mm}$ is given by

$$\not{p}_T^{mm} = \not{p}_T^{obs} - \frac{1-x_1}{x_1} \cdot p_{1obs} - \frac{1-x_2}{x_2} \cdot p_{2obs}$$

5.2.9

If we now make the assumption that the mismeasured transverse momentum and the transverse momentum of the initial state gluon radiation is roughly gaussian, we can construct the following likelihood function of the variables x_1 and x_2 and the observed quantities:

$$L(x_1,x_2) = \ln f_\pi(x_1) + \ln f_\pi(x_2)$$
$$- \frac{(p_{Tl})^2}{\delta_l^2} - \frac{(\not{p}_T^{\,mm})^2}{\delta_{mm}^2}$$

5.2.10

where $\not{p}_T^{\,mm}$ and p_{Tl} are given in terms of the observed quantities and x_1 and x_2 by eqs. 5.2.8 and 5.2.6.

This function represents the logarithm of the probability that given values of x_1 and x_2 will give rise to the observed value of $\not{p}_l$ and p_{lT}. Roughly speaking $L(x_1,x_2)$ gives an indication of (the logarithm of) how likely it is that given values of these variables explain the observed quantities.

If we define $\hat{x}_1$ and $\hat{x}_2$ as the values of x_1 and x_2 which minimize L then, we will define the reconstructed mass as

$$m_{recon} = \frac{2\, p_{1\,obs} \cdot p_{2\,obs}}{\hat{x}_1 \hat{x}_2}$$

5.2.11

Figure 5.8 shows $d\sigma/dm_{recon}$ as a function of m_{recon} with the cut for various combinations of m_H and m_t where we simulate the mismeasurement of the missing transverse momentum before we find m_{recon} we have imposed the cut $m_{obs} > m^0_{obs} = 95GeV$ for the signal and Drell-Yan background and chosen $m_H \sim 2m_t$.

If we take as a criterion of observablity that the signal be at least 10% of the background and that the signal have a significance of at least 5 σ in a $15GeV$ range around the peak, the signal must lie above the dotted line in figure 5.8 over a $15GeV$ range. This criterion is easily satisfied for cases where $m_H < 2m_t$ but the limit to the extent to which one can go into the region $m_{ll}>2m_t$ is only about 5 GeV.

Figure 5.3 show the region of the $m_{ll}-m_t$ plane in which this condition can be satisfied. The lower limit on m_{ll} is due to the overwhelming background from the Z resonance.

5.3 Conclusions

Using the series of cuts and the maximum likelihood method described above, it may be possible to detect a Higgs-boson of intermediate mass through $H \rightarrow \tau^+\tau^-$ at the SSC, when the mass of the Higgs-boson and the top-quark are as indicated in figure 5.9. Although this does not extend very far into the region $m_H \geq 2m_t$ it could provide an additional method of identification of the Higgs-boson through other decay modes.

In principle one could obtain similar results by looking for a downwards step in the Histogram vs. m_{obs}. However since this step, although statistically significant, would only be a few percent of background, knowledge of the systematic errors to that level would be required.

If either of these method is to be used, however, there is still the experimental problem of the efficiency with which the τ leptons may be identified and the difficulty of identifying the multi π events to be resolved. For example, if even a small fraction of QCD 2-jet events are mistaken for τ pairs, the signal could be overwhelmed.

Figure Captions

Figure 5.1

(a) Feynman diagram for $gg \rightarrow H \rightarrow \tau^+\tau^-$ through a quark loop. (b) Feynman diagram for the background process $q\bar{q} \rightarrow \tau^+\tau^-$. The intermediate particle may be a real or virtual Z or γ.

Figure 5.2

The branching ratios for Higgs-boson decay as a function of m_H taking m_t $55 GeV$. The branching ratio for $H \rightarrow t\bar{t}$ is shown with a solid line; $H \rightarrow b\bar{b}$ is shown with long dashes; $H \rightarrow \tau^+\tau^-$ is shown with a dash-dot-dot-dot line; $H \rightarrow \gamma\gamma$ is shown with small dots; $H \rightarrow WW^*$ is shown with large dots and $H \rightarrow ZZ^*$ is shown with short dashes. (from reference (61))

Figure 5.3

Regions of the $m_H - m_t$ plane where it may be feasible to detect the Higgs-boson at the SSC. If these quantities fall between the two solid lines, the Higgs-boson may be detected by $H \rightarrow \gamma\gamma$; to the left of the long dashes, it may be detected by $H \rightarrow b\bar{b}$; above the dash-dot line, through $H \rightarrow ZZ^*$; and above the dash-dot-dot line, through $H \rightarrow \tau^+\tau^-$. The short dashes indicate the line $m_H = 2m_t$ and the hatched region is eliminated because $m_t \leq 45 GeV$. (taken from ref. (60a))

Figure 5.4

The cross section for the production of the Higgs-boson at the SSC ($\sqrt{s}$=40TeV). The solid lines indicate the cross section through gluon fusion (figure 5.1a) with m_t=30, 40, 60, 100, 150, and 200TeV; the dotted line indicates the cross section for ZZ or WW fusion; and the dashed lines indicate the cross section for $t\bar{t}$ fusion. (taken from ref. (60a))

Figure 5.5

The quantity $d\sigma/dm_{obs}$ is shown as a function of m_{obs} for the process $g\bar{g}\rightarrow H\rightarrow\tau^+\tau^-$ (solid lines) taking m_H=80, 120, and 135GeV with m_t=65GeV. The background Drell-Yan process $q\bar{q}\rightarrow\tau^+\tau^-$ is shown with the long dashed line. The numbers between the dashed lines indicate the number of events which fall between these two lines (taking an integrated luminosity of $10^{40}cm^{-2}$) for the signal (with m_H=120, 135GeV) and background.

Figure 5.6

A graph of the function $f_\pi(x)$ as a function of x (arbitrary normalization).

Figure 5.7

A graph of δ_f as a function of $\sqrt{\hat{s}}$. The dots indicate ISAJET results and the line is a linear fit to these results.

Figure 5.8

A graph of the quantity $d\sigma/dm_{recon}$ as a function of m_{recon}. The signal is indicated by solid lines for the values of (m_t,m_H) (55,115), (65,120), (75,155), and (85,175); the background is indicated by the dashed line. In order for the signal to satisfy the observability criterion, the peak of the curve must be above the dotted line over a range of 15GeV.

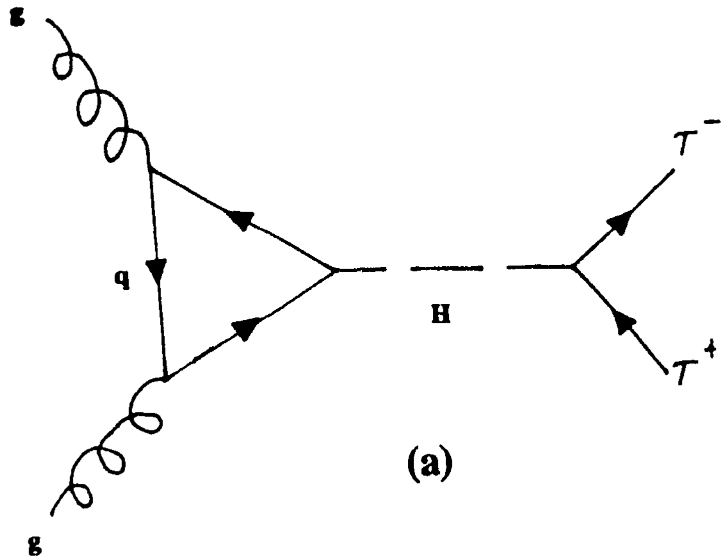

(a)

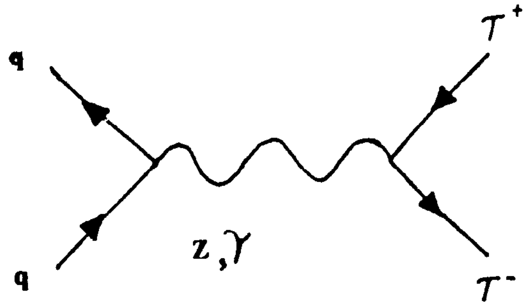

(b)

Figure 5.1

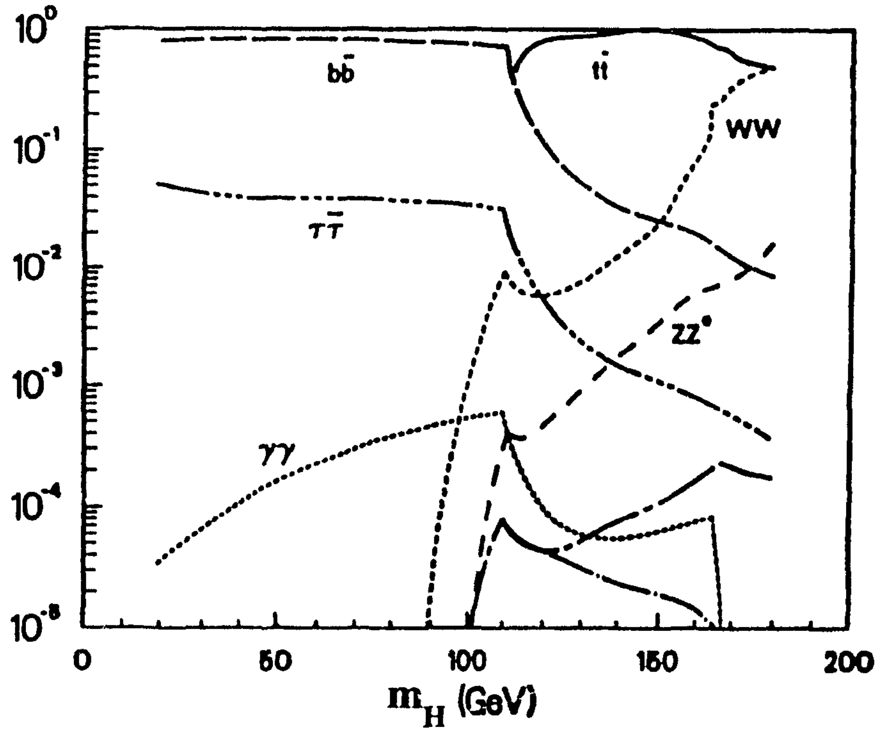

10^0
10^{-1}
10^{-2}
10^{-3}
10^{-4}
10^{-5}
$b\bar{b}$
$t\bar{t}$
WW
$\tau\bar{\tau}$
ZZ^*
$\gamma\gamma$
0
50
100
150
200
m_H (GeV)

Figure 5.2

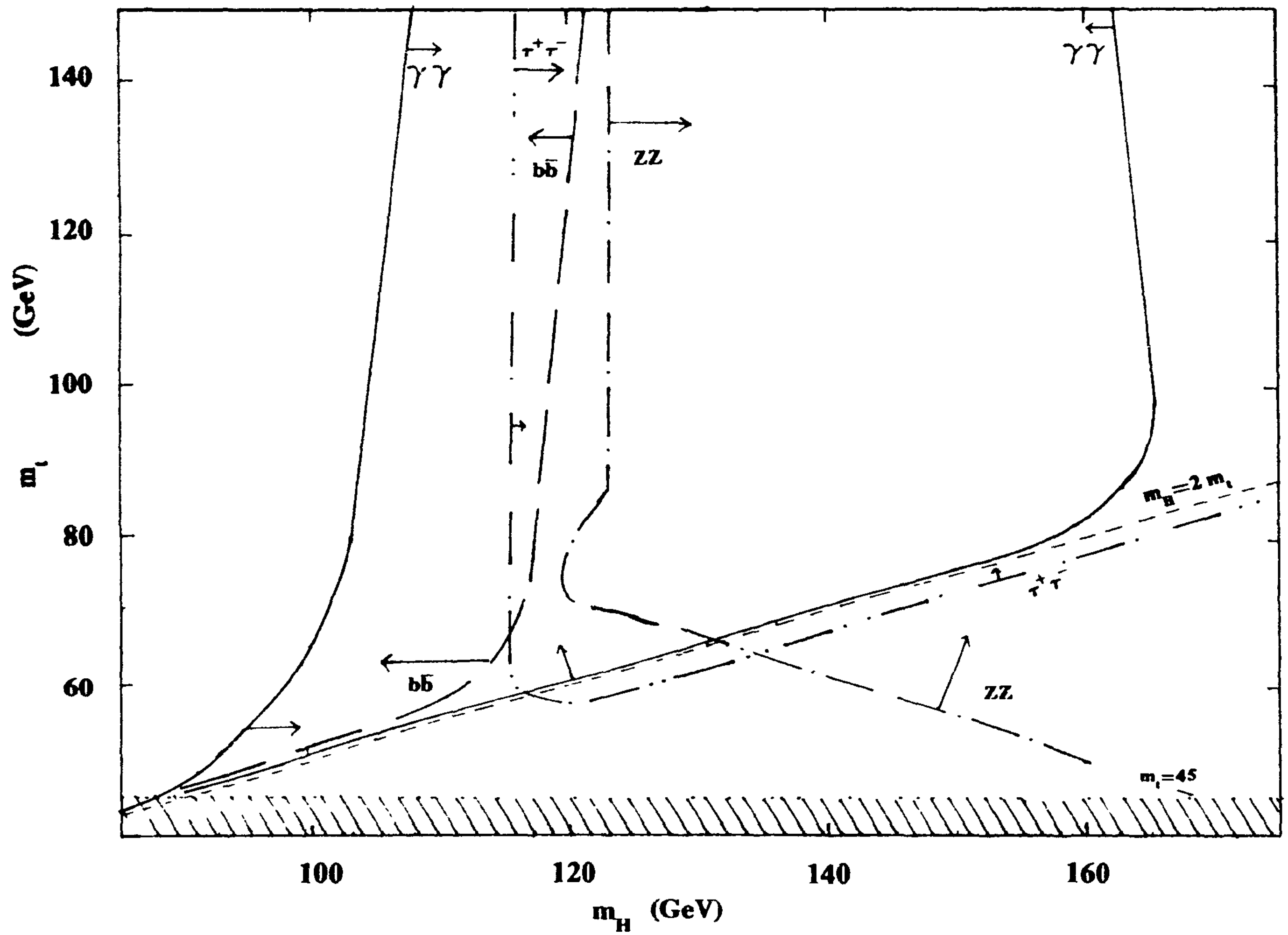

140
120
100
80
60
m_t (GeV)
$\gamma\gamma$
$\tau^+\tau^-$
$b\bar{b}$
ZZ
$\gamma\gamma$
$m_H = 2\,m_t$
$\tau^+\tau^-$
$b\bar{b}$
ZZ
m_t=45
100
120
140
160
m_H (GeV)

Figure 5.3

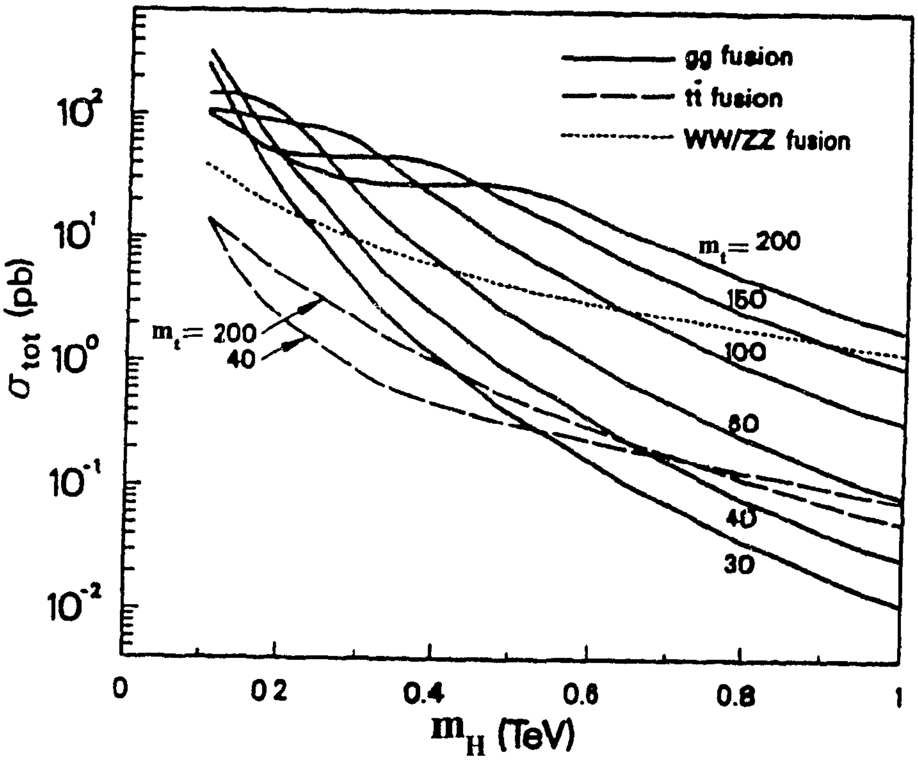
gg fusion
$t\bar{t}$ fusion
WW/ZZ fusion
$m_t = 200$
150
100
80
40
30
$m_t = 200$
40
10^2
10^1
10^0
10^{-1}
10^{-2}
σ_{tot} (pb)
0
0.2
0.4
0.6
0.8
1
m_H (TeV)

Figure 5.4

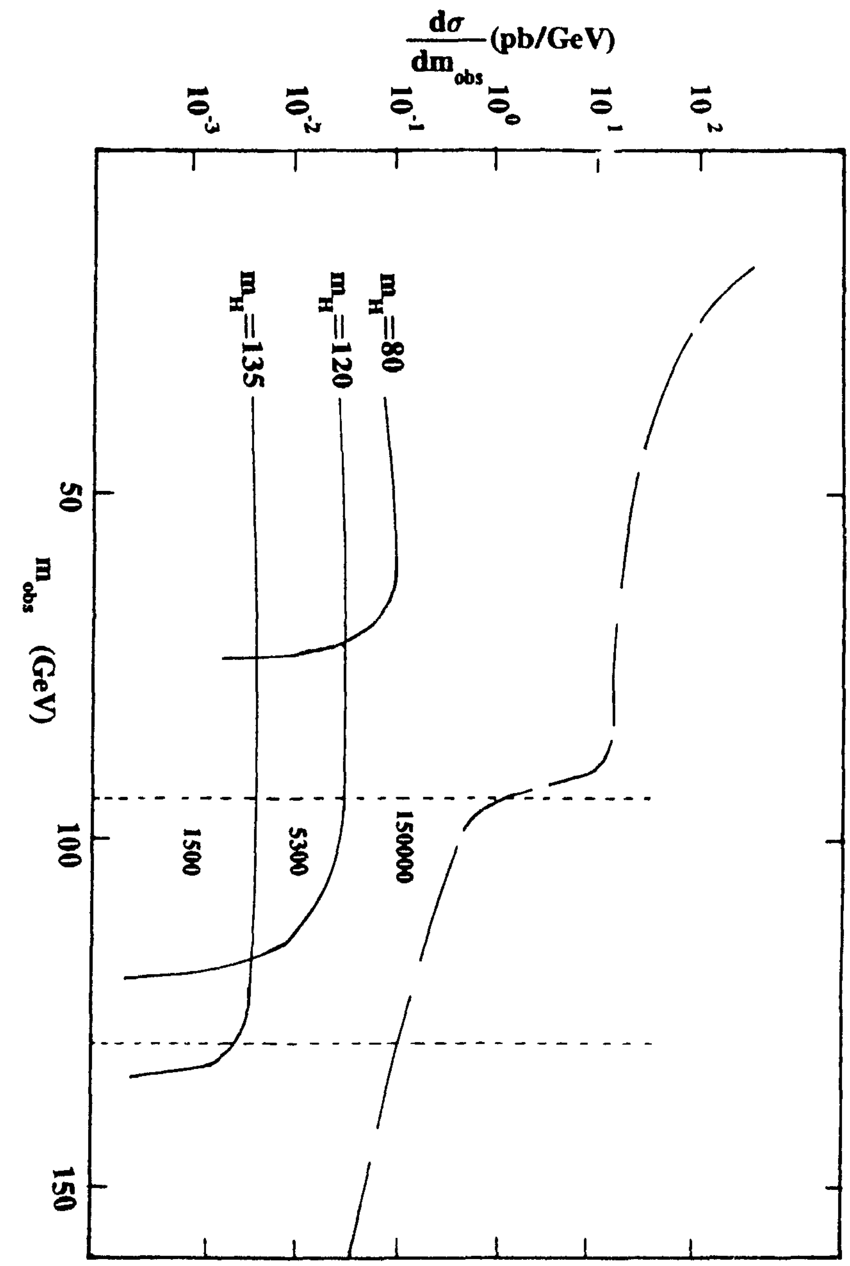

dσ/dm_obs (pb/GeV)
10^-3
10^-2
10^-1
10^0
10^1
10^2
m_H=80
m_H=120
m_H=135
150000
5300
1500
50
100
150
m_obs (GeV)

Figure 5.5

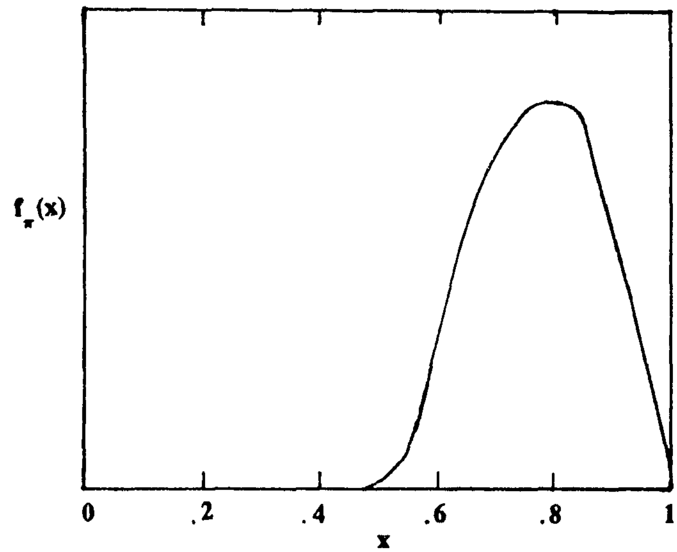

Figure 5.6

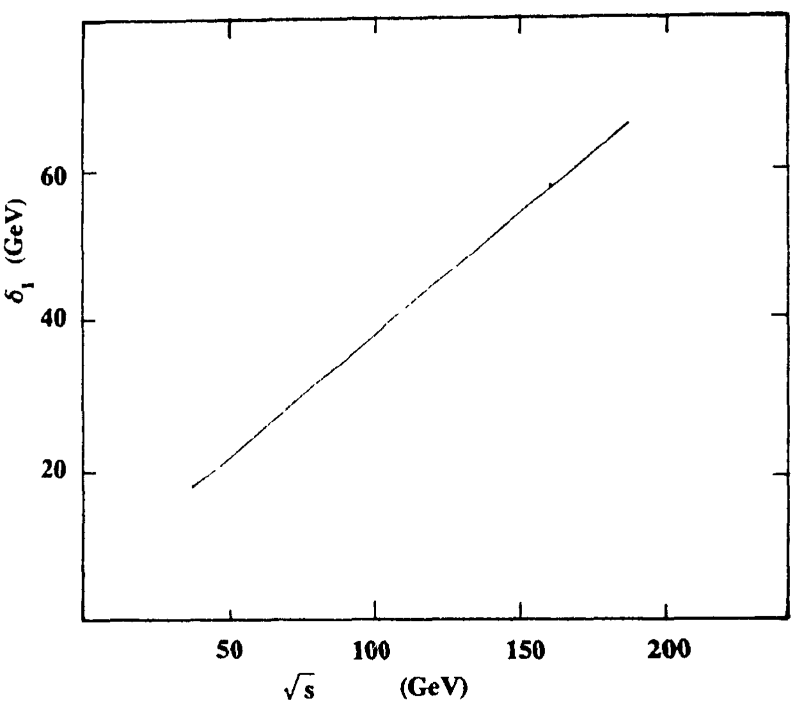

Figure 5.7

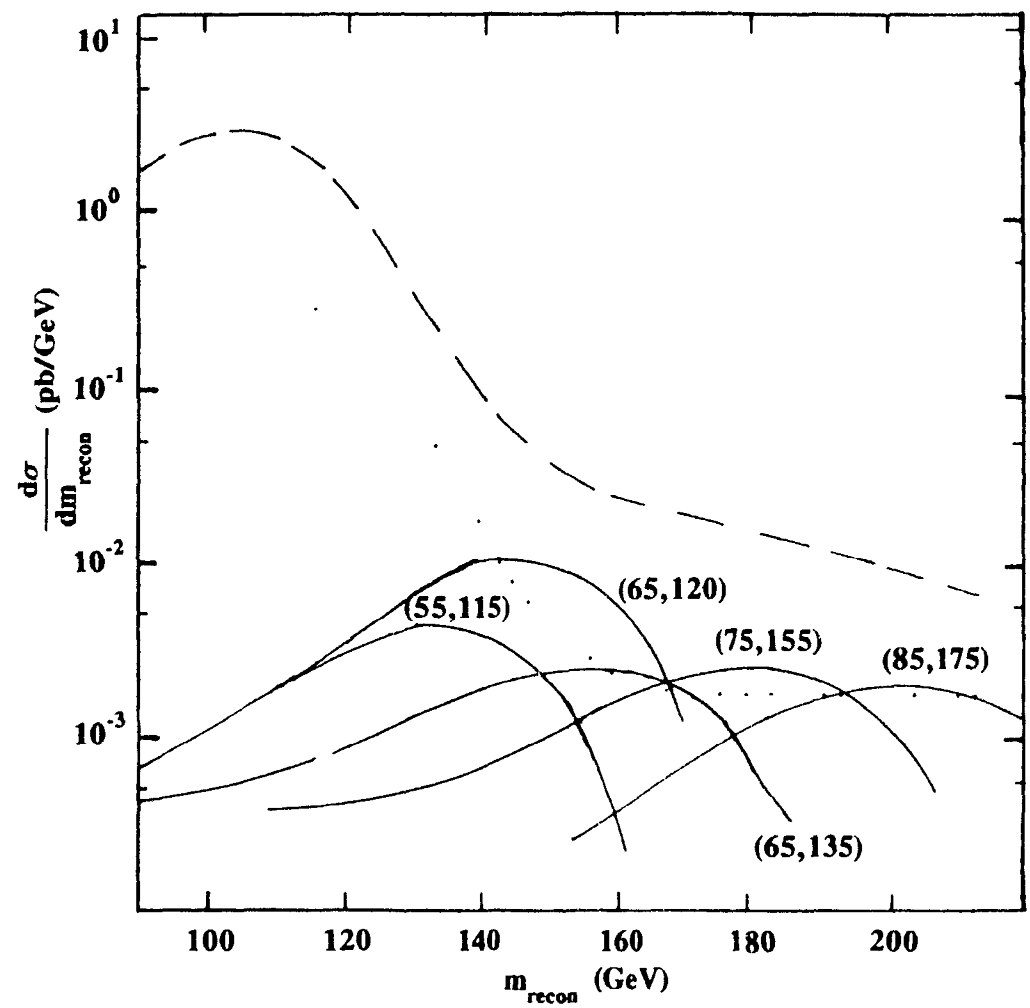

10^1
10^0
10^{-1}
10^{-2}
10^{-3}
$\frac{d\sigma}{dm_{recon}}$ (pb/GeV)
(65,120)
(55,115)
(75,155)
(85,175)
(65,135)
100
120
140
160
180
200
m_{recon} (GeV)

Figure 5.8

CHAPTER 6

USING A DISPERSIVE APPROACH TO A HEAVY HIGGS-BOSON

6.1 Introduction

For a sufficiently large Higgs-boson mass (m_H), it is expected that the Higgs sector becomes strongly interacting; thus perturbation theory will fail. This can be seen by rewriting the standard model Higgs-boson self coupling from Chapter 1 in terms of the Fermi constant: we find $g_{HHH}=G_F m_H^2$. This happens in particular when $m_H^2 \sim G_F$ and so $m_H \sim O(1 TeV)$. In this chapter we are led to consider a non-perturbative approach, dispersion relations, particularly with regard to a Higgs-boson with a mass in this range.

In this method, one constructs amplitudes satisfying analyticity and unitarity constraints. However, the approach necessarily involves several assumptions and simplifications, and we cannot claim precise quantitative predictions. Our goal is far more modest and consists of constructing certain models which may give some insight regarding the following questions about a heavy Higgs-boson: (a) How do the actual amplitudes differ from those of perturbation theory at tree level? (b) Is there any indication of strong interaction effects, such as bound states or resonances? (c) Is there any indication that the Higgs-boson itself arises as a bound state or resonance?

At sufficiently high energies the interactions with longitudinally-polarized gauge bosons (W_L,Z_L) dominate. In the high energy limit, we may use the equivalence theorem (66,67) which allows us to replace W_L, Z_L by the corresponding Goldstone scalars (eaten via the Higgs mechanism to provide the longitudinal degrees of freedom) thus yielding a theory of scalar-scalar interactions. This formalism considerably simplifies the mathematical treatment throughout.

In section 6.2 we consider the applications of dispersive methods to Higgs-Higgs scattering taking into account only Higgs-boson self interactions. In section 6.3 we consider the analogous case of $Z_l Z_l$ scattering through the exchange of a Higgs-boson and in section 6.4 we present our conclusions.

6.2 The channel

HH→HH

We begin with the simplest case of elastic scattering of Higgs-bosons. In perturbation theory (tree level) the amplitude for this process is (figure 6.1a) (67) :

$$F(s,t) = \lambda\left[-\frac{1}{3m_H^2} + \frac{1}{m_H^2 - s} + \frac{1}{m_H^2 - t} + \frac{1}{m_H^2 - u}\right]$$

6.2.1

where

$$\lambda = \frac{9\sqrt{2}}{16\pi} G_F m_H^4 .$$

In the center of mass frame of $HH \to HH$ let $|\vec{q}|$ = the momentum of the Higgs-boson, θ = scattering angle. Setting $|\vec{q}|^2 = \nu$, the invariants are given by

$$s = 4(\nu + m_H^2), \quad t = -2\nu(1 - \cos\theta), \quad u = -2\nu(1 + \cos\theta)$$

Considering the partial wave expansion

$$F(s,t) = \sum_l (2l + 1)\, F_l(\nu) P_l(\cos\theta) \quad ,$$

6.2.2

the projections of the terms $\lambda/(m_H^2 - t)$ and $\lambda/(m_H^2 - u)$ of eq 6.2.1 onto the l^{th} partial wave are

$$F_l^{t\text{-}exch}(\nu) = \frac{\lambda}{2\nu} Q_l(1+\frac{m_H^2}{2\nu})$$

$$F_l^{u\text{-}exch}(\nu) = (-1)^l \frac{\lambda}{2\nu} Q_l(1+\frac{m_H^2}{2\nu}) \ ,$$

6.2.3

where $Q_l(\xi)$ are the Legendre functions of the second kind. The first two terms of eq. (6.2.1) contribute only to $l=0$ with

$$B_l(\nu) = F_l^{t\text{-}exch}(\nu) + F_l^{u\text{-}exch}(\nu)$$

6.2.4

perturbation theory gives:

$$F_l^{pert}(\nu) = B_l(\nu) + \lambda(\frac{-1}{3m_H^2} + \frac{1}{m_H^2 - s})\delta_{l0} \ .$$

6.2.5

In dispersion theory (68) we construct the amplitude as depicted in figure 6.1b. Specifically, as a Born term (the "force" in our model) we take $B_l(\nu)$ of eqs. 6.2.4, 6.4.3. To this we add the rescattering of two Higgs-bosons (intermediate as well as initial and final particles on the mass-shell). We assume that the higher mass exchanges (for example two Higgs-bosons in the t-channel and u-channel) can be neglected; in the dispersion approach this means that they introduce distant singularities.

Then regarding the analyticity properties in ν of $F_l(\nu)$, $Q_l(\xi)$ has a branch cut $-1\leq\xi\leq1$; this introduces a branch cut (the left-hand cut): $-\infty<\nu\leq-m_H^2/4$, with the corresponding discontinuity in $F_l(\nu)$:

$$\Delta F_l(\nu) = \lambda \, \frac{1+(-1)^l}{4} \, \frac{\pi}{\nu} \, P_l\left(1+\frac{m_H^2}{2\nu}\right) .$$

6.2.6

In the physical region ($s>4m_H^2$ or $\nu>0$), $F_l(\nu)$ is bounded by unitarity. For the range $\nu\geq 0$ the following elastic unitarity condition holds:

$$\mathrm{Im}\, F_l(\nu) = \rho(\nu)\, |F_l(\nu)|^2$$

6.2.7

where $\rho(\nu) = \sqrt{\nu/s}$; we use this condition for all $\nu>0$. Notice, for $|\nu| \to \infty$, $\Delta F_l(\nu) \to 0$, and this suggests an unsubtracted representation for $F_l(\nu)$ of the form:

$$F_l(\nu) = \frac{1}{\pi} \int_{-\infty}^{m_H^2/4} \frac{\Delta F_l(\nu')}{\nu'-\nu-i\epsilon}\, d\nu' + \frac{1}{\pi} \int_0^{\infty} \frac{\rho(\nu')\, |F_l(\nu')|^2}{\nu'-\nu-i\epsilon}\, d\nu' .$$

6.2.8

This is an integral equation for $F_l(\nu)$ which specifies our model.

Notice that our Born term $B_l(\nu)$ does not contain the s-channel Higgs pole (the term $\lambda/(m_H^2-s)$ of eqs. 6.2.1 and 6.2.5); we would like to see whether it can be dynamically produced as a pole in $F_l(\nu)$.

We proceed with the N/D method (68,69). Write:

$$F_l(\nu) = \frac{N_l(\nu)}{D_l(\nu)}$$

6.2.9

with $N_l(\nu)$ containing the left-hand cut and $D_l(\nu)$ the right hand singularities. We are particularly interested in $l=0$, and we write an unsubtracted representation for $N_l(\nu)$:

$$N_l(\nu) = \frac{1}{\pi} \int_{-\infty}^{-m_H^2/4} \frac{\Delta F_l(\nu')\, D_l(\nu')}{\nu' - \nu - i\epsilon} d\nu' \ .$$

6.2.10

For $D_l(\nu)$ it is customary (68,69) to write a once subtracted representation. With no loss of generality we take the subtraction point at $\nu=0$, thus

$$D_l(\nu) = 1 \ - \ \frac{\nu}{\pi} \int_0^{\infty} \frac{\rho(\nu')\, N_l(\nu')}{\nu'\, (\nu' - \nu - i\epsilon)} d\nu' \ .$$

6.2.10′

Replacing this in equation 6.2.10 we obtain a linear integral equation for $N_l(\nu)$. Defining

$$f(\nu) = \sqrt{\frac{\rho(\nu)}{\nu}}\, N_l(\nu) \qquad \beta(\nu) = \sqrt{\frac{\rho(\nu)}{\nu}} B_l(\nu)$$

the integral equation is

$$f(\nu) = \beta(\nu) + \int_0^{\infty} K(\nu,x) f(x)\, dx$$

6.2.11

where

$$K(\nu,x) = \sqrt{\frac{\rho(\nu)\rho(x)}{\nu x}}\, \frac{1}{\pi^2} \int_{-\infty}^{-m_H^2/4} \frac{\nu' \Delta F_l(\nu')}{(\nu - \nu')(x - \nu')} d\nu' \ ;$$

6.2.12

in this way $K(\nu,x)$ is a symmetric kernel.

Now the important point is that with the Born term $B_l(\nu)$ given by eqs. 6.2.4 and 6.2.3, $\beta(\nu)$ is square integrable; and with $\Delta F_l(\nu)$ given by eq. 6.2.6, the kernel 6.2.12 has a bounded form (Hilbert-

Schmidt):

$$||K||^2 \equiv \int_0^\infty \int_0^\infty d\nu\, dx\, |K(\nu,x)|^2 < \infty$$

6.2.13

Equation 6.2.11 is therefore a Fredholm integral equation, and can be solved by standard methods. All this results from the fact that our left-hand discontinuity ΔF_l (and our Born term) is defined from scalar particle exchange between scalars.

Below we treat in detail the l=0 partial wave. Now, $\Delta F_0(\nu) = -\lambda\pi/2\nu$ and

$$K(\nu,x) = \frac{\lambda}{2\pi}\sqrt{\frac{\rho(\nu)\rho(x)}{\nu x}}\,\frac{1}{\nu - x}\ln\left(\frac{4\nu+m_H^2}{4x+m_H^2}\right)$$

6.2.14

Eq. 6.2.11 has an iteration (Neumann) solution provided that the norm $||K|| < 1$. This is satisfied for

$$m_H < 1.0\,TeV$$

6.2.15

this value gives an idea of the limit of applicability of the perturbation expansion.

Since the kernel 6.2.14 is symmetric, it has real eigenvalues (70); and since it is nonseparable, it has an infinity of eigenvalues with accumulation point at $\lambda=\infty$ ($M=\infty$) (70). We find the first eigenvalue at

$$M^1 \approx 1.1\,TeV$$

6.2.16

and the second eigenvalue at $\sim 4.1 TeV$.

Bound states of the system correspond to

$$D_I(s_B) = 0 \qquad 0 < s_B < 4m_H^2$$

6.2.17

and possible resonances correspond to

$$\mathrm{Re}\, D_I(s_0) = 0 \qquad s_0 > 4m_H^2 \ .$$

6.2.18

We remark that a difference between $N_I(s)$ and $B_I(s)$ is a measure of strong interaction effects.

Considering m_H as a free parameter, first for m_H $0.5 TeV$, we find no indication for a bound state or a resonance. Also $N_0(s)$ and $B_0(s)$ are similar; strong interaction effects are absent. Regarding the dispersive $F_0(s)$, since $D_0(s)$ shows no zero in the amplitude (6.2.9) we add by hand an s-channel Higgs pole term; the resulting amplitude is similar to $F_0^{pert}(s)$. In general, for $m_H < 0.6 TeV$ there is no bound state, however, for $m_H \geq 1 TeV$ there is a bound state. As m_H increases the position $\sqrt{s_B}$ of the bound state increases (figure 6.2). Evidently this can be interpreted as the Higgs-boson itself. In fact, for $m_H \approx 3.5 TeV$ there is an almost self-consistent solution ($\sqrt{s_B} \approx m_H$).

We calculate also the residue $r(s_B)$ of the corresponding pole of $F_0(s)$, in terms of $N_0(s_B)$ (figure 2). Self-consistency requires $r(s_B)$ λ, for $m_H = 3.5 TeV$, $r(s_B) \approx 2.9\lambda$, so that this condition is not well satisfied, but not grossly violated. This result can be interpreted to mean that the forces assumed to produce the Higgs-boson are qualitatively (but not quite quantitatively) correct (72). On the other hand, for $m_H \approx 1.5 TeV$, there is a self consistent solution with respect to the coupling; correspondingly, $\sqrt{s_B} \approx 1.85 m_H$.

Now, for $m_H > 1 TeV$ we turn to the region $s \geq 4m_H^2$. $N_0(s)$ and $B_0(s)$ are very different, clearly suggesting strong interaction effects. Interestingly, Re $D_0(s)$ has a zero, suggesting a possible resonance in the system of two Higgs-bosons and its position $\sqrt{s_0}$ increases with m_H (figure 6.2).

6.3 The Channel

$$Z_L Z_L \rightarrow Z_L Z_L$$

We turn to elastic scattering of longitudinal Z's. As a first effort we consider only Z's interacting with Higgs-bosons, leaving a more realistic treatment (involving coupled Z Z and W W channels (67)) for future work.

In perturbation theory (tree level) the amplitude (67) can be written

$$A(s,t) \approx \kappa\left(-\frac{3}{m_H^2}+\frac{1}{m_H^2-s}+\frac{1}{m_H^2-t}+\frac{1}{m_H^2-u}\right) \tag{6.3.1}$$

$(s,m_H^2>>M_Z^2)$, where $\kappa=\lambda/9$. In this form each of the terms corresponds to scalar-scalar interactions (equivalence theorem).

With $|\vec{q}|=$ the center of mass momentum of the Z and $|\vec{q}|^2=\nu$, now $s=4(\nu+M_Z^2)$; t and u have expressions as before. The projections of the terms $\kappa/(m_H^2-t)$ and $\kappa/(m_H^2-u)$ onto the partial wave $A_l(\nu)$ are similar to eq. 6.2.3. We define B_l as shown in equation 6.2.4 so that

$$A_l^{pert}(s) = B_l(s) + \kappa\left(-\frac{3}{m_H^2}+\frac{1}{M_H^2-s}\right)\delta_{l0} \tag{6.3.2}$$

In dispersion theory, (68,69) first two Z-bosons are exchanged in the s-, t- and u-channel; then there are higher mass exchanges (involving for example more Z-bosons). Again, the exchanged particles are on the mass-shell (physical). We make the following two assumptions: (i) the most important state exchanged in the t- and u-channel corresponds to Z-bosons resonating to a Higgs-bosons. (ii) Higher mass exchanges (corresponding for example to two Higgs-bosons) can be neglected.

Thus as a Born term we take $B_l(\nu)$ defined similarly to eqs. 6.2.3 and 6.2.4. For $4M_Z^2<s<16M_Z^2$ the partial wave amplitude $A_l(\nu)$ satisfies elastic unitarity in the form (6.2.7); again we use it for all $\nu>0$ (73).

The N/D method leads again to a Fredholm integral equation similar to 6.2.11. Notice that again this is due to the fact that our left-hand discontinuity (and our Born term) is defined from a scalar particle exchanged between scalars; and this was possible thanks to the equivalence theorem. (66,67) This is different from a vector meson (for example a ρ meson) exchanged between two pseudoscalars (e.g. pions) (68,69) resulting in an asymptotically constant left-hand discontinuity and thus requiring either the introduction of some cutoff or the solution of a singular (non-Fredholm) integral equation (74).

Treating l 0, now the condition $||K||<1$ is satisfied for m_H $0.83TeV$ and the first eigenvalue is found at $M^1\approx 1.4TeV$.

Notice that in our models, in the $Z_L Z_L$ system the eigenvalues (and the strong interaction effects) appear at a somewhat greater value of m_H than in the HH system. The difference arises as a result of two competing factors: (i) The Born term and the kernel are multiplied by a different coupling (κ for $Z_L Z_L$ versus $\lambda=9\kappa$ for HH). For $Z_L Z_L$, this factor tends to increase the limiting value of m_H satisfying the condition $||K||<1$, the position of the first eigenvalue M^1 etc. (ii) The kinematic factor $\rho(\nu)$ is different. For Z_LZ_L: $\rho(\nu)=\sqrt{\nu(\nu+M_Z^2)}/2$; for HH: $\rho(\nu)=\sqrt{\nu(\nu+m_H^2)}/2$. This factor acts in the opposite direction and partly (but not completely) compensates the effect of (i).

For m_H=0.5TeV we find again that $N_0(s)$ and $B_0(s)$ differ very little, and that Re $D_0(s)$ shows no indication of a zero; again strong interaction effects are absent.

For m_H>1.5TeV, however, $N_0(s)$ and $B_0(s)$ differ considerably. Also, it is interesting that Re $D_0(s)$ has a zero. For example, for m_H=2TeV, the zero is at $\sqrt{s}\approx 1.1TeV$; for m_H=2.5TeV, at $\sqrt{s}\approx 1.8TeV$. This zero can be taken as indicating a resonance, and, in fact, the Higgs-boson itself, which now in the ZZ channel should appear as a resonance. With this interpretation, again we found qualitative self-consistency. The value m_H=2.5TeV, singled out in the HH channel, evidently offers again a reasonable possibility. (75)

In figure 6.3 we present the amplitudes $|A_0(s)|$ (solid lines) and $|A_0^{pert}(s)|$ (dashed lines) for m_H=1.5, 2, and 2.5TeV, in the range $2M_Z<\sqrt{s}\leq 1.5TeV$ (76,77). For m_H=1.5TeV, $|A_0|$ exceeds $|A_0^{pert}|$ by a factor of 2~4; $|A_0|$ shows a broad bump at $\sqrt{s}\sim 0.65$ reflecting the zero of Re $D_0(s)$; $|A_0^{pert}|$ increases as $\sqrt{s}\rightarrow 1.5TeV$ due to the s-channel Higgs-boson pole (equation 6.3.2). For m_H=2TeV, $|A_0|$ and $|A_0^{pert}|$ are comparable; for this value of m_H, A_0^{pert} (tree level) clearly violates the unitarity bounds established in reference (67). We see that $|A_0|$ shows a broad bump at $\sqrt{s}\approx 1.1TeV$, reflecting the zero of Re $D_0(s)$. As $\sqrt{s}\rightarrow 2TeV$ $|A_0^{pert}|$ increases due to the s-channel Higgs-boson pole.

Finally, for m_H=2.5TeV $|A_0|$ is well below $|A_0^{pert}|$; $|A_0^{pert}|$ violates the unitarity bound (67).

Notice that for all values of m_H $|A_0(s)|$ reaches the maximum value $|A_0(s)|=2$; in figure 6.3 this is very clear for m_H=1.5 and 2TeV. The maximum value $|A_0|=2$ corresponds to saturating the unitarity bound.

For $m_H \geq 1.5TeV$, $D_0(s)$ has a zero at some distant $s<0$, for example, if m_H=2.5TeV, the zero is at $s \sim$-45TeV^2. This unpleasant feature could be interpreted to mean that our final amplitudes $A_0(s)$ corresponds to an extra (attractive, see (78)) force in addition to that of the Born term $B_0(s)$.

We have also applied the N/D method to the wave l=2. We find $|A_2(s)|$ smaller than $|A_0(s)|$ by one order of magnitude or more thus the l=2 and higher l partial waves may be neglected.

6.4 Conclusions

Our conclusions can be summarized as follows: Generally speaking, for $m_H \geq 1.5TeV$: (a) The dispersive amplitudes differ in structure from the corresponding perturbative (tree-level). For $m_H \approx 1.5TeV$, in $Z_L Z_L \rightarrow Z_L Z_L$ the former exceed the latter by factors of 2~4 (b) There are indications of strong interaction effects. In $HH \rightarrow HH$ there is an l=0 bound state. In $Z_L Z_L \rightarrow Z_L Z_L$ there is some indication of a resonance; as there is in $HH \rightarrow HH$. (c) The above l=0 bound state in $HH \rightarrow HH$ can be considered as the Higgs-boson itself. For $m_H \approx 3.5TeV$ there is an almost self-consistent solution with respect to the mass; this solution is very roughly self consistent with respect to the coupling as well; likewise at $m_H \approx 1.5TeV$ there is a self consistent solution with respect to the coupling roughly self consistent with respect to mass. There is also indication that the Higgs arises as a resonance in $Z_L Z_L$.

Figure Captions

Figure 6.1:

Feynman diagrams for Higgs-boson Higgs-boson scattering. (a) Tree level diagrams for a perturbative calculation of the Higgs-Higgs scattering amplitude. (b) The construction of the amplitude in dispersion theory.

Figure 6.2:

The results of the dispersion calculation for Higgs-boson Higgs-boson scattering as a function of m_H. This graph shows $\sqrt{s_B}$, the energy of the bound state (solid line); $\sqrt{s_0}$, the energy of the resonance (dashed line) and $r(s_B)/\lambda$, $r(s_B)$ being the residue of the bound state pole.

Figure 6.3:

The dispersive and tree level amplitudes for $Z_L Z_L$ scattering as a function of $\sqrt{s}$ for the values of Higgs-boson mass m_H=1.5, 2, and 2.5 TeV. The dispersive amplitude $|A_0|$ is shown with solid curves; the tree level amplitude $|A_0^{tree}|$ is shown with dashed curves.

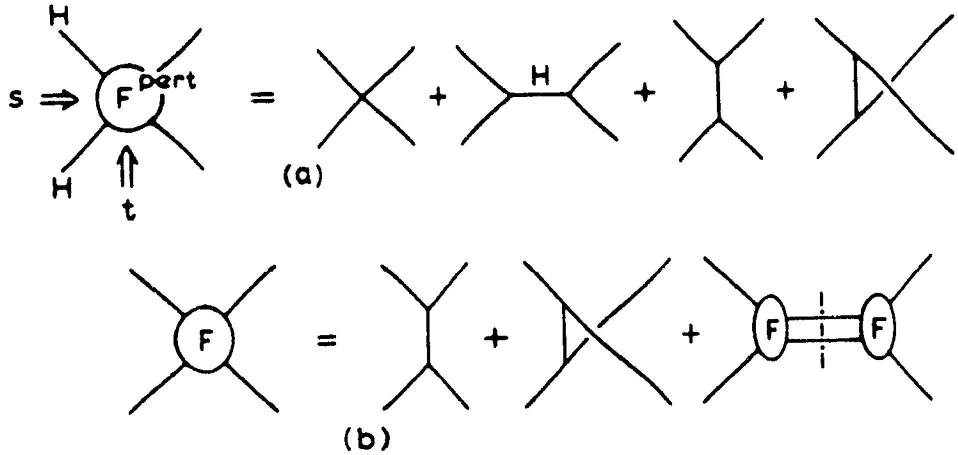

Figure 6.1

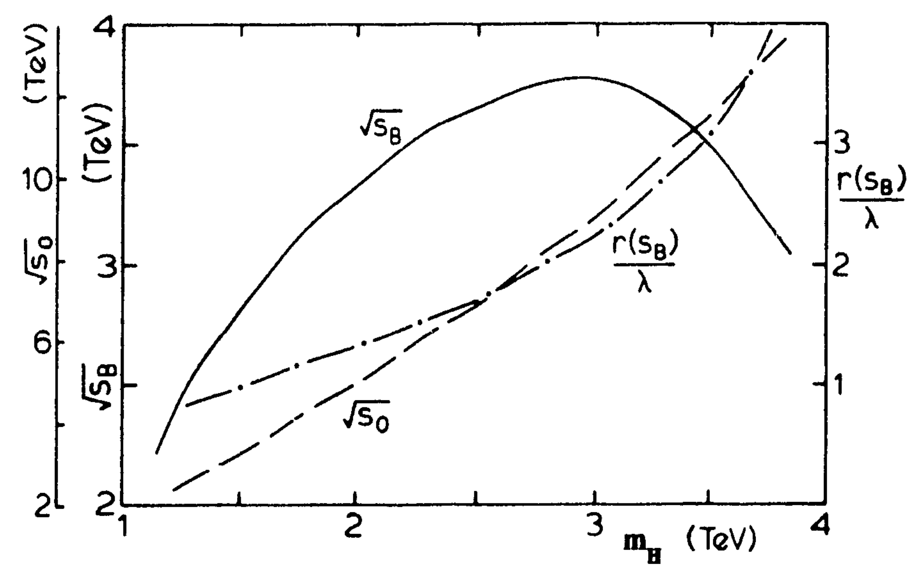

Figure 6.2

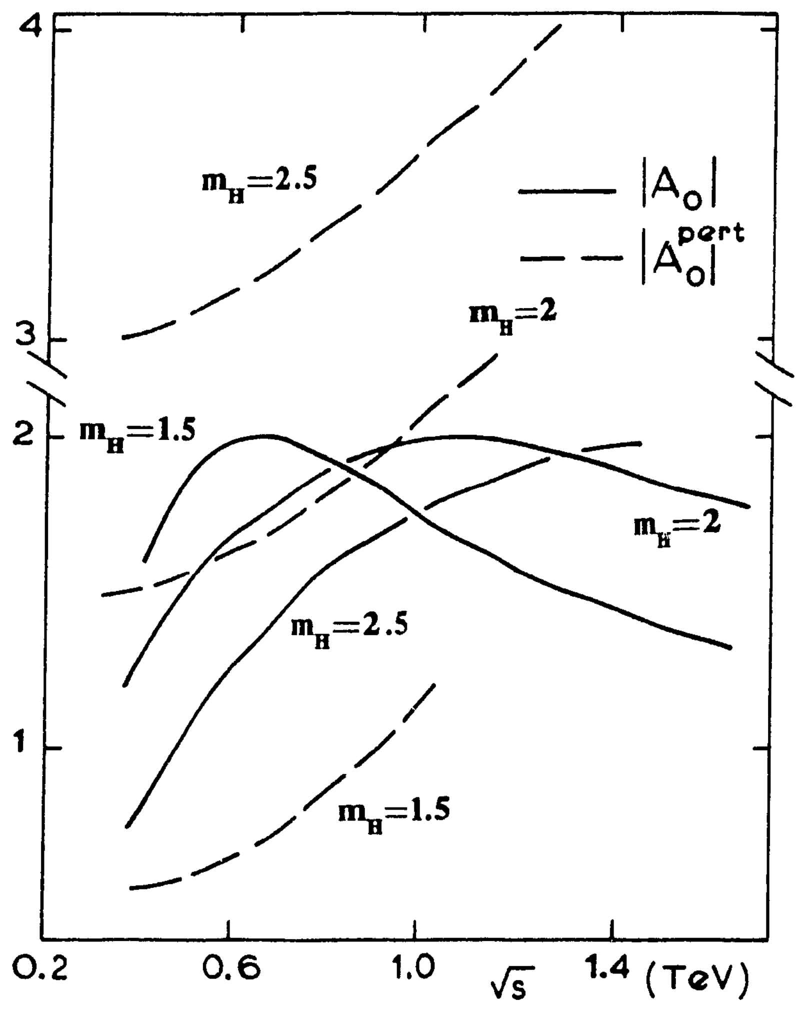
4
3
2
1
m_H=2.5
m_H=2
m_H=1.5
m_H=2
m_H=2.5
m_H=1.5
$|A_0|$
$|A_0^{pert}|$
0.2
0.6
1.0
$\sqrt{s}$
1.4
(TeV)

Figure 6.3

CHAPTER 7

CONCLUDING REMARKS

In conclusion, this thesis has considered strategies to find the Higgs-boson and top-quark, the missing pieces of the standard model, for a wide range of their possible masses.

In chapter 2 we have shown that a top-quark with mass $m_t \leq 80 GeV$ can be detected and its mass determined at e^+e^- colliders such as LEP and at $p\bar{p}$ colliders such as the Tevatron.

In chapter 3 we gave a possible strategy for Higgs searches at the Z peak which may be able to detect a Higgs-boson with mass $m_H < 60 GeV$. In chapters 4 and 5 we considered a Higgs-boson where m_H falls in the intermediate mass range at hypothetical e^+e^- colliders and at the SSC. In chapter 4 it was shown that such a Higgs-boson is certainly detectable at a e^+e^- collider with $\sqrt{s} \approx 300-500 GeV$. However no such collider is planned in the near future so the most immediate prospect for searching for a Higgs-boson in this mass range is through decay modes such as $H \to \tau^+\tau^-$ at the SSC (which is planned) considered in Chapter 5. As illustrated in figure 5.3, the various decay modes of the Higgs-boson cover most of the possible values of (m_H, m_t) (particularly if Tevatron results can establish a limit $m_t > 60 GeV$) where the redundancy that appears in some parts of that figure is important since all these channels are experimentally challenging to study.

If $180 < m_H \lesssim 600 GeV$, the Higgs could be detected through its decay $H \rightarrow W^+W^-$ at the SSC (79). If m_H is larger, however, it is not detectable at the SSC. In this mass range, the Higgs-boson starts to become strongly interacting and as was discussed in Chapter 6, it begins to show non-perturbative effects such as bound states and resonances. Such a massive Higgs-boson would probably be a strong hint of physics beyond the standard model.

FOOT NOTES AND REFERENCES

(1) D. Atwood, A. P. Contogouris, and H. Tanaka, Phys. Rev. Lett. 57 (1986) 2355.

(2) D. Atwood, A. P. Contogouris, and H. Tanaka, Phys. Rev. D36 (1987) 1547.

(3) D. Atwood, A. P. Contogouris, N. Mebarki, and H. Tanaka, Phys. Rev. D34 (1986) 2648.

(4) D. Atwood, A. P. Contogouris, and K. Takeuchi, Phys. Rev D34 (1988) 3437.

(5) D. Atwood, "Detection of Intermediate Mass Higgs in the $\tau^+\tau^-$ Decay Mode", *Workshop on Intermediate Mass and Non-Minimal Higgs Boson*, University of California at Davis (January 1988) 728.

(6) A. P. Contogouris, N. Mebarki, and D. Atwood, Mod. Phys. A2 (1987) 1075.

(7) A. P. Contogouris, N. Mebarki, D. Atwood, and H. Tanaka, Mod. Phys. Lett. A3 (1988) 295.

(8) (a) Ta Pei Cheng and Ling-Fong Li, *Gauge Theories of Elementary Particle Physics*, Oxford University Press, Oxford, (1984);

(b) C. Itzykson and J. Zuber, *Quantum Field Theory*, McGraw Hill Inc., New York, (1980).

(9) (a)Ta Pei Cheng and Ling-Fong Li, *Gauge Theories of Elementary Particle Physics*, Oxford University Press, Oxford, (1984) p. 342

(b) Schwinger, Ann. Phys. 2 (1957) 407.

(10) (a) G. Arinson et al (UA1 Collaboration), Phys. Lett. 166B (1986) 484;

(b) R. Ansari et al (UA2 collaboration), Phys. Lett. 186B (1987) 440.

(11) (a) S. Weinberg, Phys. Rev. Lett. 19 (1967) 1264;

(b) A. Salam in *Elementary Particle Physics* (Nobel symp. no. 8), N. Svartholm ed. , Almqvist and Wilsell, Stockholm (1968).

(12) (a) H. G. Georgi and S. L. Glashow, Phys. Rev. D6 (1972) 429,

(b) D. J. Gross and R. Jackiw, Phys. Rev. D6 (1972) 477;

(c) C. Bouchiat, J. Iliopoulos, and Ph. Meyer, Phys. Lett. 38B (1972) 519.

(13) (a) M. Kobayashi and T. Maskawa, Prog. Theor. Phys. 49 (1973) 652.

(b) For an alternative parameterization see H. Harrari and M. Leurer, Phys. Lett. B181 (1986) 123.

(14) Albajar et al. (UA1 collab.), Z. Phys. C37 (1988) 505.

(15) Franzini et al., Phys. Rev. D35 (1987) 2883.

(16) F. J. Gillman and M. Wise, Phys. Rev. D27 (1983) 1128.

(17) (a) U. Amaldi et al. Phys. Rev. D36 (1987) 1385.

(b) Similar results are also obtained in J. Ellis, G. Fogli, Phys. Lett. 213B (1988) 526.

(18) E. Farhi and L. Suskind, Phys. Rep. 74 (1981) 277.

(19) (a) F. Wilczek, Phys. Rev. Lett. 39 (1977) 1304;

(b) M. I. Vysotsky, Phys. Lett. 97B (1980) 159;

(c) P. Nason, Phys. Lett. 175B (1986) 223.

(20) (a) S. Raby, G. West and C. Hoffman, Los Alamos preprint LA-UR-88-2667 (1988).

(b) R. Barbieri and T. Erikson, Phys. Lett. 57B (1975) 270.

(c) J. Ellis, M. K. Gaillard, and D. V. Nanopoulos, Nuc. Phys. B106 (1976) 292.

(d) S. Weinberg, Phys. Rev. Lett. 36 (1976) 29.

(21) J. Ellis et al. Nuc. Phys. B106, (1976) 292.

(22) D. J. E. Callaway, Phys. Rep. 167 (1988) 214.

(23) J. F. Gunion et al, Nuc. Phys. B294 (1987) 621.

(24) (a) D. Atwood et al, Proceedings of *Experiments, Detectors, and Experimental areas for the Supercollider*, R. Donaldson and M. Gilchriese ed., Berkeley (1987) p. 728;

(b) J. F. Gunion and L. Roszkowski ed., *Workshop on Intermediate Mass and Non-Minimal Higgs Boson*, University of California at Davis (January 1988);

(c) E. Wang et al., "Detecting the Heavy Higgs Boson at the SSC", *Experiments, Detectors and Experimental Areas for The Supercollider*, (Berkely 1987) 20.

(d) F. Paige and E. Wang, "Standard Model Neutral Higgs Subgroup", in *From Colliders to Super Colliders* , (Madison 1986) 95.

(e) J. F. Gunion and H. E. Haber, "Probing the Higgs Sector at the SSC", *From Colliders to Super Colliders* , (Madison 1986) 67.

(25) J. H. Kuhn, J. Kaplan and E. G. O. Safiani, Nuc. Phys. B157 (1979) 125.

(26) (a) D. Atwood, A. P. Contogouris, H. Tanaka and S. Vlassopoulos, Phys. Rev. D33 (1986) 1260;

(b) D. Atwood, "Scalar-Quark Production in Electron-Positron Collisions", MSc. Thesis, McGill University, Montreal Canada, (1986).

(27) V. Barger, K. Hagiwara, W-K. Keung, and J. Woodside, Phys. Rev. D31 (1985) 528.

(28) (a) W. Bartel et al (Jade Collaboration), Phys. Lett. 155B (1985) 288;

(b) W. Ash et al, Phys. Rev. Lett. 54 (1985) 2477.

(29) G. P. Yost et al (Particle Data Group), Phys. Lett. B204 (1988) 1.

(30) A. Ali et al., Nuc. Phys. B167 (1980) 454.

(31) $\tilde{M}_J$ differs from the usual transverse mass (V. Barger, A. Martin and R. J. N. Phillips, Phys. Lett. 125B (1983) 343), but leads to stronger concentrations at $\tilde{M}_J = m_t$ (see below).

(32) B. Combridge, Nuc. Phys. B151 (1979) 429.

(33) E. Eichten et al, Rev. Mod. Phys. 56 (1984) 579, set 1.

(34) Suggested by collider data (G. Arnison et al (UA1 Collab.), Phys. Lett. 136B (1984) 294) and theoretical calculations (N. Antoniou et al, Phys. Rev. D29 (1984) 1354 and Phys. Lett. 128B (1983) 257).

(35) F. Berends et al, Phys. Lett. 103B (1981) 124.

(36) (a) J. Bjorken, in *Weak Interactions at High Energy and the Production of New Particles, Proceedings of the SLAC Summer Institute on Particle Physics* (1976), edited by M. C. Aipf (SLAC Report No. 198, 1977);

(b) D. Dicus and S. Willenbrock, Phys. Rev. D32 (1985) 1642;

(c) B. Joffe and V. Khoze, Leningrad Report No. 274 (1976) (unpublished);

(d) P. Kalyniak, J. Ng, and P. Zakarauskas, Phys. Rev, D29 (1984) 502.

(37) J. Finjord, Phys. Scr. 21 (1980) 143.

(38) E. Ma and J. Okada, Phys. Rev. D20 (1979) 1052.

(39) P Roudeau, Orsay Report No. LAL 85/29 (unpublished).

(40) P. Kalyniak, J. Mg, and P. Zakarauskas, Phys. Rev. D30 (1984) 123. As this work shows, however, the $m_{\ell\ell}$ distributions are different.

(41) F. Wilczek, Phys. Rev. Lett. 39 (1977) 1304.

(42) M. I. Vysotsky, Phys. Lett. 97B (1980) 159.

(43) J. Richardson, Phys. Lett. 82B (1979) 272.

(44) (a) A Martin, Report No. CERN-TH. 4060/84 (unpublished);

(b) A Martin, Phys. Lett. 156B (1985) 448.

(45) J Kuhn and P. Zerwas, Phys. Lett. 154B (1985) 448.

(46) (a) P Franzini and F. Gilman, Phys. Rev. D32 (1985) 237;

(b) P. Franzini, Report No. SLAC-PUB-3763, 1985 (unpublished).

(47) (a) F. J. Gillman and L. E. Price, "Detection of Higgs Bosons Decaying to Bottom Quarks", in *Physics of the SSC*, (Snowmass 1986) p.185;

(b) J. Brau, $H \to b\bar{b}$, in *Experiments, Detectors and Experimental Areas for The Supercollider* (Berkeley 1987) p. 735;

(c) J. Brau, K. T. Pitts, and L. E. Price, Oregon U. Preprint OREXP-88-1201 (1988).

(48) (a) J. Gunion and F. Haber, Mod. Phys. A2 (1987) 957;

(b) Z. Kunszt, *Proceedings of the International Europhysics Conference on High Energy Physics*, (Uppsala, Sweden, June 1987) 23;

(c) D. Atwood et al., "Intermediate Mass Higgs Boson(s)", in *Experiments, Detectors and Experimental Areas for The Supercollider*, (Berkeley 1987) 728;

(d) J. F. Gunion and L. Roszkowski ed., *Proceedings of The Workshop on Intermediate Mass and Non-Minimal Higgs Bosons*, (Davis CA 1988).

(49) G. Altarelli and E. Franco, Mod. Phys. Lett. A1 (1986) 517

(50) G. Barbiellini et al, in *Physics at LEP* (ed. CERN 86-02), Vol. 2 (1986) p. 1.

(51) J. Gunion, University of California, Davis preprint UCD-87-27 (1987).

(52) E. Kuraev and V. Fadin, Yad. Fiz. 41 (1985) 4661 (Sov. J. Nuc. Phys. 41 (1985) 466). Eq. 4.2.3 is a somewhat simplified form.

(53) P. Erhard (UA1 Collaboration), Proceedings of *The International Europhysics Conference on High Energy Physics*, (Uppsala, Sweden, June 1987) 169.

(54) H. Albrecht et al (Argus Collaborations), Phys. Lett 192B (1987) 245. However, values of m_t below $M_z/2$ are not excluded

(55) G. Altarerlli, Proceedings of Workshop on Physics at Future Accelerators, La Thuile and CERN, January 1987, p.36 (CERN-TH 4711).

(56) J. Gunion et al, Phys. Rev. D34 (1986) 101.

(57) J. F. Gunion et al, Nuc. Phys. B294 (1987) 621.

(58) J. Gunion et al, Phys. Rev. D34 (1986) 101.

(59) (a) F. J. Gillman and L. E. Price, "Detection of Higgs Bosons Decaying to Bottom Quarks", in *Physics of the SSC* (Snowmass 1986) 185.

(b) J. Brau, *H rarrow b b Bar* , in *Experiments, Detectors and Experimental Areas for The Supercollider* (Berkeley 1987) p. 735.

(c) J. Brau, K. T. Pitts, and L. E. Price, Oregon U. Preprint OREXP-88-1201 (1988).

(60) (a) D. Atwood et al, "Intermediate Mass Higgs Boson(s)", in *Experiments, Detectors and Experimental Areas for The Supercollider* (Berkeley 1987) p. 728.

(b) J. F. Gunion and L. Roszkowski ed., *Proceedings of The Workshop on Intermediate Mass and Non-Minimal Higgs Bosons*, (Davis CA 1988).

(61) J. F. Gunion, G. L. Kane and H. Wudka, Nuc. Phys. B299 (1988) 231.

(62) G. P. Yost et al. (Particle Data Group), Phys. lett. B204 (1988) 1.

(63) F. E. Paige and S. D. Protopopescu, *ISAJET 5.31: A Monte Carlo Event Generator for p-p and p-p bar Reactions*, Brookhaven National Labratories, Upton NY (1986).

(64) (a) Our gausian $p\!\!/_t^{min}$ distribution will therefore be similar to the distribution used in R. M. Barnett et al, "Detection of a Heavy Neutral Higgs Boson in a Higgsino-Neutralino Decay Mode", *Phsics of the Superconducting Supercollider* (Snowmass 1986). The non-gaussian tail suggested there is not critical for this applycation.

(b) See also R. M. Barnett, H. E. Haber and G. L. Kane, Nuc. Phys. B267 (1986) 625.

(65) R. K. Ellis et al, Nuc. Phys. B297 (1988) 221.

(66) (a) J. Cornwall, D. Levin, and G. Tiktopolos, Phys. Rev. D10, 1145 (1974);

(b) M. Chanowitz and M. Gallard, Nuc. Phys. B261, 379 (1985);

(c) G. Gounaris, R. Kogerler and H. Neufeld, Phys. Rev. D34, 3257 (1986).

(67) B. Lee, C. Quigg, and H. Thacker, Phys. Ref. D16, 1519 (1977).

(68) See for example D. Amati and D. Fubini, Ann. Rev. Nuc. Sc. 12, 359 (1962)

(69) G. F. Chew and S. Mandelstam, Phys. Rev. 119, 467 (1961) and Nuovo Cim. 19, 752 (1961).

(70) R. Courant and D. Hilbert, *Methods of Mathematical Physics* (New York, 1953), Vol. 1, Ch. III.

(71) A. P. Contogouris, N. Mebarki, D. Atwood, and H. Tanaka, Mod. Phys. Lett. A3 (1988) 295.

(72) A somewhat similar study of $HH \rightarrow HH$ (R. Chan and M. Suzuki, Phys. Lett. 134B, 115 (1984)) uses a different Born term and proceeds with a first iteration solution. For $M_H > 1.3 TeV$ it also finds an $I=0$ bound state, but with very small binding energy.

(73) Following the usual procedures (68,69), in $B_I(\nu)$ we have neglected the Higgs-boson width Γ_H. In view of its largeness for high m_H, this approximation is questionable.

(74) D. Atkinson and A. P. Contogouris, Nuovo Cim. 39, 1082 and 1102 (1965).

(75) Due to the Schwarz reflection theorem $A_0(s^*) = A_0^*(s)$, a resonance corresponds to a pair of complex conjugate poles on the second sheet of the complex s-plane. A linear expansion of Re $D(s)$ at $s=s_0$ gives the well- known expression for the width $\Gamma \approx \left(\frac{\text{Im } D(s)}{\sqrt{s}} \frac{d \text{ Re } D(s)}{ds} \right)_{s_0}$. Using this for m_H 2.5TeV when $\sqrt{s} \approx 1.8 TeV$ we obtain $|\Gamma| \sim 4 TeV$ but $\Gamma < 0$. We interpret this to mean that this expression is unreliable; due to the large distance of the poles from the real s-axis, the linear expansion of Re $D(s)$ may well be inadequate.

(76) Regarding the magnitude of the cross section $d\sigma/dm_{ZZ}$, keeping only $A_0(s)$ and using the Z_l structure function of references (77), for the contribution of the u-quark (one color) at $\sqrt{s} = m_{ZZ} \approx 1 TeV$ we find $d\sigma/dm_{ZZ} \approx 0.6 \times 10^{-3} \times |A_0|^2$.

(77) (a) G. Kane, W. Repko, and B. Rolnick, Phys. Lett 148B, 367 (1984);

(b) M. Duncan, G. Kane and W. Repko, Nuc. Phys B272, 517 (1986).

(78) The corresponding pole in $A_0(s)$ has residue $r(s_0) < 0$. Such a pole might be taken to represent distant singularities, initially neglected.

(79) (a) E. Wang et al., "Detecting the Heavy Higgs Boson at the SSC", *Experiments, Detectors and Experimental Areas for The Supercollider*, (Berkely 1987) 20.

(b) F. Paige and E. Wang, "Standard Model Neutral Higgs Subgroup", in *From Colliders to Super Colliders* , (Madison 1986) 95.

(c) J. F. Gunion and H. E. Haber, "Probing the Higgs Sector at the SSC", *From Colliders to Super Colliders* , (Madison 1986) 67.